A unified spectral/hp element depth-integrated Boussinesq model for nonlinear wave-floating body interaction

Umberto Bosi

▶ **To cite this version:**

HAL Id: tel-02297587

https://tel.archives-ouvertes.fr/tel-02297587

Submitted on 26 Sep 2019

THÈSE PRÉSENTÉE

POUR OBTENIR LE GRADE DE

DOCTEUR DE
L'UNIVERSITÉ DE BORDEAUX

ÉCOLE DOCTORALE DE MATHÉMATIQUE ET D'INFORMATIQUE

MATHÉMATIQUES APPLIQUÉES ET APPLICATION DES MATHÉMATIQUES

par **Umberto** BOSI

A UNIFIED SPECTRAL/HP ELEMENT
DEPTH-INTEGRATED BOUSSINESQ MODEL
FOR NONLINEAR WAVE-FLOATING BODY
INTERACTION

Sous la direction de Mario RICCHIUTO

Soutenue le 17 Juin 2019

Membres du jury :

M.	ABGRALL, Rémi	Professeur des Universités, UZH	Examinateur
M.	BENOIT, Michel	Professeur des Universités, IRPHE	Rapporteur
M.	ENGSIG-KARUP, Allan P.	Associate Professor, DTU	Examinateur
M.	ESKILSSON, Claes	Associate Professor, AAU	Invité
M.me	KAZOLEA, Maria	Chargé de Recherche, INRIA	Examinateur
M.	LANNES, David	Directeur de Recherche, IMB	Examinateur
M.	MARCHE, Fabien	Maître de Conférences, IMAG	Rapporteur
M.	NAVA, Vincenzo	Researcher, BCAM	Invité
M.	RICCHIUTO, Mario	Directeur de Recherche, INRIA	Directeur de these
M.me	WEINANS, Lisl	Maître de Conférences, IMB	Examinateur

Un modèle Boussinesq intégré en profondeur unifié d'élément spectral/*hp* pour une interaction nonlinéaire vague-corps flottante

Résumé

Le secteur de l'énergie houlomotrice s'appuie fortement sur la modélisation mathématique et la simulation d'expériences physiques mettant en jeu les interactions entre les ondes et les corps. Dans ce travail, nous avons développé un modèle d'interaction de fidélité moyenne vague-corps pour la simulation de structures tronquées flottantes fonctionnant en mouvement vertical. Ce travail concerne l'ingénierie de l'énergie marine, pour des applications telles que les convertisseurs d'énergie de vague (WEC) à absorption ponctuelle, même si ses applications peuvent aussi être utilisées en ingénierie maritime et navale. Les motivations de ce travail reposent sur les méthodes standard actuelles pour décrire l'interaction corps-vague. Celles-ci sont basées sur des modèles résolvant le flux de potentiel linéaire (LPF), du fait de leur grande efficacité. Cependant, les modèles LPF sont basés sur l'hypothèse de faible amplitude et ne peuvent pas répresenter les effets hydrodynamiques non linéaires, importants pour le WEC opérant dans la région de résonance ou dans les régions proches du rivage. En effet, il a été démontré que les modèles LFP prédisent de manière excessive la production de puissance, sauf si des coefficients de traînée sont calibrés. Plus récemment, des simulations Reynolds Averaged Navier-Stokes (RANS) ont été utilisées pour les WEC. RANS est un modèle complet et précis, mais très coûteux en calcul. Il n'est ni adapté à l'optimisation d'appareils uniques ni aux parcs énergétiques. Nous avons donc proposé un modèle de fidélité moyenne basé sur des équations de type Boussinesq, afin d'améliorer le compromis entre précision et efficacité.

Les équations de type Boussinesq sont des modèles d'ondes intégrées en profondeur et ont été un outil d'ingénierie standard pour la simulation numérique de la propagation d'ondes non linéaires dans les eaux peu profondes et les zones côtières. Grâce à l'élimination de la dimension verticale, le modèle résultant est très efficace et évite la description temporelle de la limite entre la surface libre et l'air. Jiang (2001) a proposé un modèle de Boussinesq unifié, décomposant le problème en deux domaines : surface libre et corps. Dans cette méthode, le domaine du corps est également modélisé par une approche intégrée en profondeur - d'où le terme unifié. Récemment, Lannes (2016) avait analysé de manière rigoureuse une configuration similaire dans une équation non linéaire en eaux peu profondes, en déduisant une solution exacte et semi-analitique pour des corps en mouvement. Suivant la même approche, Godlewski et al. (2018) a élaboré un modèle de flux d'eau peu profonde encombrée.

Le modèle de Boussinesq à intégration de profondeur introduit est basé sur l'approche unifiée de Jiang. Comme tous les modèles basés sur des équations de type Boussinesq, le modèle est limité aux régimes de profondeur peu profonde et intermédiaire. Nous considérons le modèle de Madsen et Sørensen comme un modèle de Boussinesq amélioré pour la surface libre . Nous démontrons que les termes dispersifs sont négligeables sous le corps. Pour mieux exploiter l'efficacité des modèles, nous utilisons une méthode d'éléments finis spectrale / *hp* afin de discrétiser les équations et de simuler des ondes non linéaires et dispersives interagissant avec des corps. La méthode des éléments spectraux / *hp* continus a été appliquée à la discrétisation dans chaque domaine. La méthode de Galerkin à éléments spectraux / *hp* discontinus a été utilisée pour dériver des conditions de flux pour le couplage des

domaines. L'utilisation d'éléments spectraux / *hp* prend en charge l'utilisation de maillages adaptatifs pour la flexibilité géométrique et des approximations précises d'ordre élevé, qui rend le schéma efficace.

Dans cette thèse, nous développons les résultats présentés par Eskilsson et al. (2016) et Bosi et al. (2019). Le modèle est étendu à deux dimensions horizontales. Le modèle 1D est vérifié à l'aide de solutions fabriquées et validé par rapport aux résultats publiés sur l'interaction vague-corps en 1D pour les pontons fixes et corps en mouvement de soulèvement forcé et libre. Les résultats des preuves de concept de la simulation de plusieurs corps sont présentés. Nous validons et vérifions le modèle 2D en suivant des étapes similaires. Enfin, nous mettons en œuvre la technique de verrouillage, une méthode de contrôle de mouvement du corps pour améliorer la réponse au mouvement des vagues. Il est démontré que le modèle possède une excellente précision, qu'il est pertinent pour les applications d'ondes en interaction avec des dispositifs à énergie houlomotrice et qu'il peut être étendu pour simuler des cas plus complexes.

Mots clés : énergie houlomotrice, modèles d'ondes non linéaires, modèles d'ondes intégrées en profondeur, équations de Boussinesq.

A unified spectral/*hp* element depth-integrated Boussinesq model for nonlinear wave-floating body interaction

Abstract

The wave energy sector relies heavily on mathematical modelling and simulation of the interactions between waves and floating bodies. In this work, we have developed a medium-fidelity wave-body interaction model for the simulation of truncated surface piercing structures operating in heave motion, such as point absorbers wave energy converters (WECs). The motivation of the work lies in the present approach to wave-body interaction. The standard approach is to use models based on linear potential flow (LPF). LPF models are based on the small amplitude/small motion assumption and, while highly computational efficient, cannot account for nonlinear hydrodynamic effects (except for Morison-type drag). Nonlinear effects are particularly important for WEC operating in resonance, or in nearshore regions where wave transformations are expected. More recently, Reynolds Averaged Navier-Stokes (RANS) simulations have been employed for modelling WECs. RANS is a complete and accurate model but computationally very costly. At present RANS models are therefore unsuited for the optimization of single devices, not to mention energy farms. Thus, we propose a numerical model based built on Boussinesq-type equations to include wave-wave interaction as well as finite body motion in a computationally efficient formulation.

Boussinesq-type equations are depth-integrated wave models and are standard engineering tool for numerical simulation of propagation of nonlinear wave in shallow water and coastal areas. Thanks to the elimination of the vertical dimension and the avoidance of a time-dependent computational the resulting model is very computational efficient. Jiang (Jiang, 2001) proposed a unified Boussinesq model, decomposing the problem into free surface and body domains. Notably, in Jiang's methodology also the body domain is modeled by a depth-integrated approach – hence the term unified. As all models based on Boussinesq-type equations, the

model is limited to shallow and intermediate depth regimes. We consider the Madsen and Sørensen model, an enhanced Boussinesq model, for the propagation of waves. We employ a spectral/*hp* finite element method (SEM) to discretize the governing equations. The continuous SEM is used inside each domain and flux-based coupling conditions are derived from the discontinuous Galerkin method. The use of SEM give support for the use of adaptive meshes for geometric flexibility and high-order accurate approximations makes the scheme computationally efficient.

In this thesis, we present 1D results for the propagation and interaction of waves with floating structures. The 1D model is verified using manufactured solutions. The model is then validated against published results for wave-body interaction. The hydrostatic cases (forced motion and decay test) are compared to analytical and semi-analytical solutions (Lannes, 2017), while the non-hydrostatic tests (fixed pontoon and freely heaving bodies) are compared to RANS reference solutions. The model is easily extended to handle multiple bodies and a proof-of-concept result is presented. Finally, we implement the latching technique, a method to control the movement of the body such that the response to the wave movement is improved. The model is extended to two horizontal dimensions and verified and validated against manufactured solutions and RANS simulations. The model is found to have a good accuracy both in one and two dimensions and is relevant for applications of waves interacting with wave energy devices. The model can be extended to simulate more complex cases such as WEC farms/arrays or include power generation systems to the device.

Keywords: Wave energy, nonlinear wave models, depth-integrated wave equations, Boussinesq equations.

Unité de recherche : INRIA Bordeaux Sud-Ouest – Equipe CARDAMOM, 200 avenue de la Vieille Tours, 33405 Talence

Résumé substantiel

Il a été estimé que le changement climatique s'est accéléré au cours des dernières décennies et que ses effets s'aggravent de plus en plus de façon extrême et catastrophique (par exemple la montée du niveau de la mer ou les grandes tempêtes [69]). Les actions entreprises par les gouvernements ont impliqué la stipulation d'accords internationaux [4] ainsi que l'attention et l'investissement accrus dans les politiques et les recherches visant à contrôler l'impact humain sur l'environnement. Le groupe d'experts intergouvernemental sur l'évolution du climat (GIEC) a reconnu dans les sources d'énergies renouvelables, telles que l'énergie éolienne et solaire, une mesure valable [133] afin de ralentir le réchauffement climatique. Dernièrement, les ressources en énergie océanique ont été prises en compte pour intégrer la production d'énergie, en utilisant des dispositifs à énergie houlomotrice (WEC) pour produire de l'électricité.

La quantité théorique mondiale de l'énergie houlomotrice est estimée à 2.11 ± 0.05 TW, dont environ 4.6% extractibles avec les technologies actuelles [87]. L'exploitation de l'énergie houlomotrice est également incluse dans le plan européen de réduction des gaz à effet de serre, utilisant des sources d'énergie renouvelables d'objectifs de 20% d'ici 2020, et de 80 à 95% avant 2050, augmentant la production actuelle d'énergie houlomotrice de 100 GW d'ici là [125]. L'énergie des vagues est régulièrement étudiée depuis les années soixante-dix [158, 65, 26]. Il existe plusieurs dispositifs exploitant différentes conceptions, localisations ou méthodes de récolte, et leur catégorisation peut varier : *wave terminators* [158, 7], *waves attenuators* [91] ou *point absorbers* (PA) [141, 70]. Une autre classification du WEC est effectuée en fonction de la manière dont le WEC génère l'énergie : *oscillating water column* (OWC) [181], *overtopping device* [105] et *corps activés par les vagues* [70, 35, 128].

Pour cette thèse, des PA WEC à pillonement ont été choisis. Ces WEC sont généralement des bouées flottantes qui peuvent absorber l'énergie des vagues provenant de toutes les directions, à partir du mouvement vertical imposé par les vagues. Le réglage de base d'un PA est composé d'un corps flottantes auto-activé [15] ou connecté par des amarres [142] au fond marin et à un système de prise de force, généralement un générateur électrique ou une pompe hydraulique, permettant de convertir le mouvement vertical en électricité. Pour mieux tirer parti de la caractéristique du PA et maximiser l'énergie absorbée, plusieurs PA sont souvent utilisés, disposés dans des parcs. La géométrie du parc doit être configurée pour exploiter au mieux l'extraction d'énergie [8]. Le PA agit efficacement comme un atténuateur d'onde, réduisant la hauteur des ondes transmises. S'il est installé dans la région côtière, l'effet d'atténuation se propage au littoral et peut réduire l'érosion du rivage et la perte de plages. [1, 131].

Le test du PA WEC est donc extrêmement important, à la fois pour comprendre et quantifier les effets du champ éloigné et du champ proche et pour optimiser la position de plusieurs WEC afin de maximiser la production d'énergie. L'expérimentation physique et la modélisation numérique sont les techniques de test. L'approche

physique nécessite des modèles de WEC placés soit dans des canaux ou des bassins d'eau, soit en pleine mer pour des tests sur le terrain. L'avantage du bassin hydrographique réside dans la possibilité de réaliser des expériences dans un environnement contrôlé. Il est possible de générer des conditions d'état de la mer cohérentes et reproductibles et de mesurer facilement les paramètres hydrodynamiques de l'eau ainsi que des CVE. Cependant, la modélisation physique étant économiquement coûteuse, il est de plus en plus courant de la compléter par une modélisation numérique, en la remplaçant parfois à de nombreuses étapes de la conception du WEC. Weber [182] a fait remarquer qu'il est plus économique d'élever le niveau de performance technologique d'un concept WEC à un niveau de préparation à la technologie faible. Une telle voie de développement impose une plus grande demande aux méthodes numériques utilisées. Des expériences physiques sont ensuite utilisées pour valider la précision des résultats numériques. Les nombreux modèles mathématiques d'interaction vague-corps décrivent avec une précision différente la dynamique du champ de fluide et le mouvement du WEC sous la force de la vague. Le choix du modèle est donc dicté par la physique régissant l'interaction et le compromis entre la précision requise, le temps de calcul et la puissance disponible. Le temps et la puissance de calcul requis pour résoudre un modèle augmentent avec la complexité. De plus, selon les critères de fonctionnement du WEC considérés et les effets étudiés, différents modèles mathématiques doivent être envisagés.

De nos jours, la modélisation numérique des PA WEC repose largement sur l'utilisation d'outils basés sur l'équation de Cummins [41] en utilisant des coefficients hydrodynamiques calculés à partir du flux de potentiel linéaire (LPF) pour la prédiction de mouvements, de charges et de production d'énergie. Les modèles LPF sont basés sur l'hypothèse de faible amplitude et sont largement utilisés pour leur simplicité et leur efficacité. Bien que les modèles LPF aient été utilisés avec succès dans de nombreuses applications offshore [68], les approximations de faible amplitude et de petit mouvement ne sont pas valables dans de nombreux cas, tels que les WEC fonctionnant dans la région de résonance et en particulier pour les cas où les effets hydrodynamiques non linéaires sont prédominants.

Plus récemment, grâce à l'augmentation de la puissance de calcul, des simulations CFD ont été utilisées dans plusieurs cas pour les PA WEC [119, 193, 143]. Comparées aux modèles LPF linéaires, les simulations basées sur le volume de CFD de fluide (VOF-CFD) présentent l'avantage de capturer toute la dynamique non linéaire des expériences de WEC et de vagues près des côtes. En fait, les simulations RANS ont montré que les modèles LPF peuvent ne pas convenir à l'optimisation de WEC. En comparant les résultats obtenus avec les deux méthodes, il est clair que LPF surestime la production d'énergie, en particulier dans la région de résonance [193, 143]. Cependant, les expériences RANS restent extrêmement coûteuses. Une simulation avec un état de mer complet pour un WEC peut nécessiter jusqu'à 150 000 heures de CPU par simulation [63].

Dans les eaux peu profondes aux eaux intermédiaires à vagues non déferlantes, les équations de type Boussinesq (BTE) constituent une alternative au modèle LPF et CFD. Les BTE constituent une famille d'équations intégrées en profondeur qui expriment l'hydrodynamique non linéaire des vagues uniquement en dimensions horizontales. Cela rend les BTE moins exigeants en termes de calcul que les équations 3D complètes. Les BTE sont des modèles d'onde standard [2, 147, 124], utilisés pour prédire la propagation des ondes non linéaires dans les zones côtières et littorales. Cependant, les corps tronqués de perforation de surface sont difficiles à manipuler avec un modèle d'onde intégré en profondeur. Les approches typiques [59, 138, 33]

n'incluent pas le corps réel dans la discrétisation. Le travail de Jiang [96] et plus recemment de Lannes [111] et [78] sur le modèle de Boussinesq «unifié» constitue une exception. La technique proposée consiste à décomposer le domaine numerique en domaines de surface libre et de corps. Il est important de noter que le domaine sous le corps a également été modelé avec une approche intégrée en profondeur - d'où le terme «unifié».

Les équations aux dérivées partielles décrivant le problème du corps d'onde sont résolues grâce à des schémas de discrétisation se rapprochant du modèle continu d'origine et pouvant être traités numériquement. Plusieurs stratégies de discrétisation et de résolution pour les EDP ont été proposées, mais nous allons nous concentrer sur les méthodes d'ordre élevé, qui ont une précision spatiale égale ou supérieure à trois, et sont particulièrement souhaitables pour la simulation de solutions lisses et intégrations à long terme.

L'une des méthodes les plus courantes et historiquement la première utilisée pour résoudre les PDE est la méthode des différences finies (FDM). FDM se rapproche des dérivées sur une grille discrète en utilisant des différences finies, convertissant ainsi le système PDE en un système d'équation algébrique. La résolution du nouveau système est particulièrement bien adaptée à la résolution numérique, d'où la généralisation de cette méthode en analyse numérique [85]. De plus, on peut atteindre une résolution élevée [117, 88, 163] et même une convergence spectrale [115].

Une méthode alternative est la méthode des éléments finis (FEM) est basée sur une méthode variationnelle d'approximation de la PDE. Le domaine global est divisé en un maillage de sous-domaines que nous désignerons comme des éléments dans ce qui suit et dans chacun d'eux sont définis un ensemble de fonctions de base. La méthode Galerkin [74] est généralement utilisée dans les MEF pour résoudre des équations différentielles. La méthode de Galerkin est un cas particulier de la famille des méthodes de pondération des résidus (WR) [40, 72] pour lesquelles les fonctions de pondération sont identiques aux fonctions d'interpolation.

Les méthodes des éléments limites (BEM) [21, 77] sont apparues comme une puissante alternative aux méthodes FEM et FDM, en particulier dans les cas où le domaine s'étend à l'infini. Avec BEM, nous désignons toute méthode pour cela qui approxime la solution numérique des équations intégrales aux limites par des équations avec des états limites connus et inconnus. Par conséquent, il ne nécessite que la discrétisation de la surface plutôt que du volume, c'est-à-dire que la dimension des problèmes est réduite d'une unité. Par conséquent, l'effort de discrétisation nécessaire est généralement beaucoup plus petit et, de plus, des maillages peuvent être facilement générés et les modifications de conception ne nécessitent pas de remodelage complet.

Toutes ces méthodes ont été utilisées avec succès pour étudier le problème de l'interaction vague-corps, cependant pour cette thèse la méthode des éléments finis spectral/hp (SEM) [169, 145] a été adopté pour la résolution des modèles mathématiques. Un avantage du SEM par rapport aux autres méthodes (éléments/volumes finis, différence finis ou méthode des éléments finis de frontière) est qu'il permet la convergence à la fois dans le sens de l'adaptivité h- et p-. Cela signifie qu'il est possible d'affiner le maillage en conservant l'ordre polynomial constant (adaptabilité h-) et en utilisant des éléments plus petits pour capturer des phénomènes à petite échelle, ou augmenter l'ordre polynomial (adaptabilité p-). L'adaptivité hp- est une combinaison des deux types d'adaptivité et peut être utilisée pour obtenir une convergence optimale [13] et réaliser une convergence efficace sur les fonctionnalités à grande échelle [99]. Le mot "spectral" du SEM suggère le taux de convergence élevé

de la méthode, qui, avec le bon choix de points en quadrature et de fonctions d'interpolation, peut être extrêmement rapide. De plus, le SEM a été utilisé avec succès dans la simulation de flux complexes [103, 161] et dans un certain nombre d'autres applications, en particulier la modélisation océanographique [38, 135, 28]. On obtient une efficacité et une précision élevées dans la simulation du flux entièrement non linéaire [80, 55] et du flux Boussinesq faiblement non linéaire [60]. Plus important encore, ces dernières années, le SEM a été largement utilisé dans les problèmes d'interaction corps-ondes : les résultats d'une vague diffusée par une structure qui s'étend jusqu'au fond de la mer [60]. Le cas des structures tronquées a été largement étudié dans le cas de structures fixes [58, 57, 114], aussi bien que de structures à soulèvement libre [64, 20, 134].

Cette thèse vise à développer des modèles basés sur des équations de type Boussinesq non linéaires efficaces en calcul pour l'interaction entre les vagues et les corps flottants. Comme tous les modèles BTE, le modèle presenté est limité aux régimes de profondeur peu profonde et intermédiaire. Bien que le modèle ne se limite pas aux applications dans les énergies marines renouvelables, la raison pour laquelle un modèle de corps de vagues de fidélité moyenne a été développé se trouve dans l'état actuel de la modélisation des PA dans les eaux littorales. Cependant, l'intérêt sur ce modèle provient aussi bien de problèmes d'ingénierie côtière ou navale.

Nous proposons un modèle de Boussinesq unifié et intégré en profondeur pour l'interaction non linéaire vague-corps, basé sur l'approche unifiée introduite par Jiang [96]. Dans ce manuscrit, nous déduisons tout d'abord trois modèles unidimensionnels du type Boussinesq à surface libre : le modèle non linéaire et non dispersif pour eau peu profonde et les modèles non linéaires faiblement dispersifs d'Abbott [2] et de Madsen et Sørensen [124] et nous analysons leurs propriétés de dispersion linéaire. Les équations décrivant la dynamique du corps sont déduites de la BTE de surface libre. Nous avons discuté de la nécessité d'un modèle dispersif dans le domaine du corps et nous avons obtenu l'équation d'accélération qui permet l'évolution de la position du corps dans le temps. Enfin, dans cette première partie, nous examinons les stratégies de couplage nécessaires pour permettre l'échange d'informations entre le domaine de surface libre et le WEC.

En adaptant l'idée originale en termes de discrétisations, nous utilisons une méthode spectrale/éléments finis *hp* pour la simulation d'ondes non linéaires et dispersives en interaction avec des corps fixes et soulevés. En particulier, nous utilisons la méthode SEM continue [99] à l'intérieur de chaque domaine et la méthode de couplage introduite pour le système continu est implémentée dans le modèle discret, basé sur le flux entre domaines conformes à la méthode SEM de Galerkin discontinue [37].

Il en résulte un nouveau modèle efficace et précis simulant la propagation des ondes et l'interaction non linéaire des ondes avec les corps. Ce modèle a été validé et après utilisé pour évaluer les points de repère pour une boîte unidimensionnelle, reproduisant les résultats publiés pour un ponton fixe [55, 120] ou une boîte de soulèvement en mouvement forcé et en décomposition [111]. De plus, nous avons évalué la réponse au mouvement des vagues (RAO) d'une boîte flottante librement soumise à des trains de vagues de différentes raideur. Les résultats ont montré un bon accord avec résultat évalué pour les ondes linéaires et nous pouvons retracer le comportement du modèle linéaire, avec le pic caractéristique à la fréquence de résonance. Pour les ondes de raideur moyenne, le RAO résultant est plus proche de la simulation RANS, améliorant les prédictions du modèle linéaire.

Dans la deuxième partie, les modèles continues et discrets sont étendus à deux dimensions horizontales, ce qui nous permet de simuler des cas plus réalistes. En ce qui concerne les modèles unidimensionnels, nous avons présenté les différents modèles de Boussinesq et la dérivation d'une méthode SEM en 2D pour les résoudre numériquement. Les modèles sont ensuite mis à l'essai : d'abord vérifiés à l'aide de solutions appropriées, puis validés par rapport aux résultats CFD et FNPF.

Malgré les défis à venir, c'est-à-dire plus de grade de liberté pour le corps et une technique de production d'énergie permettant de relier notre travail à des applications techniques, nous estimons que le présent travail indique qu'un système Boussinesq unifié de fidélité moyenne peut apporter des avantages en termes d'efficacité sans compromettre la précision des résultats. Nous avons montré que les modèles de Boussinesq, s'ils sont appliqués dans les hypothèses de dispersion et de non-linéarité sous-jacentes, montrent un accord acceptable avec les résultats CFD et FNPF, à la fois en une et en deux dimensions, et constituent une alternative valable pour la simulation de structures flottantes dans des eaux peu profondes.

Acknowledgements

This thesis has been like a big, long journey which has now reached its destination and opened the road to new ones. So this is the time to thank all the people that I met and made this adventure.

First of all Mario, my captain, who has been constantly supportive and ready, who always has an answer and new ideas. Thanks for everything, without your guide I wouldn't have arrive to the end. I salute you!

Thanks Allan and Claes, my "unofficial" supervisors that, parallel to Mario, had helped me in many aspect of the thesis, from the mathematics and physics behind this work to invest time in the debugging of the code.

A huge thanks to all the people that passed at the Cardamom equipe, both who already left and the new ones. It has been great to work in our "italian" community side by side the french minority! You are too many but it has been amazing, we spent a great time together and I won't ever forget you!

My family deserve an immense hug, they have been always by my side in all this year of study pilgrimage around Europe. Un grazie infinito ai miei genitori, i nonni, Luei e Alice per aver sempre creduto in me in tutto questo tempo e essere sempre stati al mio fianco anche quando sono stato lontano. Siete fantastici!

Finally, my girlfriend. Thank you Mahalia to have endured with me this roller-coaster of emotions that has been this PhD, cheering with me at the best times and give me strenght in the hard ones. You had the charisma, uniqueness, nerve and talent that I needed!

Contents

Chapter 1

Introduction

Sommaire

1.1 Technology and motivations

It has been assessed that the climate change has accelerated in the last few decades [168], and its effects are getting more extreme and catastrophic (i.e. sea rise or superstorms [69]). The actions undertaken by Governments has involved stipulation of international agreements [4] as well as dedicating more attention and investment to policies and researches inclined to control the human impact on the environment. The Intergovernmental Panel on Climate Change (IPCC) had recognised in renewable energy sources, such as wind and solar energy, a valid countermeasure [133] to slow global warming. Lately, ocean energy resources have been taken into consideration to integrate the power production, with the possibility to use wave energy converters (WECs) to generate electricity.

The world's theoretical total wave energy is estimated to be 2.11 ± 0.05 TW, with about $4,6\%$ extractable with present technologies [87]. The exploitation of wave energy is also included in the European plan to reduce the greenhouse gas using renewable energy sources of targets of 20% by 2020, and 80 to 95% by 2050 [178], with the goal of 100 GW wave energy installed power by 2050 [125]. The energy is harvested from waves generated by the winds blowing on the sea surface. Waves power presents characteristics that make them an attractive energy source: in particular the waves can transport energy without significant losses over long distances and their movements are predictable, with gradual changes, and more constant than wind or solar power, rendering the setting of the devices easier and more manageable . Wave energy has been regularly studied since the seventies [158, 65, 26]. However, the first technologies that can harvest wave energy dates back to the nineteen century, with patents as early as 1799 (M. Girard, France) [36]. Several devices are available that exploit different design, locations or harvesting methodology and their categorization can vary. Considering the position of the body to the wave front, the three main categories are:

— *Wave terminators* are long structures compared to the wavelength. The terminators are placed parallel to the wave front, forming an artificial coastline.

Examples of terminators are the Salter's nodding duck [158] or the Oyster800 by Aquamarine Power [7];

— *Wave attenuators* are long structures that are aligned to the wave direction, perpendicular to the front, such as the Pelamis wave generator design [91];

— *Point absorbers* (PA) are buoy structures typically of smaller dimensions compared to the wavelength in which they operate that can absorb energy from waves incoming from any direction. PA WECs had been developed for example by CorPower [141] or at the École Central de Nantes [75].

An alternative classification of the WEC is done by the way the power is generated by the WEC. The most common working principles are

— *Oscillating water column* (OWC) such as the light buoys introduced in Japan by Yoshio Masuda (1925-2009) [66] or the Wave Swell Energy [181], where the waves power an oscillating air flow throug a turbine;

— *Overtopping devices*. The water enters a reservoir inside the device and the returning water flow is use to activate a turbine at the device bottom. The Wave Dragon [105] is an overtopping WEC.

— *Wave activated bodies*. The wave activates the motion of the body and from this the power production. In this category are included PA [70], oscillating surge [35] and pitch converters [128].

(A)

(B)

(C)

(D)
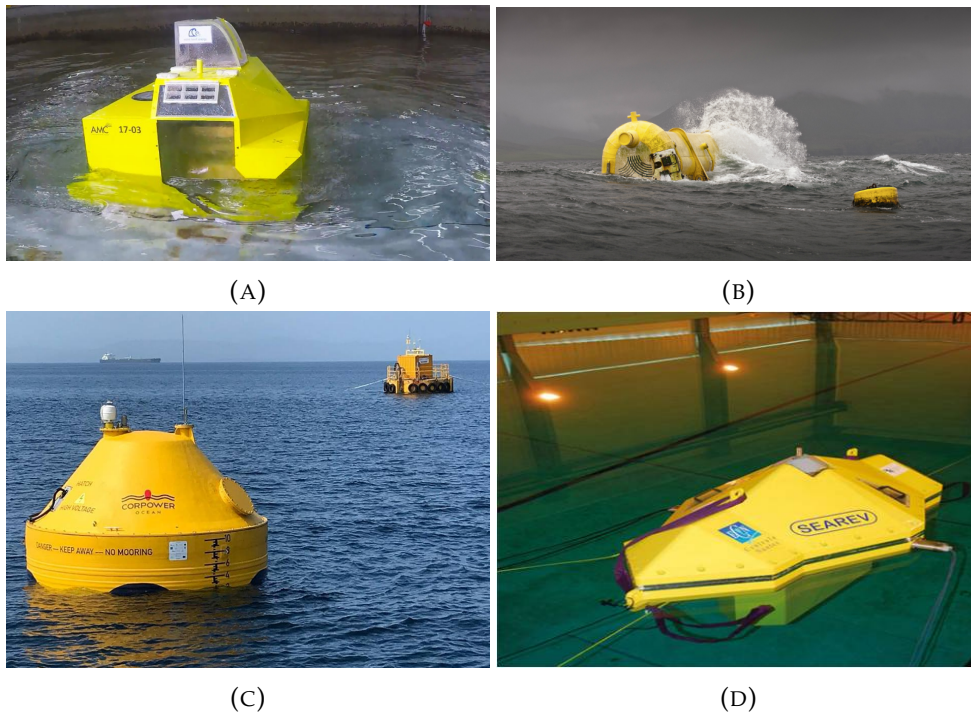
FIGURE 1.1 – Few examples of WECs: in figure (a) the oscillating water column by Wave Swell Energy [181], (b), the oscillating surge Converter Oyster800 by Aquamarine Power [7], (c) the heaving PA by CorPower [160], (d) the oscillating pitch converter SEAREV developed by the École Central de Nantes [75].

However, many more designs and variations of these basic concepts have been proposed, depending on the positioning (off-shore, near-shore or on-shore) and activation technique. A review of several design of WECs is presented in [50] and [98]. For this research we have focused on heaving point-absorber WECs. These WECs are usually surface piercing floating devices that produce energy from the

vertical motion imposed by the waves. The basic setting of a PA is composed of a floating body that is either self activated [15] or connected by mooring lines [142] to the seabed and a power take-off (PTO) system that can convert the vertical movement into electricity, usually an electrical generator or a hydraulic pump. Heaving PA have usually an axisymmetric geometry such that they can extract energy from waves coming from any direction. To better take advantage of the characteristic of the point absorbs WECs and maximize the energy absorbed, multiple WECs are often employed, arranged in farms or arrays. The WECs interact and disturb the incoming waves, generating transmitted and reflected waves, affecting the power production. Thus, the near-field interactions must be taken into accounts when designing the geometry of the farms: the near-field waves are composed of incoming, radiated and reflected transmitted waves, such that the resulting elevation can be locally higher or lower than the incoming field [8]. The array geometry must be configurated to exploit those effects at best and improve the energy extraction [8]. The far field is also influenced by the presence of WECs. WEC effectively acts as a wave attenuators, reducing the height of the transmitted waves. If installed in the near shore region, the attenuating effect propagates to the coastline and it can reduce the shore erosion and beach loss [1, 131].

The testing of WEC is thus extremely important, both to understand and quantify the far-field and near-field effects and optimize the position of single WECs to maximize the power production. Physical experimenting and numerical modelling or the combination of them are the testing techniques. The physical approach requires models of the WECs placed either in water flumes or basins or in the open sea for field tests. The advantage of water basin lays in the possibility of perform experiments in controlled environment, consistent and repeatable sea state condition can be generated and the hydrodynamics parameters of the water as well as of the the WECs can be easily measured. However, physical modelling is economically expensive so it is increasingly more common to complement it with numerical modelling, sometimes substituting it in many steps of the WEC's design. Weber [182] pointed out that it is more economical to raise the technology performance level (TPL) of a wave energy converter (WEC) concept at low technology readiness level (TRL). Such a development path puts a greater demand on the numerical methods used. The findings of Weber also tell us that important design decisions as well as optimization should be performed as early in the development process as possible. The performance prediction can be performed with the aim of several mathematical models that describe the wave-body interaction. All the models produced describe with different precision grade the dynamics of the fluid field and the WEC's movement under the wave force. The choice of the model is thus dictated by the physics governing the interaction, and the trade off between the accuracy required, the computational time and power available. The computational time and power demanded to solve a model increases with the complexity. Moreover, depending on the functioning criteria of the WEC considered and the effects that are investigated, different mathematical models must be considered. Appropriate set of equations in a numerical domain with the suitable boundary condition to represent a particular sea state and the dynamics of the WEC. The precision of the numerical results are dependent on the physics described by the equations, thus they have to be validated against physical experiment.

The complexity of the numerical model render its resolution more demanding on the machine power and time. Nowadays, thanks to the increase in computational power, more and more complicated and complete models can be solved in a reasonable time. However, for large simulations and fast development of physical
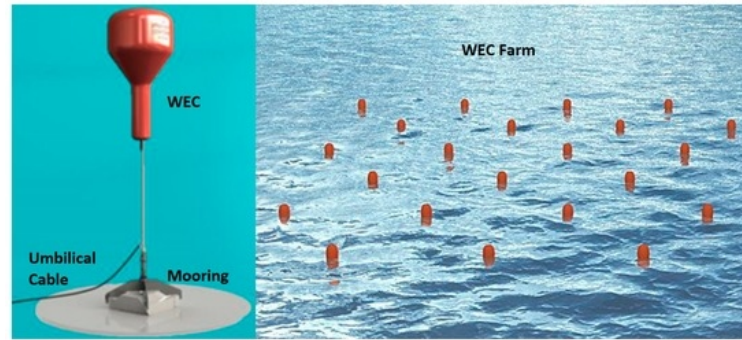
FIGURE 1.2 – Artistic representation of a PA WEC and an energy farm, thanks to Corpower Ocean [160].

models, the numerical modelling must be optimized and reliable, with a high trade-off between efficiency and precision. The objective of this work is to introduce a new method to simulate WECs in shallow waters and near-shore regions.

1.2 Current state of the art

1.2.1 Mathematical models

Nowadays, the simulation of WECs dynamics relies heavily on the use of tools based on Cummins equation [41] using hydrodynamic coefficients computed from linear potential flow (LPF) for the prediction of motions, loads, and power production. The LPF models are based on the small amplitude/small motion assumption and they are widely used for their simplicity and efficiency, e.g. see [128]. The linear wave model is the overall predominant hydrodynamic one used in wave energy studies. The hydrodynamic coefficients are computed by panel codes such as WAMIT [179] or Nemoh [9]. These coefficients are then used in the dynamic equations with convolution integrals to account for memory effects. The equations are solved in the time-domain and may include nonlinear effects from e.g. drag, power take off (PTO) and mooring forces, but the fundamental wave-body interaction and wave propagation remains linear. There are numerous models using this approach, e.g. the open-source model WEC-Sim from NREL [183] and the commercial code Ansys-Aqwa [6]. Although LPF models have been used successfully in few offshore applications [68], the small amplitude and small motion approximation is not valid in many cases such as WECs operating inside the resonance region and, especially, for survival cases. Besides, they can not account for nonlinear hydrodynamic effects which arise in case of non-constant and steepening seabed where waves are expected to exhibit nonlinear dynamics as steepening and energy transfer between harmonics.

More recently, thanks to the increase in computational power, more advanced nonlinear models became also available for WEC modelling. Nonlinear models include computational fluid dynamics (CFD), fully nonlinear potential flow (FNPF), nonlinear Foude-Krylov models and depth averaged wave models. Penalba et al. [146] had presented a review of all nonlinear methods for WEC modelling. CFD simulations have been employed for PA WECs in several cases, e.g. [119, 193, 143]. Compared to the linear LPF models, simulations based on volume of fluid Reynolds averaged Navier-Stokes (VOF-RANS) have the advantage of capturing all nonlinear dynamics that WECs and near-shore waves experiences, such as overtopping of the

WEC and breaking waves, that can impact greatly the predictions of the dynamics and subsequently, the design of WEC. In CFD models, the viscosity and vorticity of the fluid can be included in the governing equations. In particular, the solutions of turbulent flows are realistic representation of the physical problem. RANS equations are the most common method to solve turbulent flows, thanks to their reasonable computational cost and accuracy. As a matter of fact, it has been shown through RANS simulations, that LPF models can be unsuited for the optimization of WEC. Comparing the results by the two methods, it is clear that LPF over-predicts the power production, especially in the resonance region, unless ad hoc coefficients are calibrated [193, 143]. However, RANS experiments are still extremely costly, a simulation with a full sea state for a WEC may require as much as 150 000 CPU hours per sea-state simulation [63], but they are used because of high resolution results and the investigation of specific flow phenomena around offshore and near-shore structures.

For inviscid, non-compressible flow and non-breaking waves, the FNPF model can be used to improve the time computational performances of RANS simulations [188]. FNPF theory discard the assumption of small wave steepness, thus higher waves and finite body displacements can be evaluated. Sometimes dependent boundary conditions must be applied to the moving surfaces of the fluid and the wetted surface of the body. The boundary value problem (BVP) for the wetted surface has to be solved at each time step and it can be computationally demanding, and so is important to select an appropriate technique to keep the simulations efficient. Moreover, the FNPF does not include green water nor slamming of the waves, such that it can not be employed with all WECs applications. Because of this limitations, the use of FNPF for WECs has been sparse and in an early stage of development and often shadowed by RANS simulations. Nonetheless, it has been employed successfully in many researches for fixed and floating buoys surface piercing such as [57, 106], as well as for completely submerged body [86, 27, 116].

In shallow to intermediate waters with non-breaking waves, Boussinesq-type equations (BTE) provide an alternative to the FNPF model. BTE are a depth integrated family of equations that express the nonlinear wave hydrodynamics in horizontal dimensions only. This makes them computationally less demanding than complete 3D equations, and allows the use of nonlinear hydrodynamics also for a larger number of realisations of irregular sea states, as it can be required in optimization or in fatigue predictions. BTE are standard engineering wave models, e.g. [**bosi2018spectral**, 2, 147], used to predict nonlinear wave propagation in near-shore and coastal areas. See [23] for an extensive recent review. These models are used because of their computational efficiency and simplicity since the elimination of the vertical dimension from the problem avoids the handling of the time-dependent domain caused by the moving free surface. However truncated surface-piercing bodies are troublesome to handle by a depth-integrated wave model. In order to include truncated bodies in depth-integrated hydrodynamic models methods such as pressure patches [59], porosity layers [138] and slender ship approximations [33] have been used. None of these approaches includes the actual body in the discretization. The work of Jiang [96] on the 'unified' Boussinesq model is an exception. The technique proposed by Jiang is to decompose the problem domain into a free-surface and a body domains. Importantly, Jiang modelled also the domain under the body with a depth-integrated approach – hence the term 'unified'. In [111], Lannes has accurately analysed a similar wave-body setting. In his work, Lannes included nonlinear contributions using the nonlinear shallow water equations, thus extending the study of John [97]. Moreover, he derived analytical and semi-analytical solutions for the wave-body interaction problem in forced and decay motion, remaining within the

traditional shallow water limit. The same method introduced by Lannes has been discussed in [78] to solve 'roofed', congested shallow water flows.

1.2.2 Numerical methods

The description of the dynamics of WECs and waves through a mathematical model involve solving a system of partial differential equations (PDEs). These are solved with discretization schemes that approximate the original continuous model and can be treated numerically. Several discretization and resolution strategies for PDEs have been proposed [150], however we are going to focus on high order methods, which have a spatial accuracy of order equal or higher than three [180] and are especially desirable for simulating flows with smooth solutions and long time integrations. We briefly report the state of the art on high order methods. In [137, 165, 102, 172, 48], we have reviews of the state of the art of numerical models for propagating waves; here we outline the most important ones.

One of the most common and historically the first method used to solve PDEs is the finite difference method (FDM). FDM approximates the derivatives over a discrete grid using finite differences, thus converting the PDE system into a system of algebraic equation. The resolution of the new system is particularly well suited to be solved numerically, hence the widespread of this method in numerical analysis [85]. Moreover high order resolution [117, 88, 163] and even spectral-like convergence [115] can be reached. However, although regurlarly used in several applications, FDM presents some critical limitation. Xu et al. [190] points out that FDM are based on uniform Cartesian grid which for simulation of practical problems can become a disadvantage. Some methods, such as the coordinate transformation [46], have been introduced to solve FDM on non-uniform meshes but it is not clear if they preserve the accuracy and stability of the uniform original scheme. Moreover, it has been shown [194] that high order finite difference method present spurious solutions and might become unstable, especially close to the boundaries either by pollution given by a simplification of the scheme [44, 32] or caused by the discretization grid [194].

An alternative method is the finite element method (FEM) is based on a variational method of approximation of the PDE. The global domain is divided into a mesh of sub-domains which we will refer to as elements in what follows and in each elements are defined a set basis functions. The basis functions are systematically recombined to evaluate an approximation of the PDE's solution. The geometry of the elements of the mesh is put in relation to the one of the reference element using the Jacobian transformation matrix. Thanks to this approach, in principle the elements of a mesh can be of any shape as the PDE is solved on the reference one, permitting the simulation of very complex geometries. The Galerkin method [74] is generally used in the FEM to solve differential equations. The Galerkin method is a special case of the family of Weighted Residuals (WR) methods [40, 72] for which weighting functions are the same as interpolation functions. Typically, the PDEs are solved in their weak or variational formulation to reduce the requirement on differentiability of the function. Note that the boundary conditions are included weakly in the variational formulation of the system. In each element of the domain, a piecewise polynomial function is set as basis for the interpolation and weighting of the solution. This permits to construct a linear matrix formulation of the problem that can be solved with appropriate techniques [54].

The finite volume method (FVM) [118, 177] is another common method, which formulation allows the use of unstructured meshes and thus the accurate solution of problems with complex geometry. A small finite control volume surrounds each

node, in the node-centered approach, or each cell, in the cell-centered approach, of the computational discrete domain. The equations are integrated in the control volume and the fluxes are evaluated as surface integral on the interfaces. The FVM is conservative since the fluxes entering a volume are identical to the ones leaving the adjacent ones. Moreover, the method can handle discontinuous solutions. Several finite volume schemes exist according to whether they use structured [83, 152] or unstructured [31, 171, 5] grids. However, the FVM might presents difficulty in the accurate definition of derivatives. The Taylor-expansion method from the FDM is impossible since the computational grid is not necessarily orthogonal and equally spaced. Also, high order derivatives can not be lowered in order such as in the FEM method since FVM lacks of a mechanism like a weak formulation [184]. FVM is still widely used and exist several approaches to implement high order precision: Lacor et al. [109], for uniform Cartesian meshes had developed an implicit deconvolution step method or high-order polynomial reconstructions in each cells such ENO (Essentially Non-Oscillatory) and WENO (Weighted Essentially Non-Oscillatory) [162, 3] for either structured and unstructured grids.

If the construction of the elements and the polynomial basis functions of the FEM method are based on orthogonal functions, the method can be turned into an arbitrarily high-order accurate Spectral/*hp*-FEM method, also referred to as a Spectral Element Method (SEM) [169, 145]. When the interpolating nodes of the elements are positioned on the zeros of certain families of orthogonal function (Legendre or Chebyshev polynomials), the SEM reaches the highest interpolation accuracy. An advantage of the SEM over the other methods presented is that it permits the convergence both in the *h*- and *p*-adaptivity sense. This means that it is possible to refine the mesh, keeping the polynomial order constant (*h*-adaptivity) and using smaller elements to catch small-scale phenomena, or increase the polynomial order (*p*-adaptivity) to achieve an efficient convergence over large-scale features. The *hp*-adaptivity is a combination of the two types of adaptivity and it it can be employed to achieve optimal convergence [13]. The word "spectral" of the spectral/*hp*-FEM suggests the high order convergence rate of the method, that with the right choice of quadrature points and interpolating functions can be exponentially fast. The adaptivity to complex geometry, the fast convergence and the efficiency that results exploiting unstructured meshes with non constant polynomial order make the SEM a powerful method and it is gaining increasing interest in the field of CFD [99]. A recent review on the SEM is given in [191].

Boundary elements methods (BEM) [21, 77] have emerged as a powerful alternative to FEM and FDM, particularly in cases where where the domain extends to infinity. With BEM we denote any method for that approximates numerical solution of boundary integral equations by equations with known and unknown boundary states. Hence, it only requires discretization of the surface rather than the volume, i.e., the dimension of problems is reduced by one. Consequently, the necessary discretization effort is mostly much smaller and, moreover, meshes can easily be generated and design changes do not require a complete remeshing. The BEM is extensively used in the study of nonlinear ocean wave dynamics and wave-body interactions hydrodynamics [130]. In particular, BEM has been employed to solve the problem with fixed bodies as floating pontoon in coastal areas [187, 186] and refraction/diffraction problems with body that extends troughout the water column [174, 195], as well as moving bodies: [122], for example, shows results for forced motion bodies while free floating bodies had been presented in numerous studies [170, 34, 189, 16].

Because of the characteristics of fast convergence, adaptivity and efficiency, the

spectral/*hp*-FEM has been adopted in resolution of the mathematical models presented in this thesis. The spectral/*hp*-FEM has been successfully used in the simulation of complex flows [103, 161] and in a number of other applications and in particular oceanographic modelling [38, 135, 28]. High efficiency and accuracy is reached in the simulation of fully nonlinear flows [80, 55] and weakly nonlinear Boussinesq flows [60]. More importantly, in recent years, spectral/*hp*-FEM has been used in wave-body interaction problems: results for a wave scattered by a structure that extends to the seabed are presented for example in [60]. The case of truncated structures has been studied in [58, 57, 114] for fixed structures, while the simulations of free heaving structures has been been presented in [64, 20, 134, 166].

1.3   Outline of the manuscript

This thesis, whithin the MIDWEST project [132], aims to develop computationally efficient nonlinear models for the interaction between water waves and floating bodies in shallow water regimes. Although the model is not limited to applications in marine renewable energy, the rationale for developing a medium fidelity wave-body model is found in the present state of modelling WECs in nearshore waters. As discussed in section 1.2, the simulation of WEC is commonly based either on LPF models, that are efficient but proven to be too simplistic, or VOF-RANS models, that are often too computationally expensive to be used in many applications whether very precise. Thus, we have focused on medium fidelity model, to combine efficiency and precision. The interest on fast and precise model for wave-body interaction arises not only from the simulation of WEC but several application from coastal or naval engineering. The model proposed can be applied for example to the interaction of waves and ships [43]. Moreover, this interaction is the one created in ports or shallow channels and in lagoons by ships and the study of this can be of interest on their design or on the management of navigation and traffic [17]. Floating waves attenuators or breakwater devices are other fields of interest. These are floating structures, which provide protection from external waves to facilities nearshore such as small marinas, harbours or delicate coastal environment and they have proved to be reliable in many cases and substantially cheaper than the traditional ones, particularly in case of deep (more than 6 meters) or unstable seabed. They can be easily moved, rearranged and have a lower ecological impact. The evaluation of their effectiveness and design presents some interesting challenges since intense nonlinearities, wave breaking and over-topping effects arise from the interaction of the attenuator and the shallow water waves [126, 107, 127].

The MIDWEST project [132] objective is to develop a multi-fidelity tools that combines wave models of different fidelity, from LPF to RANS VOF models. Following these requirements, we have proposed a depth-integrated unified Boussinesq model for nonlinear wave-body interaction based on the unified approach introduced by Jiang [96]. Adapting the original idea in terms of governing equations and discretizations, we employ a spectral/*hp* finite element method for the simulation of nonlinear and dispersive waves interacting with fixed and heaving bodies. In particular, we employ the continuous spectral/*hp* element method [99] inside each domain, and implement flux-based coupling conditions between domains in line with the discontinuous Galerkin spectral/*hp* element method [37]. This results in a new efficient and accurate model that simulates the wave propagation and the nonlinear interaction of waves with fixed and heaving bodies. However, as all models

based on Boussinesq-type equations, the model is limited to shallow and interme-
diate depth regimes. The use of spectral/*hp* elements gives support for the use of
adaptive meshes for geometric flexibility and high-order accurate approximations
makes the scheme computationally efficient. The current study presents the under-
lying formulation of the method as well as verification and validation of the numer-
ical model.

This work is structured as follows. In section 2.2 we derive and present the gov-
erning equations based on the enhanced Boussinesq-type equations of Madsen and
Sørensen [124]. The equations for body domain are defined and their properties are
shown. Furthermore, in section 2.6, we illustrate the types of interactions that we
are going to analyse. The 1D numerical discretisation in space and time is described
in chapter 3. In particular we discuss the formulation and the coupling between free
surface domain and the body constrained domain (sections 3.3 – 3.5), the spectral
element method, the time discretization and the acceleration equation for the body
motion in sections 3.2, 3.4 and 3.5. Chapter 4 shows the results of the 1D model: 4.1
presents a convergence study; section 4.2 compares the numerical results of the hy-
drostatic case to analytical and semi-analytical solutions. We have validated the non
hydrostatic 1D model against cases found in literature, in particular 4.3 shows the
results for a fixed pontoon while the heaving body test cases are presented in sec-
tion 4.4, first the single heaving body results are compared against LPF and RANS
simulations, then a proof-of-concept with two bodies in series is shown. The model
is expanded to two dimensions in chapter 5, following the same scheme of the 1D
derivation and chapter 6 displays the 2D results. Finally, we have implemented
a latching control technique on the body movement in chapter 7. This technique
controls the movement of the body to improve the response to the wave swell in
resonance conditions. Conclusions and follow up are in chapter 8.

1.4 Main contribution

The proposed wave-body extension of Boussinesq-type equations for wave-induced
motions is new to the wave energy sector and the numerical implementation will
use state-of-the-art methods from scientific computing in order to achieve maximal
computational efficiency. This is a clear step forward compared to the linear hy-
drodynamic models used today. Boussinesq models have an application window
in terms of dispersion and nonlinearity, making them mainly applicable in the shal-
low/intermediate depth region. However, the application window can in the future
be extended further into the deep water region by considering more nonlinear and
dispersive terms, at the cost of more complex equations and somewhat more costly
computations. The project will provide tools that can yield more reliable estimates
of predicted body movement response to the wave excitation which it will be linked
to the power production and loads on the WEC and ultimately to a better estimation
of the cost of energy.

A fundamental aspect of the project has been also the use of spectral/*hp* element
method in the numerical discretization of the model. Although the other methods,
such as BEM or FEM, are more common in the discretization of wave-body interac-
tion problems, SEM has a great accuracy without compromising the efficiency of the
computations, reaching the same precision as the other methods but at a fraction of
the cost and memory.

Peer reviewed journals and conference proceedings:

— Eskilsson, C., Palm, J., Engsig-Karup, A.P., Bosi, U. and Ricchiuto, M. (2015, September). Wave induced motions of point-absorbers: a hierarchical investigation of hydrodynamic models. In 11th European Wave and Tidal Energy Conference (EWTEC). Nantes, France.
— Bosi, U., Engsig-Karup, A. P., Eskilsson, C., Ricchiuto, M., Solaï E. (2018, July). A high-order spectral element unified Boussinesq model for floating point absorbers. In proceeding ICCE 2018-36th International Conference on Coastal Engineering 2018.
— Bosi, U., Engsig-Karup, A. P., Eskilsson, C., Ricchiuto, M. (2019). A spectral/*hp* element depth-integrated model for nonlinear wave-body interaction. Computer Methods in Applied Mechanics and Engineering. 348, pp.222-249.

Presentations to national and international conferences:
— EWTEC 2015: 11th European Wave and Tidal Energy Conference (EWTEC); Nantes (France); 6-11 September, 2015.
— GdR EMR: Ecole thématique sur les technologies EMRs (éolien en mer, hydrolien et houlomoteur); Nantes (France), 19-20 October, 2016.
— HONOM 2017: European Workshop on High Order Nonlinear Numerical Methods for Evolutionary PDEs: Theory and Applications; Stuttgart (Germany); 27-31 March 2017.
— FEF 2017: 19th International Conference on Finite Elements in Flow Problems; Rome (Italy), 5-7 April, 2017.
— ICCE 2018: 36th International Conference on Coastal Engineering 2018; Baltimore, MD (US), 30 July - 3 August, 2018.
— MARINE 2019: VIII International Conference on Computational Methods in Marine Engineering; Göteborg (Sweden), 13-15 May, 2019.

In preparation:
— Eskilsson et al.: benchmarking paper.
— Bosi, U., Engsig-Karup, A. P., Eskilsson, C., Ricchiuto, M. Depth averaged spectral/*hp* element models of nonlinear wave-body interaction in one and two dimensions.

Chapter 2

Governing equation

Sommaire

2.1 Introduction

In the coastal and marine engineering community, the mathematical modelling of waves has gained an important place to complement the more expensive and time consuming physical experiments. This is also true for the studies of wave energy converters (WECs). As discussed in the introduction, wave body interactions can be simulated using either linear models, weakly or fully nonlinear potential approximations, and VOF-RANS type models (NS in the following). However, for the design of WECs nonlinear effects play a non negligible role. This makes the linear models inappropriate to account for some phenomena. On the opposite, fully nonlinear, three dimensional NS equations can well reproduce the fully nonlinear, dispersive effects, as well as those related to vorticity and viscous dissipation. They remain however too computationally costly, in spite of the continuous evolution and growth in computer power. Potential models provide an intermediate compromise. They have the capability to account for full nonlinear and dispersive effects. However, the development of efficient and accurate formulations for wave interacting with moving water piercing bodies is still a subject of research. For near-shore as well as in relatively deep waters, the coastal engineering community has used for a long time asymptotic depth-averaged approximations. Following this approach,

our aim in this work is to use Boussinesq-type equations for wave-body interaction. Boussinesq equations are a family of approximation of the incompressible Euler equations. These equations can be derived from the Euler's equations by combining a depth averaging procedure with asymptotic expansions. These expansions are expressed in terms of two main dimensionless parameters. The first is the dispersion parameter μ

$$\mu = \kappa h, \text{ with } \kappa \lambda = 2\pi, \tag{2.1}$$

where h is the reference water depth, λ the wavelength and κ the wave number. Clearly, in shallow waters, or for very long waves this parameter can be assumed to be small. Depending on the order of magnitude assumed for μ, one can obtain approximations with different application windows. The simplest models is obtained by considering a zeroth order approximation, which provides the well known hydrostatic Nonlinear Shallow Water (NSW) model. This model gives a good representation of nonlinear waves as long as the dispersion parameter remains $\mu \leq \pi/20$. To account for the effects of shorter waves, higher order correction terms can be added. When doing so is customary to distinguish waves for which these effects are weakly or fully nonlinear. This is done introducing the nonlinearity parameter ε

$$\varepsilon = \frac{A}{h}, \tag{2.2}$$

with A the wave amplitude. For fully non-linear models $\epsilon \approx 1$, while weakly nonlinear models are obtained under the hypothesis that

$$\varepsilon \approx \mu^2 < 1. \tag{2.3}$$

In this chapter, we will follow this derivation procedure to arrive at the depth averaged approximations used in our numerical simulations. We will repeat the formal derivation in one space dimension. The multi-dimensional extension will be discussed, without formal derivation, in chapter 5. The derivation is done following the unified approach initially introduced by Jiang [96]. In this approach the domain is divided in two regions: Ω_w, the outer or free surface domain and Ω_b, the area under the body. We will only consider configurations in which the water-body interface corresponds to a straight vertical wall. This avoids having to deal with the triple point water-air-body and track its position. Moreover, only heave motion is allowed to simplify the model and to reproduce the most relevant motion for point absorber WECs. Besides the model derivation, we also discuss additional elements as the conservation of energy, the flow coupling between the different domains. and the construction of analytical or semi-analytical solutions.

This chapter is organized as followed. Section 2.2 considers the derivation of the free surface and the body equations. In particular, we consider the coupling of the free surface and body domains in section 2.2.3. In section 2.3, we discuss the added mass evaluation in case of free floating bodies. A short summary of the model is presented in section 2.4. Finally, in sections 2.5 and 2.6 we discuss the generation and absorption of waves and some analytical solution for the wave-body interaction.
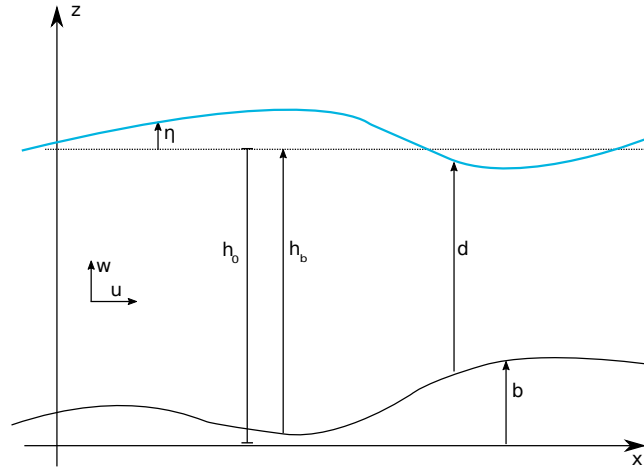
FIGURE 2.1 – 1D setup of the free surface problem.

2.2 Derivation of Boussinesq equations

2.2.1 Free surface domain

We start by introducing the notation that is going to be used throughout all the thesis. The model for the free surface problem is going to be presented and derived in two dimensions (x, z) (one horizontal plus vertical), however the procedure is general [112]. Multidimensional expansion will be considered, however without derivation, in chapter 5. The free surface domain is denoted as Ω_w. As shown in figure 2.1, we consider a Cartesian coordinate system. We recall that the characteristic scales for the flow are the wave amplitude A, wavelength λ and wave period T. The bathymetry is denoted by $b(x)$. The water depth $d(x, t)$ is the main unknown in the outer domain and it is defined as

$$d(x, t) = h_0 + \eta(x, t) - b(x) \tag{2.4}$$

where $\eta(x, t)$ is the free surface elevation. We define the parameters of reference still water depth h_0 and still water depth $h_b(x) = h_0 - b(x)$. The remaining unknowns are the vertical velocity $w(x, z, t)$, the horizontal velocity $u(x, z, t)$ and the pressure $p(x, z, t)$.

Considering the water as a fluid with constant density ρ_w and neglecting the effects of the free surface tension and viscosity, the flow dynamics can be described by the free surface incompressible Euler's equations. The system equations are the conservation of mass equation

$$u_x + w_z = 0, \tag{2.5}$$

and the conservation of momentum equations

$$\begin{cases} u_t + uu_x + wu_z + \frac{1}{\rho_w} p_x = 0, \\ w_t + uw_x + ww_z + \frac{1}{\rho_w} p_z + g = 0. \end{cases} \tag{2.6}$$

where the subscripts $(\cdot)_x$, $(\cdot)_z$ and $(\cdot)_t$ represent respectively the derivative in the x direction, z direction and time.

The boundary condition at the free surface, often called the *kinematic* condition, is:

$$w_f = d_t + u_f d_x, \quad z = b + d, \tag{2.7}$$

where we have defined $u_f = u(x, b + d, t)$ and $w_f = w(x, b + d, t)$, the values of the velocities at the free surface. The *dynamic* condition is the boundary condition of the pressure at the free surface:

$$p_f - p_{air} = 0, \quad z = b + d. \tag{2.8}$$

Commonly, the atmospheric pressure is assumed to be constant. We can thus replace the pressure p by its relative value

$$\Pi = p - p_{air}, \tag{2.9}$$

verifying the boundary condition $\Pi_f = 0$. At seabed level $z = b$, we have the impermeability condition, which is similar to the kinematic free surface condition and reads in general

$$w_s = b_t + u_s b_x = u_s b_x, \quad z = b, \tag{2.10}$$

where $u_s = u(x, b, t)$ and $w_s = w(x, b, t)$ are the values of the velocities at the seabed, and where the second equality is a consequence of having assumed $b_t = 0$. Finally, the models considered in this work are obtained under the hypothesis of irrotational flow which in 1D reads

$$u_z = w_x. \tag{2.11}$$

Dimensional analysis

We introduce here the nondimensional form of the problem. This is done as a first step toward the simplification of the Euler's equations. The nondimensional variables are evaluated dividing all the physical quantities by a set of selected reference scales for mass, time, length, flow speed and pressure. The parameters of dispersion μ (2.1) and nonlinearity ε (2.2) naturally appear in this process. We have the following definitions.

Definition 1. *We define the nondimensional variables as*

$$\tilde{t} = \mu \frac{\sqrt{gh_0}}{h_0} t, \quad \tilde{x} = \frac{\mu}{h_0} x, \quad \tilde{z} = \frac{z}{h_0}, \quad \tilde{h}(\tilde{x}) = \frac{h(x)}{h_0} = 1, \quad \tilde{\eta}(\tilde{x}, \tilde{t}) = \frac{\eta(x, t)}{\varepsilon h_0},$$

$$\tilde{d}(\tilde{x}, \tilde{t}) = \varepsilon \tilde{\eta}(\tilde{x}, \tilde{t}) + \tilde{h} = \varepsilon \tilde{\eta} + 1 = \frac{d(x, t)}{h_0}, \quad \tilde{\Pi} = \frac{1}{\varepsilon g h_0} \frac{p - p_{air}}{\rho_w} \tag{2.12}$$

$$\tilde{u} = \frac{1}{\varepsilon \sqrt{gh_0}} u, \quad \tilde{q} = \tilde{d}\tilde{u}, \quad \tilde{w} = \frac{\mu}{\varepsilon \sqrt{gh_0}} w, \quad \tilde{g} = 1.$$

We also introduce the nonlinearity bathymetry parameter

$$\beta = \frac{b_0}{h_0},$$

where b_0 is the characteristic variation of the bathymetry. Thus, we define the non-dimensional bathymetry

$$\tilde{b}(\tilde{x}) = \frac{b(x)}{\beta h_0} = \frac{b(x)}{b_0}. \tag{2.13}$$

Dropping the tilde notation, we write the incompressible Euler's equations in dimensionless form as:

$$\mu^2 u_x + w_z = 0, \tag{2.14a}$$

$$u_t + \varepsilon \left(u u_x + \frac{1}{\mu^2} w u_z \right) + \Pi_x = 0, \tag{2.14b}$$

$$w_t + \varepsilon \left(u w_x + \frac{1}{\mu^2} w w_z \right) + \Pi_z + 1 = 0. \tag{2.14c}$$

The nondimensional boundary conditions and irrotationality constraint can be written as

$$\mu^2 \left(\eta_t + \varepsilon u_f \eta_x \right) - w_f = 0 \qquad \text{at } z = 1 + \varepsilon\eta, \tag{2.15a}$$

$$\Pi = 0 \qquad \text{at } z = 1 + \varepsilon\eta, \tag{2.15b}$$

$$\beta\mu^2 u_s b_x - w_s = 0 \qquad \text{at } z = \beta b. \tag{2.15c}$$

$$u_z = w_x. \tag{2.15d}$$

Depth averaging and asymptotic analysis

We are going to derive the asymptotic approximations of the Euler equations in terms of depth averaged quantities. We will in particular see the evolution equations for the free surface level η and depth d, as well as for the depth averaged velocity $\bar{u}(x,t)$:

$$\bar{u} = \frac{1}{1 + \varepsilon\eta - \beta b} \int_{\beta b}^{1+\varepsilon\eta} u \, dz. \tag{2.16}$$

A variable playing a major role is also the volume flux q

$$q := \int_{\beta b}^{1+\varepsilon\eta} u \, dz = (1 + \varepsilon\eta - \beta b)\bar{u}$$

One of the main tools used in the following analysis and reported here for completeness is the well known Leibnitz's integration rule, reading:

$$\left(\int_{\zeta(x)}^{\xi(x)} f(x,z) dz \right)_x = \int_{\zeta(x)}^{\xi(x)} f_x(x,z) dz + \xi_x(x)f(x,\xi(x)) - \zeta_x(x)f(x,\zeta(x)), \tag{2.17}$$

where f, ζ and ξ and continuous, differentiable functions.

Water elevation equation.   Integrating over the water depth eq.(2.14a), we obtain:

$$\int_{\beta b}^{1+\varepsilon\eta} (\mu^2 u_x + w_z) dz = 0. \tag{2.18}$$

Applying Leibnitz rule, it can be recast as

$$w_f - w_s + \left(\int_{\beta b}^{1+\varepsilon\eta} \mu^2 u \, dz \right)_x + \beta\mu^2 b_x u_s - \mu^2 \varepsilon\eta_x u_f = 0. \tag{2.19}$$

Substituting the kinetic and dynamic conditions eqs. (2.15a) and (2.15c) to w_f and w_s and using the definition of the depth averaged velocity eq. (2.16):

$$\eta_t + (d\bar{u})_x = 0 \tag{2.20}$$

or equivalently

$$\eta_t + q_x = 0 \tag{2.21}$$

This is commonly called non-dimensional *mass equation* or *continuity equation* and it represents the conservation of volume (or equivalently mass) of water in the domain. The mass equation is exact and is a direct consequence of combination of volume conservation with the boundary conditions of the Euler's equations.

To obtain an evolution equation for the depth averaged horizontal velocity $\bar{u}$, we integrate eq. (2.14b) over the depth:

$$\int_{\beta b}^{1+\varepsilon\eta} \left(u_t + \varepsilon \left(uu_x + \frac{1}{\mu^2} wu_z \right) + \Pi_x \right) dz = 0. \tag{2.22}$$

Evaluating each terms separately:

$$\int_{\beta b}^{1+\varepsilon\eta} u_t dz \stackrel{\text{eq. (2.17)}}{=} \left(\int_{\beta b}^{1+\varepsilon\eta} u dz \right)_t - \varepsilon\eta_t u_f + \beta b_t u_s = \left(\int_{\beta b}^{1+\varepsilon\eta} u dz \right)_t - \varepsilon\eta_t u_f,$$

$$\int_{\beta b}^{1+\varepsilon\eta} \left(\frac{u^2}{2} \right)_x dz \stackrel{\text{eq. (2.17)}}{=} \left(\int_{\beta b}^{1+\varepsilon\eta} \left(\frac{u^2}{2} \right) dz \right)_x - \varepsilon\eta_x \frac{u_f^2}{2} + \beta b_x \frac{u_b^2}{2},$$

$$\int_{\beta b}^{1+\varepsilon\eta} u_z w dz = uw\big|_{\beta b}^{1+\varepsilon\eta} - \int_{\beta b}^{1+\varepsilon\eta} uw_z dz =$$

$$\stackrel{\text{eq. (2.14a)}}{=} u_f w_f - u_s w_s + \mu^2 \int_{\beta b}^{1+\varepsilon\eta} \left(\frac{u^2}{2} \right)_x dz$$

$$\stackrel{\text{eqs. (2.15a), (2.15c)}}{=} \mu^2 \left(\eta_t u_f + \varepsilon\eta_x u_f \right) + \beta\mu^2 b_x u_s + \mu^2 \int_{\beta b}^{1+\varepsilon\eta} \left(\frac{u^2}{2} \right)_x dz,$$

$$\int_{\beta b}^{1+\varepsilon\eta} \Pi_x dz \stackrel{\text{eq. (2.17)}}{=} \left(\int_{\beta b}^{1+\varepsilon\eta} \Pi dz \right)_x - \varepsilon\eta_x \Pi_f + \beta b_x \Pi_s$$

$$\stackrel{\text{eq. (2.15b)}}{=} \left(\int_{\beta b}^{1+\varepsilon\eta} \Pi dz \right)_x + \beta b_x \Pi_s.$$

$$\tag{2.23}$$

where $\Pi_s = p(z = b)$ is the pressure at the seabed. Collecting all the terms and simplifying, we obtain

$$(d\bar{u})_t + \varepsilon(d\bar{u^2})_x + (d\overline{\Pi})_x + \beta b_x \Pi_s = 0, \tag{2.24}$$

having introduced the depth averaged pressure $\overline{\Pi}$

$$\overline{\Pi} = \frac{1}{1 + \varepsilon\eta - \beta b} \int_{\beta b}^{1+\varepsilon\eta} \Pi dz.$$

Eq. (2.24) is called the *momentum* equation and with eq. (2.20), they constitute the building blocks for all the asymptotic systems that we are going to presents.

Asymptotic velocity profiles. Starting from eq. (2.14a), we are going to derive the expression for the vertical and horizontal velocity components in function of the

depth averaged horizontal velocity. We start by integrating eq. (2.14a) from the bottom to a generic depth z:

$$
\begin{aligned}
w(z) \overset{\text{eq. (2.17)}}{=} \; & w_s - \mu^2 \left(\left(\int_{\beta b}^z u dz \right)_x - \beta b_x u_s \right) \\
\overset{\text{eq. (2.15c)}}{=} \; & -\mu^2 \left(\int_{\beta b}^z u dz \right)_x .
\end{aligned}
\tag{2.25}
$$

Similarly, integrating the irrotationality condition and using eq. (2.25) leads to

$$
u(z) = u_s + \int_{\beta b}^z w_x dz = u_s - \mu^2 \int_{\beta b}^z \left(\int_{\beta b}^z u dz \right)_{xx} dz.
\tag{2.26}
$$

We can now express the vertical velocity in terms of the bottom horizontal velocity by substituting eq. (2.26) into eq. (2.25), leading to the $\mathcal{O}(\mu^4)$ estimate:

$$
w(z) = -\mu^2 \left(\int_{\beta b}^z u_s dz \right)_x + \mathcal{O}(\mu^4) = -\mu^2 (u_s(z - \beta b))_x + \mathcal{O}(\mu^4),
\tag{2.27}
$$

while for the horizontal velocity, integrating again the irrotationality condition, we can now improve the estimate as follows:

$$
\begin{aligned}
u(z) &= u_s - \mu^2 \int_{\beta b}^z (u_s(z - \beta b))_{xx} dz + \mathcal{O}(\mu^4) \\
&= u_s - \mu^2 \left((u_s)_{xx} \int_{\beta b}^z (z - \beta b) dz - u_s \int_{\beta b}^z \beta b_{xx} dz \right) + \mathcal{O}(\mu^4) \\
&= u_s - \mu^2 \left((u_s)_{xx} \frac{(z - \beta b)^2}{2} dz - \beta u_s b_{xx} (z - \beta b) \right) + \mathcal{O}(\mu^4).
\end{aligned}
\tag{2.28}
$$

The depth averaged velocity can be now expressed as a function of the seabed velocity u_s using eq. (2.28):

$$
\bar{u} = \frac{1}{1 + \varepsilon \eta - \beta b} \int_{\beta b}^{1 + \varepsilon \eta} u dz = u_s - \mu^2 \left((u_s)_{xx} \frac{d^3}{6} dz - \beta u_s b_{xx} \frac{d^2}{2} \right) + \mathcal{O}(\mu^4).
\tag{2.29}
$$

Note that within $\mathcal{O}(\mu^2)$, we have a simple relation between the bottom velocity and the depth averaged one

$$
\bar{u} = u_s + \mathcal{O}(\mu^2).
\tag{2.30}
$$

This can be used to invert eq. (2.29) leading to:

$$
u_s = \bar{u} - \mu^2 \left(\bar{u}_{xx} \frac{d^3}{6} - \beta \bar{u} b_{xx} \frac{d^2}{2} \right) + \mathcal{O}(\mu^4).
\tag{2.31}
$$

We can, finally, express the horizontal and vertical velocity profiles only in terms of the depth averaged velocity as

$$
u(z) = \bar{u} - \mu^2 \left(\bar{u}_{xx} \left(\frac{(z - b)^2}{2} - \frac{d^2}{6} \right) + \beta \bar{u} b_{xx} \left(\frac{d}{2} - z + \beta b \right) \right) + \mathcal{O}(\mu^4),
\tag{2.32}
$$

$$
w(z) = -\mu^2 (\bar{u}(z - \beta b))_x + \mathcal{O}(\mu^4).
\tag{2.33}
$$

Evaluation of nonlinear term. To be able to use eq. (2.24) to define the approximated systems, we want to express every term dependent on the depth averaged velocity. The nonlinear term $\bar{u^2}$ at precision $\mathcal{O}(\mu^4)$ becomes

$$
\begin{aligned}
\bar{u^2} &= \frac{1}{d} \int_{\beta b}^{1+\varepsilon\eta} u^2 dz \\
&= \frac{1}{d} \int_{\beta b}^{1+\varepsilon\eta} \left[\bar{u} - \mu^2 \left(\bar{u} \left(\frac{(z-\beta b)^2}{2} - \frac{d^2}{6} \right) + \beta \bar{u} b_{xx} \left(\frac{d}{2} - z + \beta b \right) \right) \right]^2 dz + \mathcal{O}(\mu^4) \\
&= \bar{u}^2 + \mathcal{O}(\mu^4).
\end{aligned}
\tag{2.34}
$$

Asymptotic pressure profile. The pressure is evaluated integrating from depth z to the free surface $1 + \varepsilon\eta$ eq. (2.14c)

$$
\Pi(z) = (1 + \varepsilon\eta - z) + \int_z^{1+\varepsilon\eta} w_t dz + \varepsilon \int_z^{1+\varepsilon\eta} u w_x dz + \frac{\varepsilon}{\mu^2} \int_z^{1+\varepsilon\eta} w w_z dz. \tag{2.35}
$$

evaluating each integral separately, we get:

$$
\begin{aligned}
\int_z^{1+\varepsilon\eta} w_t dz &\overset{\text{eq. (2.33)}}{=} -\mu^2 \int_z^{1+\varepsilon\eta} \left((\bar{u}(z-\beta b))_x + \mathcal{O}(\mu^2) \right)_t dz \\
&= -\mu^2 \int_z^{1+\varepsilon\eta} (\bar{u}_x(z-\beta b) - \beta \bar{u} b_x)_t dz + \mathcal{O}(\varepsilon\mu^4) \\
&= -\mu^2 \left[\bar{u}_{xt} \left(\frac{d^2}{2} - \frac{(z-\beta b)^2}{2} \right) - \beta \bar{u}_t b_x (1 + \varepsilon\eta - z) \right] + \mathcal{O}(\varepsilon\mu^4), \\[2mm]
\int_z^{1+\varepsilon\eta} u w_x dz &\overset{\text{eqs. (2.33),(2.32)}}{=} -\mu^2 \int_z^{1+\varepsilon\eta} (\bar{u} + \mathcal{O}(\mu^2)) \left((\bar{u}(z-\beta b))_x + \mathcal{O}(\mu^2) \right)_x dz \\
&= -\mu^2 \bar{u} \int_z^{1+\varepsilon\eta} (\bar{u}(z-\beta b))_{xx} dz + \mathcal{O}(\varepsilon\mu^4) \\
&= -\mu^2 \bar{u} \bar{u}_{xx} \left(\frac{d^2}{2} - \frac{(z-\beta b)^2}{2} \right) \\
&\qquad + \mu^2 \bar{u} (2\beta \bar{u}_x b_x + \bar{u} b_{xx})(1 + \varepsilon\eta - z) + \mathcal{O}(\varepsilon\mu^4), \\[2mm]
+ \int_z^{1+\varepsilon\eta} \left(\frac{w^2}{2} \right)_z dz &\overset{\text{eq. (2.33)}}{=} \frac{\mu^4}{2} \int_z^{1+\varepsilon\eta} \left((\bar{u}(z-\beta b))_x + \mathcal{O}(\mu^2) \right)_z^2 dz \\
&= \frac{\mu^4}{2} \int_z^{1+\varepsilon\eta} (\bar{u}_x(z-\beta b) - \beta \bar{u} b_x)_z^2 dz + \mathcal{O}(\varepsilon\mu^4) \\
&= \mu^4 \int_z^{1+\varepsilon\eta} (\bar{u}_x(\bar{u}(z-\beta b))_x)_z dz + \mathcal{O}(\varepsilon\mu^4) \\
&= \mu^4 \left[\bar{u}_x^2 \left(\frac{d^2}{2} - \frac{(z-\beta b)^2}{2} \right) - \beta \bar{u} \bar{u}_x b_x (1 + \varepsilon\eta - z) \right] + \mathcal{O}(\varepsilon\mu^4),
\end{aligned}
\tag{2.36}
$$

the pressure at depth z can thus be expressed within $\mathcal{O}(\varepsilon\mu^4)$ as

$$
\begin{aligned}
\Pi(z) = {} & (1 + \varepsilon\eta - z) - \mu^2 \left[\bar{u}_{xt} \left(\frac{d^2}{2} - \frac{(z - \beta b)^2}{2} \right) - \beta \bar{u}_t b_x (1 + \varepsilon\eta - z) \right] \\
& - \varepsilon\mu^2 \bar{u} \left[\bar{u}_{xx} \left(\frac{d^2}{2} - \frac{(z - \beta b)^2}{2} \right) - (2\beta \bar{u}_x b_x + \beta \bar{u} b_{xx})(1 + \varepsilon\eta - z) \right] \\
& + \varepsilon\mu^2 \left[\bar{u}_x^2 \left(\frac{d^2}{2} - \frac{(z - \beta b)^2}{2} \right) - \beta \bar{u} \bar{u}_x b_x (1 + \varepsilon\eta - z) \right] + \mathcal{O}(\varepsilon\mu^4).
\end{aligned} \tag{2.37}
$$

This profile can be integrated to derive an explicit expression for the depth averaged pressure. The result is

$$
\begin{aligned}
d\overline{\Pi} = {} & \frac{d^2}{2} - \mu^2 \left(\bar{u}_{xt} \frac{d^3}{3} - \beta \bar{u}_t b_x \frac{d^2}{2} \right) \\
& - \varepsilon\mu^2 \bar{u} \left(\bar{u}_{xx} \frac{d^3}{3} - \beta(2\bar{u}_x b_x + \bar{u} b_{xx}) \frac{d^2}{2} \right) \\
& + \varepsilon\mu^2 \left(\bar{u}_x^2 \frac{d^3}{3} - \beta \bar{u} \bar{u}_x b_x \frac{d^2}{2} \right) + \mathcal{O}(\varepsilon\mu^4).
\end{aligned} \tag{2.38}
$$

Eq. (2.37) permits to evaluate also an expression for the pressure at the seabed Π_s:

$$
\Pi_s = \Pi(z = \beta b) = d - \mu^2 \left(\bar{u}_{xt} \frac{d^2}{2} - \beta \bar{u}_t b_x d \right) + \mathcal{O}(\mu^4, \varepsilon\mu^2). \tag{2.39}
$$

In this work we have focused on the interaction between free surface waves and fixed or moving bodies. For this reason, the effects of a variable bathymetry have been neglected, even though, away from dry areas, including them can be done without major challenges [62, 144]. For this reason, the models used in the simulations are obtained under the assumption

$$
b(x) = b_0 = 0. \tag{2.40}
$$

Thus the terms dependent on the bathymetry, i.e. $\beta b_x \Pi_z$, are neglected.

Nonlinear shallow water equations

The first and simplest approximation of the Euler's equations that can be derived is the nonlinear shallow water model (NSW). The approximation hypothesis on which this model is based on is $\varepsilon \approx 1$ and $\mu^2 \ll 1$, such that all the terms of order $\mathcal{O}(\mu^2)$ or higher can be neglected. Substituting the eqs. (2.34) and (2.38) into the equation for horizontal velocity eq. (2.24), the NSW nondimensional system of equations reads:

$$
\begin{aligned}
d_t + (d\bar{u})_x &= 0, \\
(d\bar{u})_t + \varepsilon(d\bar{u}^2)_x + d d_x &= \mathcal{O}(\mu^2).
\end{aligned} \tag{2.41}
$$

Going back to dimensional variables and using the depth averaged flux $\bar{q} = d\bar{u}$, the dimensional NSW is

$$
d_t + \bar{q}_x = 0, \tag{2.42a}
$$

$$
\bar{q}_t + \left(\frac{\bar{q}^2}{d} \right)_x + g d d_x = 0. \tag{2.42b}
$$

We remark that the system can also be expressed in terms of water level and velocity by simple manipulations.

Total pressure formulation.   For later use, we introduce here the definition of hydrostatic pressure $P = gd$ so that we can rewrite eqs. (2.42) as

$$P_t + g\bar{q}_x = 0, \tag{2.43a}$$

$$\bar{q}_t + \left(\frac{\bar{q}^2}{d}\right)_x + dP_x = 0. \tag{2.43b}$$

Weakly-nonlinear Boussinesq-type models

Boussinesq models with improved dispersion characteristics can be derived including higher order terms of the asymptotic development. In this work, we will focus on the so-called weakly-nonlinear models, based on the following assumption:

$$\mu^2 \ll 1, \ \varepsilon \ll 1 \text{ and } \beta \ll 1 \rightarrow \varepsilon \approx \mu^2 \text{ and } \beta \approx \mu^2.$$

These hypotheses lead to models for which only the shallow water component is fully nonlinear, while the dispersive corrections only involve linear operators. In practice, we will neglect the terms of order $\mathcal{O}(\varepsilon\mu^2, \beta\mu^2, \mu^4)$ and higher.

Several models can be derived within the assumption of weak nonlinearity, for example the model of Peregrine [147] or Abbott [2], or the enhanced models by Madsen and Sørensen [124] and Nwogu [140]. These models involve a set of two PDEs, one that describes the conservation of the mass and one the conservation of momentum. In this work, we have considered the Abbott model and the Madsen and Sørensen model in the amplitude-flux formulation.

Abbott model

The nondimensional Abbott model is obtained substituting eqs. (2.34) and (2.38) into eq. (2.24) and neglecting all the terms of order $\mathcal{O}(\epsilon\mu^2, \mu^4)$. Recalling the $b(x) = 0$, we obtain

$$\begin{aligned} d_t + (d\bar{u})_x &= 0, \\ (d\bar{u})_t + \varepsilon(d\bar{u}^2)_x + gdd_x &= \mu^2\left(\frac{d^3}{3}\bar{u}_{xt}\right)_x + \mathcal{O}(\varepsilon\mu^2, \mu^4). \end{aligned} \tag{2.44}$$

Using the fact that $d = 1 + \varepsilon\eta$, we can manipulate the dispersive term as

$$\mu^2\left(\frac{d^3}{3}\bar{u}_{xt}\right)_x = \mu^2\left(\frac{(1+\varepsilon\eta)^3}{3}\bar{u}_{xt}\right)_x = \mu^2\frac{1}{3}(d\bar{u}_{xt})_x + \mathcal{O}(\varepsilon\mu^2, \mu^4). \tag{2.45}$$

Proceeding similarly, we also have

$$\mu^2(d\bar{u}_{xt})_x = \mu^2(d\bar{u})_{xxt} + \mathcal{O}(\varepsilon\mu^2, \mu^4). \tag{2.46}$$

As a consequence, within the same asymptotic accuracy, we can write

$$\begin{aligned} d_t + \bar{q}_x &= 0, \\ \bar{q}_t + \left(\frac{\bar{q}^2}{d}\right)_x + gdd_x &= \frac{h_0^2}{3}\bar{q}_{xxt}, \end{aligned} \tag{2.47}$$

which is normally known as Abbott model [71].

As for the NSW model, we can write the Abbott eqs. (2.47) in terms of $P = gd$ and flux as

$$P_t + g\bar{q}_x = 0,$$
$$\bar{q}_t + \left(\frac{\bar{q}^2}{d}\right)_x + dP_x - \frac{h_0^2}{3}\bar{q}_{xxt} = 0. \tag{2.48}$$

Madsen and Sørensen model

The model developed by Madsen and Sørensen (MS) [124] is a variant of the Abbott model (2.47) with an enhanced linear dispersion relation. To obtain this model, we first add and subtract to the nondimensional momentum equation the quantity $\mu^2 \tilde{h_0}^2 \alpha_{MS} \bar{q}_{xxt}$, where α_{MS} is a free tuning parameter:

$$\bar{q}_t + \varepsilon\left(\frac{\bar{q}^2}{d}\right)_x + dd_x - \mu^2\left(\frac{\tilde{h_0}^2}{3}\bar{q}_{xxt} + \alpha_{MS}\tilde{h_0}^2\bar{q}_{xxt} - \alpha_{MS}\tilde{h_0}^2\bar{q}_{xxt}\right) = 0. \tag{2.49}$$

From the definition of non-dimensional depth $d = \tilde{h}_0 + \mathcal{O}(\varepsilon)$, we can use eq. (2.49) to find that

$$\bar{q}_t = -\tilde{h}_0 d_x + \mathcal{O}(\varepsilon, \mu^2). \tag{2.50}$$

This term is used in eq. (2.49) to replace the term $\alpha_{MS}\bar{q}_{xxt}$ with $-\alpha_{MS}\tilde{h}_0 d_{xxx}$. The dimensional MS model [124] resulting is:

$$d_t + \bar{q}_x = 0,$$
$$\bar{q}_t + \left(\frac{\bar{q}^2}{d}\right)_x + gdd_x = Bh_0^2 q_{xxt} - \alpha_{MS}gh_0^3 d_{xxx} \tag{2.51}$$

where $B = 1/3 - \alpha_{MS}$. The free parameter α_{MS}, allows to improve the linear dispersion properties. Notice that if we set $\alpha_{MS} = 0$ the MS model reduces exactly to the Abbott one.

As before, we report the model expression in terms of $P = gd$ and flux, given by

$$P_t + g\bar{q}_x = 0,$$
$$\bar{q}_t + \left(\frac{\bar{q}^2}{d}\right)_x + dP_x = Bh_0^2 q_{xxt} - \alpha_{MS}h_0^3 P_{xxx}. \tag{2.52}$$

Within the same asymptotic accuracy, we can replace in the dispersion corrections the reference depth h_0 with the instantaneous water depth $d(x, t)$. This allows to factor the operators

$$\mathcal{L}_B(\cdot) = (1 - Bh_0^2\partial_{xx})(\cdot), \quad \mathcal{B}_\alpha^d(\cdot) = d\partial_x(1 + \alpha_{MS}h_0^2\partial_{xx})(\cdot), \tag{2.53}$$

such that the MS eqs. (2.52) can be written as

$$P_t + g\bar{q}_x = 0,$$
$$\mathcal{L}_B(\bar{q}_t) + \left(\frac{\bar{q}^2}{d}\right)_x + \mathcal{B}_\alpha^d(P) = 0. \tag{2.54}$$

Linear dispersion properties

The linear dispersion properties of a model are often expressed by the phase velocity c that the model describes. The phase velocity of a wave is the rate at which any frequency component of the wave travels in space and it is related to the wave angular frequency ω and the wave number κ:

$$c = \frac{\omega}{\kappa}. \tag{2.55}$$

The phase velocity of a model is computed from the Fourier analysis of the linear version of the equations. In particular, the phase and dissipation of the model are the solution of the algebraic compatibility equations obtained when assuming a solution:

$$d(x,t) = d_0 e^{\nu t + i\kappa x}, \ \bar{u}(x,t) = u_0 e^{\nu t + i\kappa x}, \tag{2.56}$$

where $\nu = \xi + i\omega$ with ξ the dissipation rate and ω the angular frequency (2.55). Note that for the Euler equations the well known Airy theory [112, 49] shows that waves propagate on a static background with depth h_0 with an angular frequency that has a strong nonlinear dependence on the wavenumber :

$$\omega^2_{Airy} = gh_0 k^2 \frac{\tanh(\kappa h_0)}{\kappa h_0} \tag{2.57}$$

NSW model. We start by considering the linearized form of the equations, assuming a static background:

$$\begin{aligned} d_t + h_0 u_x &= 0, \\ u_t + g d_x &= 0. \end{aligned} \tag{2.58}$$

Inserting the signals (2.56), the resulting system reads:

$$\begin{aligned} \nu d_0 + i\kappa h_0 u_0 &= 0, \\ \nu u_0 + ig\kappa d_0 &= 0. \end{aligned} \tag{2.59}$$

Solving the complex eigenvalue problem:

$$\begin{pmatrix} \nu & i\kappa h_0 \\ ig\kappa & \nu \end{pmatrix} \begin{pmatrix} d_0 \\ u_0 \end{pmatrix} = 0, \tag{2.60}$$

we have

$$\xi = 0, \ \omega^2 = \kappa^2 gh_0. \tag{2.61}$$

This result is the well known result that the celerity of hydrostastic shallow water waves is

$$c^2_{NSW} = gh_0. \tag{2.62}$$

Note that the celerity is independent on the wavenumber, which means that all frequencies are transported at the same speed. As a consequence no frequency dispersion is accounted for by the model.

Abbott model. We proceed as before, and consider a linearization around the static state of the system (2.48)

$$\begin{aligned} d_t + h_0 \bar{u}_x &= 0, \\ \bar{u}_t + g d_x - \frac{h_0^2}{3} \bar{u}_{xxt} &= 0. \end{aligned} \tag{2.63}$$

In this case, the matrix associated to the Fourier analysis is

$$\begin{pmatrix} \nu & ih_0\kappa \\ ig\kappa & (1+\phi^2/3)\nu \end{pmatrix}, \tag{2.64}$$

having set $\phi = \kappa h_0$. Solving in terms of ν shows that the Abbot model has the following spectral properties:

$$\xi = 0, \quad \omega^2 = \kappa^2 ch_0 \frac{1}{1+\phi^2/3} \tag{2.65}$$

As for the NSW equations we find no damping, and we can readily evaluate the phase velocity :

$$c_{Abbott}^2 = gh_0 \frac{1}{1+\phi^2/3}. \tag{2.66}$$

As we can see, in this case both the angular frequency and the phase velocity depend on the wave number. The Abbot system is thus able to account for frequency dispersion at leading order. However, the phase has a much simpler expression than the exact one (2.57). We will shortly see how large is the error.

Madsen and Sørensen model. Linearizing the MS eqs. (2.51), we obtain

$$\begin{aligned} d_t + h_0 \bar{u}_x &= 0, \\ \bar{u}_t + gd_x - h_0^2 B \bar{u}_{xxt} + g\alpha_{MS} h_0^2 d_{xxx} &= 0. \end{aligned} \tag{2.67}$$

The matrix associated to the Fourier analysis is now

$$\begin{pmatrix} \nu & ih_0\kappa \\ ig\kappa(1+\alpha_{MS}\phi^2) & (1+B\phi^2)\nu \end{pmatrix} \tag{2.68}$$

Solving in terms of ν shows that the MS model has the following spectral properties:

$$\xi = 0, \quad \omega^2 = \kappa^2 ch_0 \frac{1+\alpha_{MS}\phi^2}{1+B\phi^2} \tag{2.69}$$

Again we find no damping, and we can readily evaluate the phase velocity :

$$c_{MS}^2 = gh_0 \frac{1+\alpha_{MS}\phi^2}{1+B\phi^2}. \tag{2.70}$$

Note that this expression allows to calibrate the result by appropriately choosing α_{MS}. The phase speed of the Abbot model is recovered for $\alpha_{MS} = 0$.

Phase error and window of application The phase speed of the different modes can be compared to the one obtained from (2.57) reading:

$$c_{Airy}^2 = gh_0 \frac{\tanh(\phi)}{\phi} \tag{2.71}$$

The accuracy of each model can be evaluated computing the relative error of the phase velocities on the Airy phase velocity c_{Airy}:

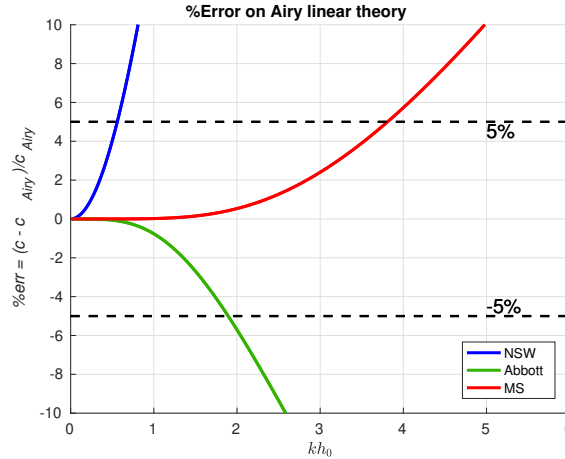$$err = \frac{c - c_{Airy}}{c_{Airy}}. \tag{2.72}$$

FIGURE 2.2 – Phase velocity error wrt the Airy theory. NSW model in blue, Abbott model in black and MS model with $\alpha = -1/15$ in red.

From figure 2.2, the lack of accuracy of the NSW becomes apparent: we see that the error becomes greater than 5% already for waves of $\kappa h_0 \approx 0.6$. The Abbott model improves the description of dispersive waves, w.r.t. the Airy theory, reaching the limit of $err > 5\%$ for wave numbers higher than $\phi > 1.9$, so for deep water or equivalent steep short wave. In case of the MS model, we have the possibility to improve the linear dispersion properties tuning the free parameter α. In particular, the Padé approximation for the dispersion relation can be reached for $\alpha = 1/15$ [124]. The figure 2.2 shows that the error in the phase velocity of the MS model with $\alpha = 1/15$ remains $err < 3\%$ in all the range of wave numbers considered in figure 2.2, pushing the windows of application of the model to $\kappa h_0 > \pi$. This value is known as the limit below the so called deep water region. The range of wave numbers $\kappa h_0 = [0, \pi]$ cover the shallow water and near shore region.

2.2.2 Body domain

We now consider the flow in the region below a fixed or moving body. The corresponding horizontal domain is denoted by Ω_b. Neglecting again the viscous effects, the flow can still be modelled with the Euler equations.

The Euler system is now considered on a domain defined by Ω_b times the vertical region between the body and the seabed (see figure 2.3). Some of the physical quantities involved have however a different behaviour. For example, the water column height d is now only indirectly related to the wave dynamics. For fixed bodies, or bodies in forced motion, the value of d is actually a given value, acting as a constraint. We have in particular that now this value can be defined as (see figure 2.3)

$$d(x, t) = h_0 - D_0 - b(x) + \theta(x) + \zeta(t), \tag{2.73}$$

where D_0 is an initial draft of the body form a reference position, $\theta(x)$ represents the geometrical profile of the body and $\zeta(t)$ the instantaneous draft variation on D_0.

FIGURE 2.3 – 1D setup of the body problem.

The last term measures the amplitude of vertical oscillation of the structure. For simplicity we set now

$$\eta(x,t) = \zeta(t) + \theta(x) \text{ and } h_0 - D_0 = \delta_0. \tag{2.74}$$

We also define the position of the center of gravity of the body as z_{cog}.

Hypothesis 1. *In the view of a unified derivation, we assume that the same scaling used for the outer domain as well as the same dimensionless equations also apply in the body domain.*

In particular, relation (2.74) can be written in dimensionless form as

$$\tilde{d} = \frac{d}{h_0} = \tilde{\delta}_0 + \varepsilon\tilde{\eta} - \tilde{b}(x).$$

with $\tilde{\delta}_0 = 1 - D_0/h_0$.

Under these assumptions, we can still write the Euler equations as in (2.14). However now the domain of definition, as well as the boundary conditions are different. We have in particular:

$$\mu^2\left(\eta_t + \varepsilon u_f \eta_x\right) - w_f = 0 \qquad\qquad \text{at } z = \delta_0 + \varepsilon\eta, \tag{2.75a}$$
$$\Pi = \Pi_b(x,t) \qquad\qquad \text{at } z = \delta_0 + \varepsilon\eta, \tag{2.75b}$$
$$\beta\mu^2 u_s b_x - w_s = 0 \qquad\qquad \text{at } z = b. \tag{2.75c}$$
$$u_z = w_x. \tag{2.75d}$$

where Π_b is the pressure on the body surface, relative to the atmospheric one. Note that here there is a major difference between the free surface domain and the body domain. In the first, the surface pressure is a given constant. Under the body, not only Π_b is not given, but it is a major unknown of the problem.

We derive now the asymptotic depth averaged equations. The asymptotic development of the body model follows the same steps of the free surface presented in section 2.2.1 and we report here only the main differences.

The mass equation for Ω_b is again:

$$d_t + \bar{q}_x = 0, \tag{2.76}$$

which is still an exact equation

As for the free surface domain, the equation that describes the dynamic of the depth averaged horizontal velocity is obtained integrating eq. (2.14b) over the water depth:

$$\int_{\beta b}^{\delta_0 + \varepsilon \eta} \left(u_t + \varepsilon \left(u u_x + \frac{1}{\mu^2} w u_z \right) + p_x \right) dz = 0. \tag{2.77}$$

The integration of u_t, $u u_x$ and $w u_z$ provides the same results found for the free surface domain. However, integrating the pressure, we have:

$$\int_{\beta b}^{\delta_0 + \varepsilon \eta} \Pi_x dz \overset{\text{using eq. (2.17)}}{=} \left(\int_{\beta b}^{\delta_0 + \varepsilon \eta} p \, dz \right)_x - \varepsilon \eta_x \Pi_b + \beta b_x \Pi_s. \tag{2.78}$$

As before, we have defined $\Pi_s = \Pi(z = \beta b)$, is the pressure at the seabed. The depth averaged momentum equation now reads

$$(d\bar{u})_t + \varepsilon(d\bar{u^2})_x + (d\bar{p})_x - \varepsilon \eta_x \Pi_b + \beta b_x \Pi_s = 0. \tag{2.79}$$

We discuss here each term composing eq. (2.79).

Asymptotic velocity profile. The asymptotic profile of the velocities $w(z)$ and $u(z)$ approximated at order $\mathcal{O}(\mu^4)$ are identical eqs. (2.32) and (2.33)

$$u(z) = \bar{u} - \mu^2 \left(\bar{u}_{xx} \left(\frac{(z - b)^2}{2} - \frac{d^2}{6} \right) + \beta \bar{u} b_{xx} \left(\frac{d}{2} - z + \beta b \right) \right) + \mathcal{O}(\mu^4), \tag{2.80}$$

$$w(z) = -\mu^2 \left(\bar{u}(z - \beta b) \right)_x + \mathcal{O}(\mu^4). \tag{2.81}$$

Nonlinear term. As for the horizontal and vertical velocity, the nonlinear terms at precision of $\mathcal{O}(\mu^4)$ is identical for the free surface and body domain

$$\bar{u^2} = \bar{u}^2 + \mathcal{O}(\mu^2) \tag{2.82}$$

Asymptotic pressure profile. Integrating eq. (2.14c) over the interval $[z, \delta_0 + \varepsilon \eta]$ and using the condition (2.75b) , we have

$$\Pi(z) = \Pi_b + (\delta_0 + \varepsilon \eta - z) - \mu^2 \left[\bar{u}_{xt} \left(\frac{d^2}{2} - \frac{(z - \beta b)^2}{2} \right) - \beta \bar{u}_t b_x (\delta_0 + \varepsilon \eta - z) \right]$$
$$- \varepsilon \mu^2 \bar{u} \left[\bar{u}_{xx} \left(\frac{d^2}{2} - \frac{(z - \beta b)^2}{2} \right) - (2\beta \bar{u}_x b_x + \beta \bar{u} b_{xx})(\delta_0 + \varepsilon \eta - z) \right]$$
$$+ \varepsilon \mu^2 \left[\bar{u}_x^2 \left(\frac{d^2}{2} - \frac{(z - \beta b)^2}{2} \right) - \beta \bar{u} \bar{u}_x b_x (\delta_0 + \varepsilon \eta - z) \right] + \mathcal{O}(\varepsilon \mu^4). \tag{2.83}$$

Integrating this equation over the water depth

$$d\overline{\Pi} = d\Pi_b + \frac{d^2}{2} - \mu^2 \left(\bar{u}_{xt} \frac{d^3}{3} - \beta \bar{u}_t b_x \frac{d^2}{2} \right)$$
$$- \varepsilon \mu^2 \bar{u} \left(\bar{u}_{xx} \frac{d^3}{3} - \beta(2\bar{u}_x b_x + \bar{u} b_{xx}) \frac{d^2}{2} \right) \tag{2.84}$$
$$+ \varepsilon \mu^2 \left(\bar{u}_x^2 \frac{d^3}{3} - \beta \bar{u} \bar{u}_x b_x \frac{d^2}{2} \right) + \mathcal{O}(\varepsilon \mu^4).$$

As for the free surface domain, we evaluate the seabed pressure Π_s

$$\Pi(\beta b) = \Pi_s = \Pi_b + d - \mu^2 \left(\bar{u}_{xt} \frac{d^2}{2} - \beta \bar{u}_t b_x d \right) + \mathcal{O}(\mu^4, \varepsilon \mu^2). \tag{2.85}$$

Substituting eqs. (2.80), (2.82) and (2.84) into eq. (2.79), the momentum equation, approximated at order $\mathcal{O}(\mu^4, \varepsilon \mu^2, \varepsilon \beta \mu^2)$

$$(d\bar{u})_t + \varepsilon(d\bar{u}^2)_x + \left(d\Pi_b + \frac{d^2}{2} - \mu^2 \left(\bar{u}_{xt} \frac{d^3}{3} - \beta \bar{u}_t b_x \frac{d^2}{2} \right) \right)_x$$
$$- \varepsilon \eta_x \Pi_b + \beta b_x \Pi_s = 0. \tag{2.86}$$

Developing the derivative $(d\Pi_b)_x$ and from definition of the seabead pressure (2.85), we have more compact expression

$$(d\bar{u})_t + \varepsilon(d\bar{u}^2)_x + d(\Pi_b + d)_x + \beta b_x(\Pi_b + d)$$
$$- \mu^2 \left(\bar{u}_{xt} \frac{d^3}{3} - \beta \bar{u}_t b_x \frac{d^2}{2} \right)_x - \beta \mu^2 b_x \left(\bar{u}_{xt} \frac{d^2}{2} - \beta \bar{u}_t b_x d \right) = 0. \tag{2.87}$$

In the inner domain Ω_b we can prove the following result:

Proposition 1. *Under the standard assumption of the Boussinesq theory of*

$$\mu^4 \ll 1, \quad \varepsilon \approx \mu^2, \quad \beta \approx \mu^2, \tag{2.88}$$

in absence of pitch, roll and yaw, all terms accounting for higher-order dispersive effects in the inner domain are negligible, within the classical Boussinesq truncation of $\mathcal{O}(\mu^4, \varepsilon \mu^2, \beta \mu^2)$.

Proof. Consider the high order term $\mu^2 \left(\bar{u}_{xt} \frac{d^3}{3} \right)_x$ in eq. (2.86) . Proceeding similarly to the free surface domain, within the Boussinesq approximation we can show that

$$\mu^2 \left(\bar{u}_{xt} \frac{d^3}{3} \right)_x = \mu^2 (d\bar{u})_{xxt} + \mathcal{O}(\varepsilon \mu^2) = \mu^2 \bar{q}_{xxt} + \mathcal{O}(\varepsilon \mu^2). \tag{2.89}$$

From the mass eq. (2.76), taking the derivative in space and time, we have the relation:

$$d_{xtt} = -\bar{q}_{xxt}. \tag{2.90}$$

However, in absence of pitch, the acceleration $a = d_{tt}$ is always constant in space and $a_x = 0$, thus also

$$\bar{q}_{xxt} = 0.$$

The assumption of small variation of bathymetry implies that

$$\beta \approx \varepsilon,$$

such that the order of the Boussinesq approximation is $\mathcal{O}(\mu^4, \varepsilon \mu^2, \beta \mu^2)$. The high order terms

$$\beta \mu^2 \left(\bar{u}_t b_x \frac{d^2}{2} \right)_x \approx \mathcal{O}(\beta \mu^2),$$
$$\beta \mu^2 b_x \left(\bar{u}_{xt} \frac{d^2}{2} - \beta \bar{u}_t b_x d \right) \approx \mathcal{O}(\beta \mu^2).$$

thus they can be neglected. $\qquad \square$

As a matter of fact, as for the outer domain, we consider a constant bathymetry $b(x) = b_0$, in which case

$$(b_0)_x = 0, \tag{2.91}$$

which also implies that all the $\beta\mu^2$ terms are identically zero.

Nonlinear shallow water equations

Thanks to proposition 1, we can work in the inner domain with the NSW model, which reads

$$\begin{aligned} d_t + (d\bar{u})_x &= 0, \\ (d\bar{u})_t + \varepsilon(d\bar{u}^2)_x + d(d_x + \Pi_b)_x &= 0. \end{aligned} \tag{2.92}$$

We define now the total pressure P for the inner domain as the sum of the hydrostatic and non-hydrostatic pressures

$$P = gd + \Pi_b \tag{2.93}$$

Using dimensional variables and the definition of total pressure eq. (2.93), the NSW in elevation-flux form for the body domain is:

$$d_t + \bar{q}_x = 0, \tag{2.94a}$$

$$\bar{q}_t + \left(\frac{\bar{q}^2}{d}\right)_x + dP_x = 0. \tag{2.94b}$$

The elevation d is a known parameter of the system and the unknowns in the inner domain are the flux and the total pressure. This can be evaluated from the momentum eq (2.94b). Taking the x derivative of eq. (2.94b)

$$-(dP_x)_x = (\bar{q}_t)_x + \left(\frac{\bar{q}^2}{d}\right)_{xx}. \tag{2.95}$$

Taking the time derivative of the continuity eq. (2.94a), we have a relation between the flux q and the vertical acceleration of the body $d_{tt} = a$

$$a = -(q_x)_t, \tag{2.96}$$

and assuming that all the variables are continuous, we can change the order to the time and space derivatives

$$a = -(q_t)_x. \tag{2.97}$$

Thus, combining the eqs. (2.95) and (2.97), we have a new expression for the inner total pressure

$$-(dP_x)_x = -a + \left(\frac{\bar{q}^2}{d}\right)_{xx}. \tag{2.98}$$

Since the mass equation is true also in the outer domain and d_{tt} is the vertical acceleration of the wave, eq. (2.98) is true also in the outer domain.

The main difference here is that in the free surface domain, the water elevation is a main hydrodynamic unknown, while the vertical position of the body surface may well be a given value. In particular this is exactly the case for fixed body as well as bodies in forced motion. For freely floating bodies one needs to consider Newton's second law of dynamics and compute the force balance to obtain the acceleration. This case is analysed in more detail later.

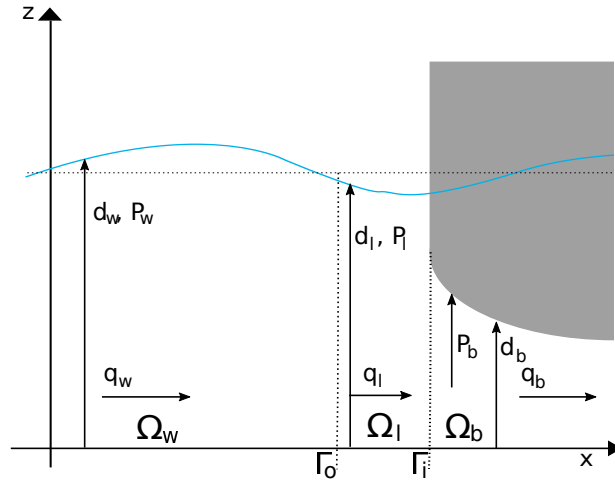### 2.2.3 Conservation issues and coupling condition

FIGURE 2.4 – 1D coupling layer Ω_l setup.

In this section, we address the problem of defining the transmission/coupling condition between the hydrostatic free surface and body domains. The structures considered in this work all have walls that are vertical at the contact point with the fluid. We also focus on fixed and heaving structures, leaving horizontally moving bodies out of the analysis for the moment. The inclusion of rotation (pitch) is also left out.

The coupling between the outer dispersive and inner non-dispersive region is not trivial, and its mathematical analysis is still a research matter [111, 110, 185]. Here we have chosen to avoid going directly from the dispersive free surface to the hydrostatic body domains but adding a thin intermediate hydrostatic free surface region. This splits the issue of domain coupling in two. Across the first interface we couple a dispersive free surface region with a hydrostatic free surface one. Across this interface, all quantities are assumed to be continuous, with possibly continuous normal derivatives. Across the second interface, not only we change the PDE model but add the new variable Π_b. The objective of the next sections is to discuss some physical principles allowing to define the coupling.

As a final remark, we note that the dispersive/non-dispersive coupling here is less problematic than the one often used for wave breaking closure, see e.g. [101] and references therein for a discussion. The reason for things to be easier here is that we are away from the steep wave fronts met in breaking waves.

The coupling condition have been then treated numerically, inserting an intermediate hydrostatic layer between the nonlinear free surface domain (defined as Ω_l) and the body domain Ω_b, as shown in figure 2.4. In Ω_l the free surface dynamic is solved by the NSW eqs. (2.43) and it introduces a simple way evaluate the transition between the non-hydrostatic free surface Boussinesq model to the constrained flow under the body. The idea, following the work of Lannes and collaborators [22] is to exploit the conservation of energy. Work related to the construction of energy conservative fluxes by e.g. Fjordholm et al [73] will be used for the definition of the fluxes.

Conservation relations

To evaluate some conservation relations, let consider the free surface and body domain $\Omega = \Omega_b \cup \Omega_l$ with the interface $\Gamma_i = \Omega_b \cap \Omega_l$ as in figure 2.4. The general NSW system is:

$$\eta_t + q_x = 0,$$
$$q_t + \left(\frac{q^2}{d}\right)_x + d(g\eta + \Pi)_x = 0, \tag{2.99}$$

where Π is the pressure at $z = d$, by definition we have $\Pi = \Pi_{air} = 0$ in Ω_l and $\Pi = \Pi_b$ in Ω_b. The energy conservation statement can be obtained multiplying the components of system (2.99) by the vector $V = [g\eta + \Pi - k, u]$, where we have denoted $k = u^2/2$ the kinetic energy. After simple manipulation, we have

$$\left(g\frac{\eta^2}{2} + dk\right)_t + (q(g\eta + \Pi + k))_x = -\mathcal{W}, \tag{2.100}$$

where $\mathcal{W} = \Pi d_t$ is the power transmitted/absorbed to/from the free surface or body. Setting

$$E = g\frac{\eta^2}{2} + dk, \quad F = q(g\eta + \Pi + k), \tag{2.101}$$

we can write compactly

$$E_t + F_x = -\mathcal{W}. \tag{2.102}$$

In Ω_f both Π and $\mathcal{W}$ are zero and we recover the classical energy conservation for the shallow water equations. In Ω_b, eq. (2.102) represents the energy conservation only for fixed structures [22], while for moving bodies it provides an energy balance. We can now couple the two domains, in particular the eqs. (2.99) and the pressure eq. (2.98). Assuming that

$$\lim_{\substack{x \in \Omega_b \\ x \to \Omega_l}} q = \lim_{\substack{x \in \Omega_l \\ x \to \Omega_b}} q,$$
$$\lim_{\substack{x \in \Omega_b \\ x \to \Omega_l}} F = \lim_{\substack{x \in \Omega_l \\ x \to \Omega_b}} F, \tag{2.103}$$

denoting by $\mathcal{M}$ and $\mathcal{E}$ the total volume of water and the total energy in the domain Ω, we can write

$$\mathcal{M}(t) = \mathcal{M}(0) - \int_0^t \int_{\Omega_b} \mathcal{V} dx dt$$
$$\mathcal{E}(t) = \mathcal{E}(0) - \int_0^t \int_{\Omega_b} \mathcal{W} dx dt \tag{2.104}$$

which state that the initial volume (and thus the mass) and energy are conserved modulo the integral of the volume $\mathcal{V}$ of the body and power pushed in/out by the body.

Note that the definition of energy fluxes F and the relations in (2.103) imply the continuity of the dynamic pressure:

$$\lim_{\substack{x \in \Omega_b \\ x \to \Omega_l}} (g\eta + \Pi + k) = \lim_{\substack{x \in \Omega_l \\ x \to \Omega_b}} (g\eta + \Pi + k) = \lim_{\substack{x \in \Omega_l \\ x \to \Omega_b}} (g\eta + k). \tag{2.105}$$

This relation can be considered as a coupling condition on Γ_i.

Finally, we can deduce the continuity of the nonlinear terms $\mathcal{N}$

$$\mathcal{N} = \left(\frac{q^2}{d} + g\frac{d^2}{2} \right)_x + d\Pi_x, \tag{2.106}$$

as a consequence of the continuity of the fluxes q. From eq. (2.103):

$$\lim_{\substack{x \in \Omega_b \\ x \to \Omega_l}} q_t = \lim_{\substack{x \in \Omega_l \\ x \to \Omega_b}} q_t. \tag{2.107}$$

we can use eq. (2.99) to argue that

$$\lim_{\substack{x \in \Omega_b \\ x \to \Omega_l}} \mathcal{N} = \lim_{\substack{x \in \Omega_l \\ x \to \Omega_b}} \mathcal{N}. \tag{2.108}$$

Summary of coupling conditions

We summarize here the different possibilities in terms of coupling conditions. These are equivalent to a set of jump conditions, which can be used later to define penalty terms in a discrete context.

Mass conservation As seen in the previous section, the conservation of global mass stems from the continuity of the normal component of the flux q. Denoting the outward one dimensional normal directions to the free surface and body domain by $\hat{n}_l$ and $\hat{n}_b$, and by q the flux vector, we can define the jump at the interface as

$$[\![q\hat{n}]\!] := q_b\hat{n}_b + q_l\hat{n}_l. \tag{2.109}$$

Thus, the conservation of total mass is equivalent to

$$[\![q\hat{n}]\!] = 0. \tag{2.110}$$

Energy Conservation As for the total mass, the validity of the total energy balance in (2.104) is a consequence of the continuity of the normal energy flux (2.103). As for the mass, we can define a normal flux jump as

$$[\![F\hat{n}]\!] := F_b\hat{n}_b + F_l\hat{n}_l = (g\eta_b + \Pi + k_b)\,q_b\hat{n}_b + (g\eta_f + k_f)\,q_f\hat{n}_f. \tag{2.111}$$

Conservation of total energy is equivalent to

$$[\![F\hat{n}]\!] = 0. \tag{2.112}$$

Total pressure continuity As already argued, the combination of the mass and energy conservation conditions, implies that the total dynamic pressure $\mathcal{P} = g\eta + \Pi + k$ should be continuous across the interface between the free surface and body domain, or equivalently:

$$[\![\mathcal{P}]\!]_b := \mathcal{P}_f - \mathcal{P}_b = [\![g\eta + \Pi + k]\!]_b = 0. \tag{2.113}$$

Note that for scalar quantities, the above relation also holds as a definition of the jump. Trivially, we have that $[\![u]\!]_b + [\![u]\!]_f = 0$ for any scalar u.

Hydrostatic total pressure continuity   From a physical point of view, one may argue that in the hydrostatic approximation the value of the pressure at the boundaries of the body domain should match the hydrostatic pressure in the free surface region. Simple computations show that this is equivalent to requiring

$$\lim_{\substack{x\in\Omega_b \\ x\to\Omega_f}} \Pi = [\![g\eta]\!]_b. \tag{2.114}$$

The above relation can be readily converted in a continuity condition for the hydrostatic total pressure $P = \Pi + g\eta$ reading:

$$[\![P]\!] = 0. \tag{2.115}$$

Note that the above condition, while based on physical grounds, is not consistent with the conservation of total energy.

Momentum variation continuity   This last condition is a postulate of mass conservation obtained taking the time derivative of (2.109). The resulting jump condition in terms of normal flux and pressure gradient reads

$$[\![\left(\frac{q^2}{d}\right)_x + d(g\eta + \Pi)_x]\!] =$$
$$\left(\left(\frac{q_b^2}{d_b}\hat{n}_b\right)_x + d_b\nabla(g\eta_b + \Pi_b)_x \right)\hat{n}_b + \left(\left(\frac{q_l^2}{d_l}\hat{n}_l\right)_x + d_f(g\eta_l)_x \right)\hat{n}_f = 0. \tag{2.116}$$

Coupling choice

The choice of the coupling conditions between the body and the free surface domain can be done in the interest of preserving different quantities. In general we are going to preserve the total mass of the system using the condition (2.110). The second condition that we impose is the continuity of the hydrostatic pressure eq. (2.115). This is consistent with the exact solution of the hydrostatic equilibrium in definition 2. For this solution, the kinetic energy is null and the outer and inner pressure have to be balanced to keep the body still. Thus, we can speculate that for small variation of the center of gravity of the body around the equilibrium position, the pressure continuity condition remains true. We will also see that the conditions (2.110) and (2.115) are consistent with the fluxes between domains in the variational formulation of the model, resulting from the Galerkin method used to solve the wave-body interaction problem in the domains $\Omega_w \cup \Omega_b$. These coupling will be necessary at the interface between the two domains.

Fluid coupling

The coupling on the interface between the two free surface domain $\Gamma_o = \Omega_w \cap \Omega_l$ imposes the continuity of the wave elevation and of the flux:

$$\begin{aligned} [\![d]\!]_{\Gamma_o} &= d_w + d_l = 0, \\ [\![q]\!]_{\Gamma_o} &= q_w + q_l = 0. \end{aligned} \tag{2.117}$$

Note that multiplying the wave elevation condition by the acceleration of gravity, we can rewrite all the coupling condition in terms of total pressure-flux.

When coupling the two free surface domains, at $(x_{wl}, y_{wl}) \in \Omega_w \cap \Omega_l$, $\Pi(x_{wl}, y_{wl})$ is zero and the condition states that the wave elevation and the flow must be equal through the interface. We also require that normal derivatives of the quantities involved in eq. (2.116) should stay continuous.

2.3   Body dynamics and added mass effects

In the case of a freely floating object, we need to evaluate the acceleration to compute the pressure under the body and the instantaneous position of the body. Using Newton's second law of dynamics, the acceleration can be evaluated from

$$m_b a = -g m_b + \rho_w \int_{\Omega_b} \Pi_b \hat{n}_z dx. \tag{2.118}$$

The non hydrostatic pressure can be obtained from the definition of total pressure $\Pi_b = P - gd$. Consider now the pressure eq. (2.98). We define a linear operator, dependent on the depth d, $\mathcal{K}_d = -\partial_x(d\partial_x(\cdot))$, such that we can rewrite eq. (2.98) as

$$\mathcal{K}_d(P) = -a + \left(\frac{q^2}{d}\right)_{xx}. \tag{2.119}$$

If the operator $\mathcal{K}_d$ admits an inverse operator $\mathcal{K}_d^{-1}$, we can evaluate and expression for the total pressure under the body

$$P = \mathcal{K}_d^{-1}\left(-a + \left(\frac{q^2}{d}\right)_{xx}\right). \tag{2.120}$$

From the definition of total pressure and the force balance eq. (2.118), the acceleration of the body is calculated by

$$m_b a = -g m_b + \rho_w \int_{\Omega_b} \left(\mathcal{K}_d^{-1}\left(-a + \left(\frac{q^2}{d}\right)_{xx}\right) - gd\right) dx, \tag{2.121}$$

collecting the acceleration terms

$$m_b a + \rho_w \int_{\Omega_b} \mathcal{K}_d^{-1}(a) dx = -g m_b + \rho_w \int_{\Omega_b} \left(\mathcal{K}_d^1\left(\left(\frac{q^2}{d}\right)_{xx}\right) - gd\right) dx. \tag{2.122}$$

Notice that, for purely heaving body, the acceleration is not dependent on x and it can be moved outside both the inverse operator $\mathcal{K}_d^{-1}$ and the integral on Ω_b, thus

$$\left(m_b + \rho_w \int_{\Omega_b} \mathcal{K}_d^{-1}(\mathbf{1}) dx\right) a = -g m_b + \rho_w \int_{\Omega_b} \left(\mathcal{K}_d^{-1}\left(\left(\frac{q^2}{d}\right)_{xx}\right) - gd\right) dx. \tag{2.123}$$

We call *added mass* $\mathcal{M}_{add}$ the integral term multiplying the acceleration

$$\mathcal{M}_{add} = \rho_w \int_{\Omega_b} \mathcal{K}_d^{-1}(\mathbf{1}) dx \tag{2.124}$$

since it has the dimension of a mass [111]. An analytic expression for the added mass $\mathcal{M}_{add}$ can be evaluated integrating eq. (2.119) in the interval $(x^-, x) \in \Omega_b$, where x^-

represent the position of left boundary of the domain

$$-P_x(x) = -\frac{x - x^-}{d}a + \mathcal{N}_x,$$ (2.125)

where we collect all the nonlinear expressions in $\mathcal{N}$ as it is not in our immediate interest to solve it. Integrating a second time in (x^-, x)

$$P(x) = \left[\int_{x^-}^x \frac{x - x^-}{d} \, dx \right] a - \mathcal{N}.$$ (2.126)

Substituting in eq. (2.118)

$$m_b a = -g m_b + \rho_w \int_{\Omega_b} \left[\left(\int_{x^-}^x \frac{x - x^-}{d} \, dx \right) a - \mathcal{N} \right] \hat{n}_z dx.$$ (2.127)

Thus we can define the analytical added mass matrix as

$$\mathcal{M}_{add}^{analytical} = -\rho_w \int_{\Omega_b} \left[\int_{x^-}^x \frac{x - x^-}{d} \, dx \right] dx.$$ (2.128)

Moreover, the inverse operator $\mathcal{K}_d^{-1}$ can be expressed by the integral function

$$\mathcal{K}_d^{-1} = \int_{x^-}^x \frac{x - x^-}{d} \, dx.$$ (2.129)

2.4 Model summary

We summarize here the models used to solve the evolution of the free surface and body domain. Since we are always going to use depth averaged variables, from now on we drop the notation $(\bar{\cdot})$ and the depth averaged velocity and flux are indicated as u and q. Moreover, to maintain the notation light, the nonlinear term is denoted by uq, using the fact that $q = du$.

The free surface domain $\Omega_f = \Omega_w \cup \Omega_l$ is solved by

$$P_t + g q_x = 0, \qquad x \in \Omega_l \cup \Omega_w;$$ (2.130a)
$$\mathcal{L}_B q_t + (uq)_x + \mathcal{B}_d^\alpha P = 0,$$ (2.130b)
$$-(\mathcal{B}_d^\alpha P)_x = (\mathcal{L}_B q_t)_x + (uq)_{xx},$$ (2.130c)
$$(\alpha_{MS}, B) = \begin{cases} (1/15, 1/3 + \alpha_{MS}), & x \in \Omega_w, \\ (0, 0), & x \in \Omega_l, \end{cases}$$ (2.130d)

while in the body domain Ω_b we have

$$d_t + q_x = 0,$$ (2.131a)
$$-(dP_x)_x = -a + (uq)_{xx}, \qquad x \in \Omega_b,$$ (2.131b)
$$q_t + (uq)_x + dP_x = 0,$$ (2.131c)

Note that eq. (2.131a) is never going to be solved explicitly and it acts as a constrain for the inner flow. On the other hand, eq. (2.130c) is automatically satisfied by the solution of eqs. (2.130a) and (2.130b). In the inner domain, for freely heaving bodies, we have to calculate the position of the center of body z_{cog}. z_{cog} is obtained from the

Newton's second law of dynamics, in particular:

$$(m_b + \mathcal{M}_{add})\, a = -g m_b + \rho_w \int_{\Omega_b} \left(\mathcal{K}_d^{-1}((uq)_{xx}) - gd \right) dx. \qquad (2.132)$$

where $\mathcal{M}_{add}$ is the added mass, from eq. (2.124).

The exchange of mass and fluxes through the interfaces Γ_i and Γ_o is performed by imposing the continuity of mass, the continuity of the momentum variation and the hydrostatic total pressure presented in section 2.2.3. On the body-coupling layer interface, considering that $\hat{n}_b = -\hat{n}_l$, the coupling reads

$$\left.\begin{aligned}
[\![q]\!]_{\Gamma_i} = 0 &\rightarrow q_b(x_i, t) = q_l(x_i, t), \\
[\![q_t]\!]_{\Gamma_i} = 0 &\rightarrow (q_b(x_i, t))_t = (q_l(x_i, t))_t, \\
[\![P]\!]_{\Gamma_i} = 0 &\rightarrow P_l(x_i, t) = P_b(x_i, t).
\end{aligned}\right\} \quad x_i \in \Gamma_i = \Omega_l \cap \Omega_b. \qquad (2.133)$$

These are a direct consequence of the conservation of mass eq. (2.110) and the wave elevation continuity eq. (2.115). The coupling between the coupling layer and the outer MS domain reads

$$\left.\begin{aligned}
[\![d]\!]_{\Gamma_o} &\rightarrow d_w(x_o, t) = d_l(x_o, t), \\
[\![q]\!]_{\Gamma_o} &\rightarrow q_w(x_o, t) = q_l(x_o, t).
\end{aligned}\right\}, \quad x_o \in \Gamma_o = \Omega_w \cap \Omega_l. \qquad (2.134)$$

The coupling conditions in the outer domain imply also

$$q_w(x_o, t) - q_l(x_o, t) = u_w d_w(x_o, t) - u_l d_l(x_o, t) = 0 \rightarrow [\![u]\!]_{\Gamma_i} = 0, \qquad (2.135)$$

and the momentum variation continuity condition is automatically verified.

The free surface MS model requires some additional coupling condition for the high order terms. These are found defining some first order auxiliary variables

$$\begin{aligned}
G - q_{xt} &= 0, \\
F - N_x &= 0, \\
N - P_x &= 0.
\end{aligned}$$

and requiring their continuity across the interface Γ_o

$$\left.\begin{aligned}
[\![G]\!]_{\Gamma_o} &\rightarrow G_w(x_o, t) = G_l(x_o, t), \\
[\![F]\!]_{\Gamma_o} &\rightarrow F_w(x_o, t) = F_l(x_o, t), \\
[\![N]\!]_{\Gamma_o} &\rightarrow N_w(x_o, t) = N_l(x_o, t).
\end{aligned}\right\}, \quad x_o \in \Gamma_o = \Omega_w \cap \Omega_l. \qquad (2.136)$$

These continuity conditions permit to reconstruct the value of the derivative on the border, transmitting the fluxes from the MS and NSW domains.

Finally, the system is closed adding the far field condition

$$\begin{aligned}
d_w|_{\pm\infty} &= h_0, \\
q_w|_{\pm\infty} &= 0.
\end{aligned} \qquad (2.137)$$

The enforcement of these condition is discussed in the following section 2.5.

2.5 Periodic and solitary wave generation

In this section we briefly discuss the generation of the incoming waves or soliton in the free domain.

2.5.1 Periodic wave generation

Several ways have been proposed to generate waves in a numerical wave tank, from analytical solutions proposed for piston and flap wave makers [45] to adding a source term to the equations [121]. In this work we make use of the relaxation method proposed by Larsen and Darcy [113] to be able to generate and absorb waves. In the relaxation method, the numerical variable $f_{num}(x,t)$ is modified at every timestep of the simulation in a smooth way using a relaxation function $w(x)$: $\Omega_w \rightarrow [0,1]$. Here the variable f can be either the elevation $d(x,t)$ or the flux $q(x,t)$. The value of the relaxed solution is given by

$$f_{relaxed}(x,t) = w(x)f_{num}(x,t) + (1 - w(x))f_{exact}(x,t), \qquad (2.138)$$

where $f_{exact}(x,t)$ is the analytical function. The relaxation function $w(x)$ acts as a damper on the numerical wave motion, absorbing it in the so called *sponge layer*. The term $(1 - w(x))$ operate as a source term, generating the desired waves. This area is defined as *source layer*.
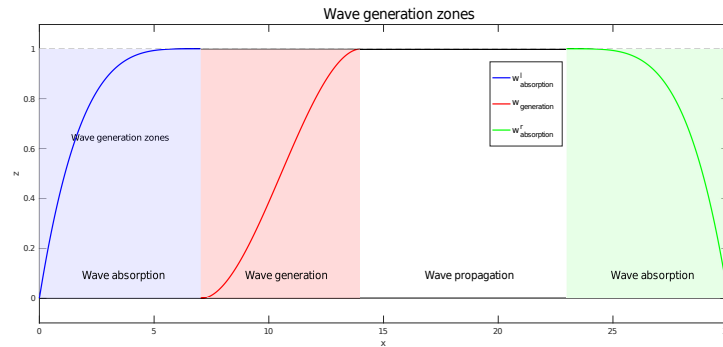

FIGURE 2.5 – Typical setup of sponge and source layer for waves travelling in the positive direction.

In this work we have used two relaxation functions for the absorption and generations of waves, respectively:

$$w^{r,l}_{absorption}(x,p) = 1 - x^p,$$
$$w_{generation}(x) = -2x^3 + 3x^2,$$

Typically, an additional sponge layer with $w(x, \{5, \ldots, 0\})$ is positioned behind the source layer so that it can absorb the possible waves travelling in the opposite direction. The rule of thumb to determine the appropriate length of the relaxation region is that is should span 1 to 2 wave lengths of the primary wave [56].

Finally the wave should be generated increasing gradually the amplitude to the final one. We introduce a time dependent parameter $\sigma(t) : \mathbb{R}^+ \rightarrow [0,1]$

$$\sigma(t) = \begin{cases} t/T_{ramp}, & t \leq T_{ramp}, \\ 1, & t > T_{ramp}. \end{cases}$$

where T_{ramp} is a ramp up period. The wave generation equation results:

$$f_{relaxed}(x,t) = w(x)f_{num}(x,t) + \sigma(t)(1 - w(x))f_{exact}(x,t). \qquad (2.139)$$

The drawback of this method is that it might occupy a large part of the computational domain. However it has been chosen since it is a procedure that is simple and flexible to use.

Far field

On the external boundaries of the outer domains, it is common to impose either periodic conditions or the absorption of the wave. In the first case, the coupling condition at the two extremes of Ω_w are the continuity of elevation and flux as in eq. (2.117). However, thanks to the wave absorption method introduced, we impose the far field conditions (2.137):

$$\begin{aligned} d_w|_{\pm\infty} &= h_0, \\ q_w|_{\pm\infty} &= 0. \end{aligned} \qquad (2.140)$$

This is the method of choice since imposing the absorption of wave at the domain's ends avoids the interactions between the generated waves and the waves exiting the domain. Moreover it represents a more realistic physical water flume.
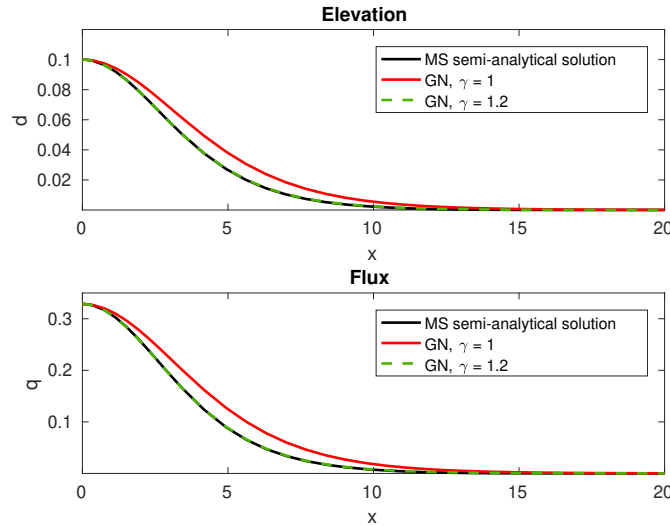
2.5.2 Soliton solution

FIGURE 2.6 – Solitary wave profile of amplitude $A = 0.1$ of the semi-analytical MS solution, exact GN ($\gamma = 1$) and modified GN with $\gamma = 1.2$.

The interaction of a solitary wave and a fixed pontoon is one of the benchmarks of this work. For the generation of the solitary wave, there are two possible paths.

We know that for a wave celerity $c > c_{NSW}$, the MS equations admit a unique solitary wave solution of the form $(d(x - ct), q(x - ct))$ [18]. However, an analytical solution of the soliton is not available but a semi-analytical form can be numerically calculated [153].

Alternatively, we can use the Green-Naghdi (GN) solitary wave solution [19]. The solitary wave of amplitude A is defined as:

$$\begin{cases} d(x,t) = h_0 + A \operatorname{sech}^2(k(x - x_0 - ct)), \\ u(x,t) = c\left(1 - \frac{h_0}{d(x,t)}\right), \\ q(x,t) = d(x,t)u(x,t). \\ k = \gamma \frac{\sqrt{2A}}{2h_0\sqrt{h_0 + A}}, \quad c = \sqrt{g(A + h_0)}. \end{cases} \tag{2.141}$$

where γ is a free parameter that permits to control the steepness of the solitary wave and x_0 the center of the wave's crest. We have the exact solution for $\gamma = 1$. However, eq. (2.141) is not exact for the MS model since it has different dispersion characteristics. This will result in a dispersion trail behind the solitary wave. Thanks to the steepness parameter γ, we can tune the initial GN wave's profile to match the semi-analytical MS solution as we can see in figure 2.6, resulting in a negligible initial error.

2.6   Some analytical solutions

We outline here the analytical and semi-analytical solutions for a truncated structure with vertical walls, partially immersed in water.

2.6.1   Hydrostatic equilibrium

Definition 2. *We define as hydrostatic equilibrium, the state*

$$(\bar{d}_{w,l}, \bar{d}_b, \bar{P}, \bar{q}, \bar{u}, \bar{a}) = (h_0, d_b, gh_0, 0, 0, 0), \tag{2.142}$$

with d_b and h_0 as the equilibrium depths under the body and in the free surface regions, linked by the hydrostatic equilibrium relation

$$\frac{m_b}{\rho_w} = \int_{\Omega_b} (h_0 - \bar{d}_b)dx. \tag{2.143}$$

Note that the the equilibrium, the variable $\bar{d}_b$ depends only on the space.

From the hydrostatic equilibrium relation eq. (2.143) we have an expression for the equilibrium position of the center of gravity z_{cog}. Substituting the definition of $\bar{d}_b(x)$, eq. (2.73),

$$\frac{m_b}{\rho_w} = \int_{\Omega_b} (h_0 - D_0 + \theta(x) + \zeta_{eq})dx, \tag{2.144}$$

Solving the equation for ζ_{eq}

$$\zeta_{eq} = \frac{1}{\rho_w |\Omega_b|}\left(\rho_w \int_{\Omega_b} (D_0 - \theta(x)) - m_b\right), \tag{2.145}$$

with $|\Omega_b| = \int_{\Omega_b} 1dx$ the area of Ω_b. But ζ_{eq} is the variation from the equilibrium position in time, thus it must be equal to zero and eq. (2.145) is the Archimedes' principle, at the equilibrium the mass of the body must be balance by the mass of water moved by the body. If we consider the reference level of D_0 as crossing the center of gravity of the body $D_0 = h_0 - z_{cog}$, the position of center of the gravity of

the body at the equilibrium is determined by

$$z_{cog} = \frac{1}{\rho_w |\Omega_b|} \left(\rho_w \int_{\Omega_b} (h_0 - \theta(x)) - m_b \right). \tag{2.146}$$

2.6.2 Forced motion

The water flow does not affect the motion of the body with a prescribed motion, however it is affected by the body's presence. The effects on the water flow are taken into account by the inner pressure in eq. (2.98). In the prescribed motion case, the position, velocity and acceleration $(d_b, v, a) = (d_b, \partial_t d_b, \partial_{tt} d_b)$ of the body are imposed by the user: in case the acceleration and velocity are imposed null, $(v, a) = (0, 0)$, the body is still and the body is defined as the pontoon; when the velocity and acceleration are imposed different from zero, for example $v = \sin(\omega t)$, we have the generation of waves by the motion of the body.

The prescribed (or forced) motion test implies that the body moves vertically with a velocity and acceleration imposed by the user. The body is thus used like a wave generator. The hydrostatic case of an axisymmetric body in forced motion admits an exact solution for the evolution of the contact point between free surface and body for a structure, calculated first by Lannes in [111]. The time dependent analytical solution of the water elevation at the contact points $x_{\pm}$ is

$$d_c(t, x_{\pm}) = \left(\tau_0 \left(\frac{x_+ - x_-}{4\sqrt{g}} v_G \right) \right)^2, \tag{2.147}$$

where $v_G = d_t$ is the given velocity of the center of gravity of the body. The function $\tau_0(r)$ can be obtained by

$$\tau_0(r) = \frac{1}{3} \left(\sqrt{h_0} + C(r) + \frac{h_0}{C(r)} \right). \tag{2.148}$$

$C(r)$ is a function dependent on the parameter $r_0 = \frac{4}{27} h_0^{3/2}$ that reads

$$C(r) = \frac{3}{2} \left(r_0 - 4r + \sqrt{r(r - r_0)} \right)^{1/3}. \tag{2.149}$$

2.6.3 Hydrostatic decay test

The motion of the body in the hydrostatic decay test is evaluated by Newton's second law of dynamics:

$$m_b a = F_h - g m_b, \tag{2.150}$$

where the hydrodynamic force F_h is evaluated integrating the hydrodynamic pressure Π_b applied by the fluid on the bottom of the body

$$F_h = \rho_w \int_{\Omega_b} \Pi_b \hat{n} dx. \tag{2.151}$$

For the decay test, the body is released from an initial position different from the equilibrium position and left to return to the equilibrium position. Thanks to Lannes [111], for the decay motion test in the hydrostatic case, we have a semi-analytical solution for the position of the center of gravity of a body δ_G. The position of the

center of gravity is calculated solving the ordinary differential equation (ODE):

$$\begin{cases} (m_b + m_{add})\ddot{\delta}_G = -c\delta_G - \nu(\dot{\delta}_G) + \beta(\delta_G)(\dot{\delta}_G)^2 \\ (\delta_G, \dot{\delta}_G)(t=0) = (\delta_G^0, 0). \end{cases} \tag{2.152}$$

with the parameters $\nu(\dot{\delta}_G)$ and $\beta(\delta_G)$ and the stiffness coefficient c defined as:

$$\nu(\dot{\delta}_G) = \rho_w g(x_+ - x_-)\left[h_0 - \left(\tau_0\left(\frac{x_+ - x_-}{4\sqrt{g}}\dot{\delta}_G\right)\right)^2\right],$$

$$\beta(\delta_G) = \rho_w \int_{x_-}^{x_+} \frac{x - x_0}{h_w} \partial_x \left(\frac{(x - x_0)^2}{h_w}\right) dx, \tag{2.153}$$

$$c = \rho_w g(x_+ - x_-).$$

with $h_w(t) = d_b + \delta_G(t)$ the position of the wetted surface, d_b the geometry of the bottom of the body at rest and $\zeta_{e,\pm} = \zeta_e(t, x_\pm) = d_b(t, x_\pm) - h_0$. The added mass term m_{add} is evaluated by:

$$m_{add} = \alpha \rho_w Var(x) \quad \alpha = \int_{x_-}^{x_+} \frac{1}{h_w} dx. \tag{2.154}$$

The variance operator $Var(f)$ is defined as

$$Var(f) = \langle f^2 \rangle - \langle f \rangle^2,$$

$$\langle f \rangle = \frac{1}{\int_{x_-}^{x_+} \frac{1}{h_w}} \int_{x_-}^{x_+} \frac{f}{h_w} dx. \tag{2.155}$$

Solving the ODE term permits to track the position of the body in time and the semi-analytical solution can be used to validate our model. Note that in the decay motion test, we do not consider any incoming wave and the only forces applied to the body are the Archimedes' force and gravity force resulting in a dampening force on the movement of the body.

2.6.4 Manufactured solution

As a general method to construct benchmarking solutions for the models we have used the well known method of manufactured solutions (MMS). The MMS consists in building an analytical solution for the mathematical models. The solutions found in this way are not a priori physically relevant, but they permit to obtain some benchmark to verify the accuracy of the simulation. The MMS is straightforward to apply. Consider a system of differential equations, in general it can be written as

$$\mathsf{D}(f) = 0,$$

where the operator D is some kind of differentiating operator. As we do not have an exact expression for the solution f, we impose a sufficiently differentiable known function $\hat{f}$, called the manufactured solution, as solution of the model in space and time. The function $\hat{f}$ will not necessarily solve exactly the governing model, and some residuals $r(\hat{f}) \neq 0$ results from $\mathsf{D}(\hat{f})$. This residuals are "manufactured" as source term to the governing equation, such that the manufactured solution satisfies the system exactly

$$\mathsf{D}(\hat{f}) = r(\hat{f}),$$

and it can be used to verify the simulations. While the solution found is artificial and does not need to be physically meaningful [155], a manufactured solution that expresses some physical characteristic of the model helps not only in the verification of the code but it can also suggest the behaviour and the performances of original system [156, 157, 164].

To verify our models, we have chosen a function

$$\hat{f}(v) = cos(\xi), \text{ with } \xi = x + ct \tag{2.156}$$

where c is a free parameter that represent the celerity of the wave. For the free surface models eqs. (2.43), (2.48) and (2.52), the manufactured variables of the models are all put in relation to the function $\hat{f}$ as

$$
\begin{aligned}
d^m(x,t) &= \hat{f}(\xi) + h_0, \\
P^m(x,t) &= gd^m = g(\hat{f}(\xi) + h_0) \\
u^m(x,t) &= c\hat{f}(\xi), \\
q^m(x,t) &= d^m u^m.
\end{aligned}
\tag{2.157}
$$

The manufactured solution is evaluated also in the body domain for a fixed truncated body and reads

$$
\begin{aligned}
d^m(x,t) &= d_b, \\
P^m(x,t) &= g(\hat{f}(\xi) + h_0) \\
u^m(x,t) &= c\hat{f}(\xi), \\
q^m(x,t) &= \hat{f}(\xi)u^m, \\
a(t) &= 0,
\end{aligned}
\tag{2.158}
$$

where d_b represent the geometry of the body and it is known. The MMS approach is used on meshes that are systematically refined or higher in polynomial order, to test the convergence in space of the method. The behaviour of the error is examined against the theoretical rate of convergence peculiar of the space discretization method.

Chapter 3

1D numerical discretization

Sommaire

3.1 Introduction

In this chapter, we introduce the spectral/*hp* element method (SEM) to solve spatially the wave-body interaction problem and the backward differentiation formulas (BDF) to integrate the system in time. The SEM is a numerical method closely related to the finite element method (FEM). FEM and SEM are numerical methods for solving ordinary and partially differential equations that otherwise would be impossible to solve analytically. The idea at the origin of the methods is to split the solution domain into a partition (mesh) made of a number of smaller sub-domains (or elements). In the subdomains, using a finite set of approximating functions (basis functions), the differential equations and initial value problems are solved using their variational formulation. In this way, the solution is evaluated in each element of the mesh, that can be a priori of any shape and permits to handle complex geometries.

On the set of elements, we can define some global basis functions patching together the local ones. These functions have support at most on neighbour elements and allow to move from a local solution to the global one. The local basis function are based on polynomials and their order affects the accuracy of the method. In the classical FEM, linear polynomials are employed.the convergence in FEM is achieved by refining the domain partition, increasing the number of elements and reducing the size of each element $h \rightarrow 0$, where h is the element size. This kind of convergence is commonly known as *h-type convergence*. On the other hand, global

spectral method increases the polynomial order $p \to \infty$ to obtain convergence, in what is called *p-type convergence*, while keeping the number of elements fixed. For sufficiently smooth problems, this implies exponential convergence, which means that doubling the polynomial order the error decrease faster than algebraic (fixed) order of convergence rate.

The spectral/*hp* element methods combines the two strategies of convergence, using basis functions are piece-wise continuous arbitrary polynomial of high order across each element. The advantages spectral/*hp* element methods include the exponential convergence and a great flexibility in handling complex geometry. These were first proposed in [12, 14], they were formalized by Patera in [145] where the FEM and the global spectral element method are mixed together. In the methods proposed, the high order spectral expansion is applied to each element and the convergence can be achieved both in *h*-type fixing the polynomial order and in *p*-type, raising the polynomial order. Note that neither the element size nor the polynomial order have to be uniform over the domain, but in principle they can vary according to the physics or geometry of the problem.

The main advantages of spectral element methods over FEM is their precision and efficiency. Although for each element the resolution is more computationally costly, with smooth problems, SEM permit the use of less elements to discretize the whole domain and have high accuracy. This results in more compact and smaller matrices that have to be stored and computed, thus minimizing the occupation of memory for large scale simulations. Moreover, it is also suited for long-time integration problems. As the PDEs are solved with high accuracy in space with few elements, the discretization error propagates much less over long simulations. As a result, high order SEMs are more cost-effective compared to low order, linear schemes [108].

The coupling between the free surface domains and the body domain is formulated using a discontinuous Galerkin finite element method (DG-FEM), following the framework of [60]. With this approach, we are going to consider each domain as a single element and apply a linear polynomials on it to discretize the functions. This permits to have a direct way to weakly impose the coupling terms on the interfaces between the domain in terms of exchanged fluxes.

Regarding the time discretization, we have used the extrapolated backward differentiation formula of the third order (eBDF3), because of the low storage requirements and its efficiency. Only the value of the variables at the previous three timesteps are needed to evaluate the solution at the new timestep $n + 1$. Moreover it has the same efficiency of the one order Euler method, since the new solution is evaluated by a single iteration, without any sub-iterations.

This chapter presents the basic derivation of the SEM in one dimension in section 3.2. Section 3.3 presents the derivation of the spatially discrete model for both the outer domain and the inner one. In section 3.4 the time discretization method is presented and applied to the model. Finally we discuss the discretization of the acceleration and the added mass M_{add} in section 3.5.

3.2 1D SEM

In this section we delineate the fundamental steps to implement a SEM method: we will discuss about the choice of the basis functions in terms of polynomial expansion and we will present the matrix formulation used to evaluate integrals and derivatives. We are going to present the SEM in general terms, so for now we are

dropping the distinction between inner and outer domain, to retrieve it once we will be talking of solving the wave-body interaction.
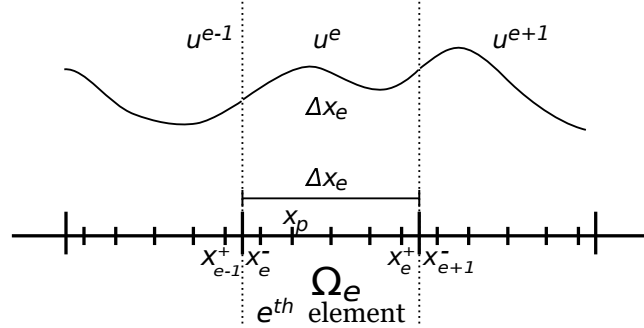
3.2.1 Basis function

FIGURE 3.1 – Sketch and notation for a one dimensional mesh with a local sixth order ($P = 6$), x_p represents the nodes internal to the element Ω_e.

Let consider a computational domain Ω and its partition in N_e number of finite elements Ω_e (cfr. figure 3.1). For each element Ω_e, we define the characteristic length $\Delta x_e = x_e^+ - x_e^-$ and the boundary on x_e^+ and x_e^- as $\Gamma_e = \partial\Omega_e$. The polynomial basis function in the element are defined in the following functional space

$$\Phi = \left\{ \varphi \in L^2(\Omega) : \varphi|_{\Omega_e} \in \mathbb{P}^p(\Omega_e), \forall \Omega_e \in \Omega \right\}, \tag{3.1}$$

where $\mathbb{P}^P(\Omega_e)$ is the space of polynomial of at most degree p in the element Ω_e. This definition enforce the continuity $\mathcal{C}^0$ of the polynomials in the computational domain Ω in the spectral elements method. The choice of a particular set of polynomials, that includes the boundary $\partial\Omega_e$, permits to ensure the continuity of the polynomials.

We introduce here two families of polynomial expansions that are commonly used in the SEM.

Jacobi polynomials   The Jacobi polynomials are a family of polynomials defined in the region $x \in [-1, 1]$. They are generally indicated as $P_n^{(\alpha,\beta)}(x)$, where n represents the polynomial order and $(\alpha, \beta) > -1$ are free parameters. The Jacobi polynomials include the Legendre polynomials, with $\alpha = \beta = 0$, and the Chebyshev polynomials, $\alpha = \beta = -1/2$. The construction of the Jacobi polynomials is done through a recursive relationship

$$\begin{aligned}
P_0^{(\alpha,\beta)}(x) &= 1, \\
P_1^{(\alpha,\beta)}(x) &= \frac{1}{2}(\alpha - \beta + (\alpha + \beta + 2)x), \\
P_n^{(\alpha,\beta)}(x) &= \frac{1}{a_n^1}\left((a_n^2 + a_n^3)P_n^{(\alpha,\beta)}(x) - a_n^4 P_{n-1}^{(\alpha,\beta)}(x) \right),
\end{aligned} \tag{3.2}$$

where $a_n^{(1,2,3,4)}$ are defined as

$$
\begin{aligned}
a_n^1 &= 2(n+1)(n+\alpha+\beta+1)(2n+\alpha+\beta), \\
a_n^2 &= (2n+\alpha+\beta+1)(\alpha^2-\beta^2), \\
a_n^3 &= (2n+\alpha+\beta)(2n+\alpha+\beta+1)(2n+\alpha+\beta+2), \\
a_n^4 &= 2(n+\alpha)(n+\beta)(2n+\alpha+\beta+2).
\end{aligned}
$$

The Jacobi polynomials are orthogonal when integrated w.r.t. $(1-x)^\alpha (1+x)^\beta$: for two polynomial orders n, i such that $i < n$:

$$
\int_{-1}^{1} (1-x)^\alpha (1+x)^\beta P_n^{(\alpha,\beta)}(x) P_i^{(\alpha,\beta)}(x) dx = C_n^{(\alpha,\beta)} \delta_{ni}, \tag{3.3}
$$

where δ_{ni} is the Kroneker delta and $C_n^{(\alpha,\beta)}$

$$
C_n^{(\alpha,\beta)} = \frac{2^{1+\alpha+\beta}}{2n+\alpha+\beta+1} \frac{\Gamma(n+\alpha+1)\Gamma(n+\beta+1)}{n!\Gamma(n+\alpha+\beta+1)}.
$$

Lagrange polynomials   The *Pth* degree Lagrange polynomial $h_p(x)$ on a set of points $x_p \in [-1,1]$ with $0 < p < P-1$ is obtained by the equation:

$$
h_p(x) = \frac{\Pi_{i=0,i\neq p}^{P-1}(x-x_i)}{\Pi_{i=0,i\neq p}^{P-1}(x_p-x_i)}. \tag{3.4}
$$

Moreover, the Lagrange polynomial $h_p(x)$ is the unique polynomial of order P which has unit value at x_p and is zero at $x_i, i \neq p$:

$$
h_p(x_i) = \delta_{pi}. \tag{3.5}
$$

The Lagrange polynomials are called *Cardinal functions* as the satisfy the *Cardinal property* (3.5).

The Lagrange polynomial h_p are very well suited as interpolation basis functions. Defining the interpolant operator $\mathcal{I}_p$ of order $P+1$, that interpolates a function at the nodes x_p:

$$
\mathcal{I}_p u(x) = \sum_{p=0}^{P} \hat{u} h_p(x).
$$

The cardinal property implies that the coefficient $\hat{u}$ can be directly determined in terms of the interpolant at the points x_p

$$
\mathcal{I}_p u(x_q) = \sum_{p=0}^{P} \hat{u}_p h_p(x_q) = \sum_{p=0}^{P} \hat{u}_p \delta_{pq} = \hat{u}_q.
$$

The weights $\hat{u}$ of the interpolation with the Lagrange polynomials are the values of the interpolant at the points x_p. This implies that $\mathcal{I}u(x_p) = u(x_p)$ and

$$
\mathcal{I}u(x) = \sum_{p=0}^{P} u(x_p) h_p(x). \tag{3.6}
$$

Note that the interpolation is exact for polynomial function of order $Q \leq P$. Having defined the interpolation in eq. (3.6), we can also define the differentiation of a function $u(x)$, with $x \in [-1, 1]$:

$$\frac{d}{dx}\mathcal{I}u(x) = \frac{d}{dx}\left(\sum_{p=0}^{P} u(x_p)h_p(x)\right) = \sum_{p=0}^{P} u(x_p)\frac{d}{dx}h_p(x). \tag{3.7}$$

SEM global basis function

A function $u(x)$ can be represented by the combination of piece-wise continuous polynomial functions as

$$u(x) \cong \hat{u}(x) = \sum_{j=1}^{M} \hat{u}_j \varphi_j(x), \quad x \in \Omega, \tag{3.8}$$

where $\varphi_j(x)$ is a global basis function that satisfy the Cardinal property (3.5). Each global function $\varphi_j(x)$ is defined on the global domain Ω but it has only local support over the elements that node x_j belongs to. In one space dimension, the function $\varphi_j(x)$ is different from zero at most on two adjacent elements.

It is possible to represent each global basis function $\varphi_j(x)$ in term of local basis function $\varphi_j^{(e)}(x)$ defined on each element. The local basis functions can be for example the Lagrange polynomials. We define $\varphi_j(x)$ as

$$\varphi_j(x) = \bigoplus_{e=1}^{M} \sum_{i=1}^{P} \varphi_i^{(e)}(x_i)\varphi_i^{(e)}(x). \tag{3.9}$$

The operator $\bigoplus$ represent the summation of disjoint intervals, so that global domain is reconstructed from the single elements.

In each element Ω_e a function is expressed by a polynomial of order P, defined over $P + 1$ *nodes* (or *nodal points*). Of these nodes, $P - 1$ are internal to the element. The remaining two are placed on on the boundary to ensure at least the $\mathcal{C}^0$ continuity for the global basis functions $\varphi_j(x)$, $j = 1, \dots, M$. We define as x_p the $P + 1$ nodes. It is convenient to map the nodes $x_p \in \Omega_e$ to the standard element defined in $r \in \Omega_{st} = [-1, 1]$ as:

$$x(r) = \frac{1}{2}(x_e^+ + x_e^-) + \frac{1}{2}(x_e^+ - x_e^-)r, \quad x(r) \in \Omega_e = [x_e^-, x_e^+],$$

such that a single operator can be stored and reused for all the elements of the domain with minimal operational cost.

The choice of the nodal points plays an important role in the conditioning of the matrices of the interpolations. The natural choice would be to use equispaced nodes, however the optimal choice is the Gauss-Lobatto-Legendre (GLL) points. In fact, comparing the two sets, if for low order the Lagrange polynomial look very similar (cfr. the $P = 5$ equispaced and GLL polynomials in figures 3.2(a) and 3.3(a)), when $P \to +\infty$ the equispaced Lagrange polynomials presents Runge oscillations close to the domain boundaries (figures 3.2(b), 3.2(c) and 3.2(d)) leading to bad conditioned matrices. On the other hand, the Lagrange polynomials based on GLL nodes do not present that problem, as seen in figure 3.3. The distribution of the GLL nodes of order P is calculated as the zeros of the Legendre polynomial of the same order $P_p^{0,0}(r) = 0$.
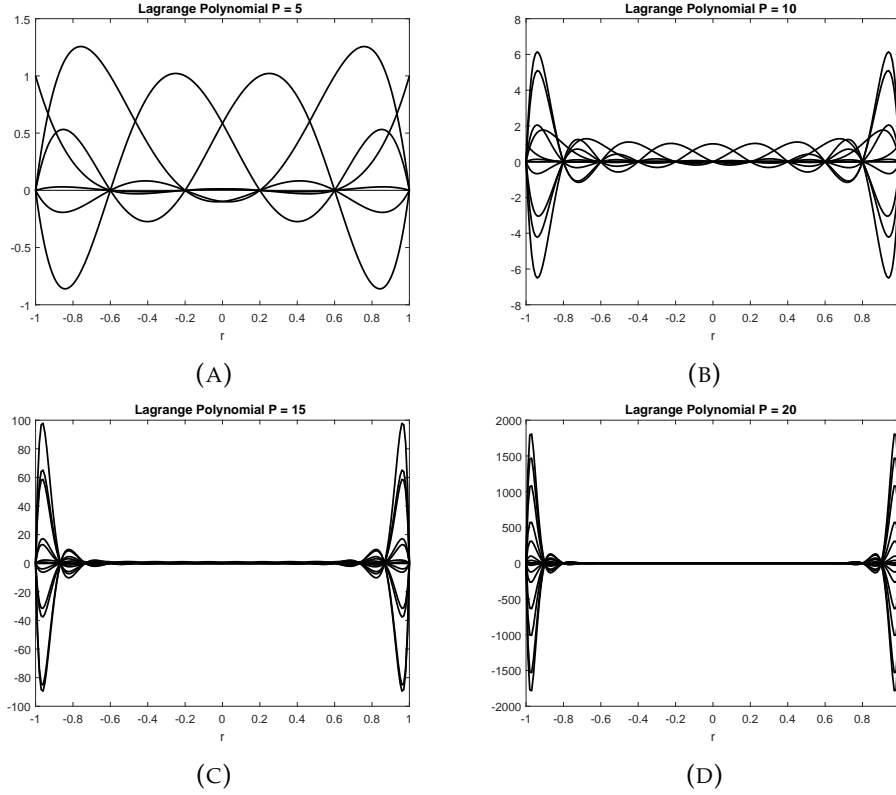
FIGURE 3.2 – Lagrange polynomial through equispaced nodes on the reference domain Ω_{st} for polynomial orders $P = 5, 10, 15$ and 20.

3.2.2   Interpolation

The SEM global basis functions φ_j can be used for interpolation. Of a function $u(x)$ defined in $x \in \Omega$, the interpolated function $u_I(x)$ can be evaluated as

$$u_I(x) = \sum_{j=1}^{M} u(x_j)\varphi_j(x), \quad x \in \Omega, \tag{3.10}$$

on a mesh of x_j nodes with $j = 1, \dots, M$. The global basis functions $\varphi_j(x)$ are piecewise $\mathcal{C}^0$ arbitrary order polynomial constructed as in eq. (3.9). With the right choice of basis functions, i.e. Lagrange basis functions, from the Cardinal property, we have that

$$u_I(x_j) = u(x_j), \quad j = 1, \dots, M, \tag{3.11}$$

such that the interpolating function interpolates $u(x)$ exactly at the mesh nodes. Expressing the value of $u(x_j)$ by means of local basis functions, the interpolated function is

$$u_I(x) = \sum_{j=1}^{M} \bigoplus_{e=1}^{N} \left(\sum_{i=1}^{P} u(x_j)\varphi_i^{(e)}(x_j) \right) \varphi_j(x), \quad x \in \Omega. \tag{3.12}$$

We would like to represent the global gradient of a function $\partial_x u(x)$ in a similar fashion as the local differentiation in eq. (3.7), namely

$$\partial_x u(x) \cong \sum_{j=1}^{M} u(x_j)\partial_x \varphi_j(x), \quad x \in \Omega. \tag{3.13}$$
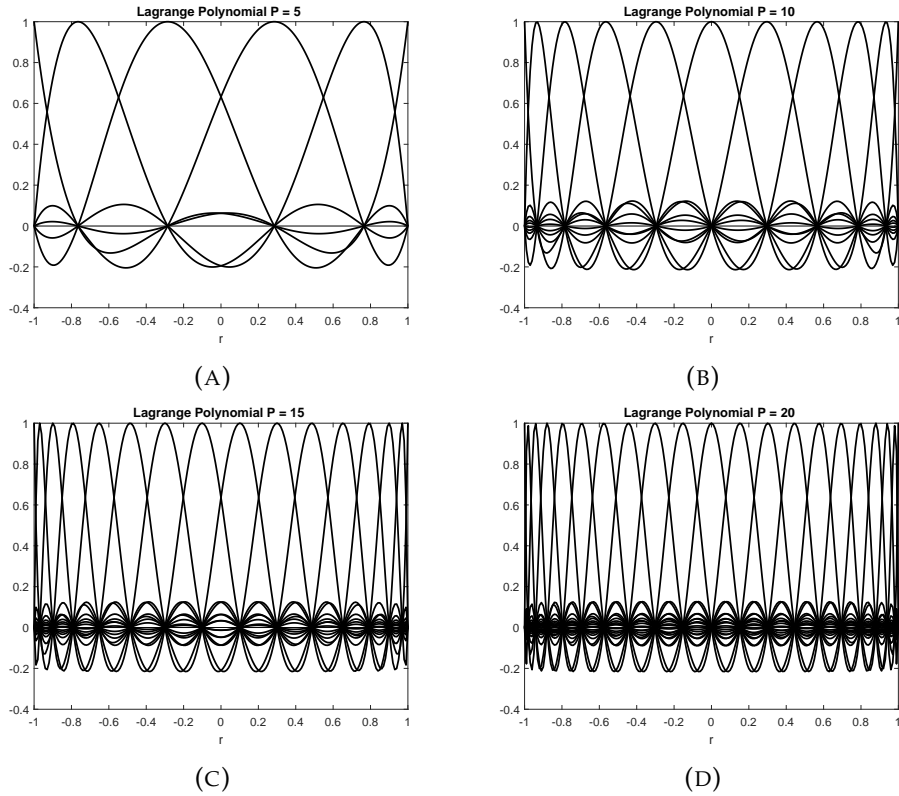
FIGURE 3.3 – Lagrange polynomial through Gauss-Lobatto-Legendre nodes on the reference domain Ω_{st} for polynomial orders $P = 5, 10, 15$ and 20.

However, the gradient of the $\mathcal{C}^0$ continuous global functions will not be continuous across the interfaces between elements in the classical sense. The global continuity of the derivative is guaranteed by a gradient recovery technique [90, 167]. In the framework of the SEM, we have employed the procedure described in [55]. We express the derivative function through a global approximation defining the auxiliary function $g(x) = \partial_x u(x)$, such that

$$\partial_x u(x) \cong g_I(x) = \sum_{j=1}^{M} g(x_j) \varphi_j(x). \tag{3.14}$$

But the $g(x_j)$ can be represented using the direct sum of local basis functions in the elements Ω_e

$$g_I(x) = \sum_{j=1}^{M} \bigoplus_{e=1}^{N} \left(\sum_{i=1}^{P} g(x_j) \varphi_i(x_j) \right) \varphi_j(x). \tag{3.15}$$

In each element, the basis function are continuous, so the following relation is valid

$$\sum_{i=1}^{P} g(x_j) \varphi_i(x_j) = \sum_{i=1}^{P} u(x_j) \partial_x \varphi_i^{(e)}(x_j). \tag{3.16}$$

Thus, the differentiation of the function $u(x)$ is interpolated by

$$\partial_x u_I(x) = \sum_{j=1}^{M} \bigoplus_{e=1}^{N} \left(\sum_{i=1}^{P} u(x_j) \partial_x \varphi_i^{(e)}(x_j) \right) \varphi_j(x). \tag{3.17}$$

Error Boundary

Consider the interpolated function $u_I(x) = \mathcal{I}u(x)$. It has been shown in [53] the interpolation error $err(x) = u_I(x) - u(x)$ for sufficiently differentiable function is bounded. In particular, for $u(x) \in \mathcal{C}^{P+1}$, in each N_e elements $i = 1, 2, \ldots, N_e$, the error is

$$\max_{x \in \Omega_{e_i}}(err(x)) \leq C_i h_i^{P+1} \max_{x \in \Omega_{e_i}}(\partial_x^{P+1}u(x)), \tag{3.18}$$

where ∂_x^{P+1} being the $(P+1)$'th derivative operator. The constant C_i depends on the location of the nodes and is optimal for nodes that are clustered around the boundary nodes, such as the GLL nodes. From the local error bounds (3.18) we can derive a global error bounds on the domain Ω:

$$\max_{x \in \Omega}(err(x)) \leq C h^{P+1} \max_{x \in \Omega}(\partial_x^{P+1}u(x)). \tag{3.19}$$

where the largest element length and constant are defined as

$$h = \max_i h_i, \quad C = \max_i C_i.$$

We want to point here that the finite element method can be considered as a particular case of spectral element methods, in which the polynomial basis function are linear ($P = 1$). The global error [53] is:

$$\max_{x \in \Omega}(err(x)) \leq \frac{1}{8} h^2 \max_{x \in \Omega}(\partial_x^2 u(x)). \tag{3.20}$$

Simply comparing the error's boundaries (3.19) and (3.20), with the same mesh, we see that high order SEM can reach an higher accuracy that the FEM.

3.2.3 Discrete formulation

Element matrices

We illustrate the SEM in general by considering the transport equation

$$\dot{f} + c f_x = 0, \tag{3.21}$$

defined in the domain Ω. The domain is divided in a partition of N_e elements Ω_e. Following the classical Galerkin method, we multiply the equation by a smooth test function $v(x)$ and integrate over the local domain Ω_e:

$$\int_{\Omega_e} v \dot{f} dx + \int_{\Omega_e} v c f_x dx = 0. \tag{3.22}$$

This is known as the variational or weak formulation of the equation. The variables can always be approximated by a polynomial interpolation of order $P + 1$ in the element $f \approx \sum_{p=0}^{P} \varphi \bar{f}$ on the interpolation nodes x_p. The equation now reads

$$\int_{\Omega_e} v \left(\sum_{i=0}^{P} \dot{\bar{f}} \varphi_i \right) dx + \int_{\Omega_e} v \left(\sum_{i=0}^{P} c \bar{f} \partial_x \varphi_i \right) dx = 0. \tag{3.23}$$

This equation is equivalent to

$$\sum_{i=0}^{P} \dot{\bar{f}} \int_{\Omega_e} v\varphi_i dx + \sum_{i=0}^{P} c\bar{f} \int_{\Omega_e} v\partial_x \varphi_i dx = 0. \tag{3.24}$$

The test function v can be any of the interpolating functions φ_j, $j = 0, 1, \dots P$:

$$\sum_{i=0}^{P} \dot{\bar{f}} \int_{\Omega_e} \varphi_j \varphi_i dx + \sum_{i=0}^{P} c\bar{f} \int_{\Omega_e} \varphi_j \partial_x \varphi_i dx = 0., \quad j = 0, 1, \dots, P. \tag{3.25}$$

This permits to collect the equations in a linear system

$$M_e \dot{\bar{f}} + cD_e \bar{f} = 0. \tag{3.26}$$

where the matrices are defined as

$$\begin{aligned} M_e[j][i] &= \int_{\Omega_e} \varphi_j \varphi_i dx, \\ D_e[j][i] &= \int_{\Omega_e} \varphi_j \partial_x \varphi_i dx, \end{aligned} \tag{3.27}$$

and $\bar{f}$ are the vector of the discrete variables defined locally on the element Ω_e. This can be collected in a global formulation M and D to be able to solve the total system.

Coupling

The coupling between different domains is performed following a discontinuous Galerkin-FEM (DG-FEM) approach. Consider a domain $\Omega = \cup_{e=1}^{N}\Omega_e$ formed by N subdomains such that $\Gamma_e = \cap_{j=e-1}^{e+1}\Omega_e \neq \emptyset$. We evaluate the global variational formulation of the transport equation in the subdomain:

$$\int_{\Omega_e} \varphi_i \dot{f} dx + c \int_{\Omega_e} \varphi_i f_x dx = 0. \tag{3.28}$$

Integrating by parts once, the first derivative term becomes

$$\int_{\Omega_e} \varphi_i f_x dx = -\int_{\Omega_e} \partial_x \varphi_i f dx + \int_{\Gamma_e} \varphi_i f \hat{n} ds. \tag{3.29}$$

In classical DG strategy, we substitute the variable integrated on the boundary with a numerical flux term $\hat{f}$. Integrating a second time by parts, as suggested in [52, 92]:

$$\int_{\Omega_e} \varphi_i f_x dx = \int_{\Omega_e} \varphi_i f_x dx + \int_{\Gamma_e} \varphi_i (\hat{f} - f^-)\hat{n} ds. \tag{3.30}$$

The numerical flux term at the interface between adjacent elements is often based on Riemann solver [176, 61] for the advective part and on a local DG type [192] or hybridizable DG [159] for high order terms. Here, central fluxes have been used

$$\hat{f} = \frac{1}{2}(f^+ + f^-), \tag{3.31}$$

where $f_e = f(x_e^{\pm})$ is the value of f on the boundary, $x_e^{\pm} \in \Gamma_e$ inside the domain and $f_{e\pm1} = f(x_{e\pm1}^{\mp})$ the value of f on the boundary from the neighbour domain

$x_{e\pm1}^{\mp} \in \Gamma_{e\pm1}$. Using the interpolated functions, we have

$$\sum_{j=0}^{P} \bar{f} \int_{\Omega_e} \varphi_i \partial_x \varphi_j dx + \frac{1}{2} \int_{\Gamma_e} \varphi_i (\varphi_{i\pm1} f_{e\pm1} - \varphi_i f_e) \hat{n} ds \tag{3.32}$$

Solving the boundary integral

$$\int_{\Gamma_i} \varphi_i (\varphi_j f_{e\pm1} - \varphi_i f_e) \hat{n} ds = \varphi_i(x_e^+) \varphi_j(x_{e+1}^-) f_{e+1} - \varphi_i(x_e^+) \varphi_i(x_e^+) f_e$$
$$- (\varphi_i(x_e^-) \varphi_{e-1}(x_{e-1}^+) f_{e-1} - \varphi_i(x_e^-) \varphi_i(x_e^-) f_e). \tag{3.33}$$

The four boundary terms can be written as matrix-vector products as

$$\int_{\Omega_e} \varphi_i f_x dx + \int_{\Gamma_e} \varphi_i (\hat{f} - f^-) \hat{n} ds = Df + (\varphi_{i\pm1} f_{e\pm1} - \varphi_i f_e) \hat{n} ds$$
$$= Df + G_{e,e+1} f_{e+1} - H_e f_e - (F_{e,e-1} f_{e-1} - E_e f_e). \tag{3.34}$$

The matrices, over three adjacent domains Ω_e, Ω_{e-1} and Ω_{e+1}, are composed as

$$\begin{aligned} E_e &= \varphi_i(x_e^-) \varphi_i(x_e^-), \\ F_{e,e-1} &= \varphi_i(x_e^-) \varphi_j(x_{e-1}^+), \\ G_{e,e+1} &= \varphi_i(x_e^+) \varphi_j(x_{e+1}^-), \\ H_e &= \varphi_i(x_e^+) \varphi_i(x_e^+). \end{aligned} \tag{3.35}$$

In particular, the dimensions of E and H are $n_e \times n_e$, F are $n_e \times n_{e-1}$ and G are $n_e \times n_{e+1}$, being n_e, n_{e-1} and n_{e+1} the dimensions of the domains Ω_e, Ω_{e-1} and Ω_{e+1}. The first derivative matrix in the domain is defined as

$$Q_e = \sum_{j=0}^{P} \int_{\Omega_e} \varphi_i \partial_x \varphi_j dx + \frac{1}{2} \left(\varphi_i(x_e^+) \varphi_j(x_{e+1}^-) - \varphi_i(x_e^+) \varphi_i(x_e^+) \right.$$
$$\left. - \varphi_i(x_e^-) \varphi_j(x_{e-1}^+) - \varphi_i(x_e^-) \varphi_i(x_e^-) \right) . \tag{3.36}$$

Notice that the first derivative global matrix for n coupled domains can be written also as

$$Q = D + C + C_\pm. \tag{3.37}$$

where C is the term that represents the coupling matrices operating on the domain Ω while $C_\pm$ represents the coupling matrices operating on the neighbour domains $\Omega_\pm$.

The global discrete transport equation then becomes

$$M\dot{f} + cQf = 0, \tag{3.38}$$

where the global matrices, defined on Ω, are:

$$M_{Global} = M = \begin{bmatrix} \ddots & & & & \\ & M_{e-1} & 0 & & \\ & 0 & M_e & 0 & \\ & & 0 & M_{e+1} & \\ & & & & \ddots \end{bmatrix} . \tag{3.39}$$

$$\boldsymbol{Q}_{Global} = \boldsymbol{Q} = \begin{bmatrix} \ddots & & & & \\ & \boldsymbol{0} & -\frac{1}{2}\boldsymbol{F}_{e,e-1} & \boldsymbol{D}_e + \frac{1}{2}(\boldsymbol{E}_e - \boldsymbol{H}_e) & \frac{1}{2}\boldsymbol{G}_{e,e+1} & \boldsymbol{0} \\ & & & & & \ddots \end{bmatrix}. \quad (3.40)$$

3.3 Nonlinear dispersive wave-body discrete model

3.3.1 First order derivative formulation

As the domains are coupled through first order fluxes on the derivatives, the equations are re-written as a first order system by introducing auxiliary variables. In the free surface domain, unless otherwise stated, we will solve the 1D MS eqs.(2.130)

$$P_t + g q_x = 0, \quad (3.41a)$$
$$q_t + (qu)_x + dP_x = D, \quad (3.41b)$$
$$D = Bh_0^2 G_x + \alpha_{MS} h_0^2 dF_x, \qquad x \in \Omega_f, \quad (3.41c)$$
$$G - q_{xt} = 0, \quad (3.41d)$$
$$F - N_x = 0, \quad (3.41e)$$
$$N - P_x = 0, \quad (3.41f)$$

where we have multiplied the mass eq. (3.41) by g such that we can use the same set of variables (P, q), through all the domains. The transition domain ($c \in \Omega_l$) is given by eq. (3.41) with $D \equiv 0$. In the body domain we solve the non dispersive 1D NSW system (2.131)

$$q_t + (qu)_x + dP_x = 0, \quad (3.42a)$$
$$-w_x = -a + k_x, \qquad x \in \Omega_b, \quad (3.42b)$$
$$w - dP_x = 0, \quad (3.42c)$$
$$k - (qu)_x = 0. \quad (3.42d)$$

3.3.2 Variational formulation

Following the scheme presented previously, we multiply the eqs. (3.41) and (3.42) by a test function φ_i and integrate in each subdomain $\Omega_{w,l,b}$, to obtain the variational formulation. Compared to the transport eq. (3.21), this system presents some non-conservative terms, namely dP_x which are not continuous over the interface between the free surface and body domains. These non-conservative products are handled by introducing penalty terms consistent with the local linearization of the quasi-linear form of the system [29, 52, 136]. The variational form of the free surface system reads

$$\int_{\Omega_w} \varphi_i P_t dx + g \int_{\Omega_w} \varphi_i q_x dx + g \int_{\Gamma_o} \varphi_i [\![q]\!] \hat{n} dx = 0, \tag{3.43a}$$

$$\int_{\Omega_w} \varphi_i q_t dx + \int_{\Omega_w} \varphi_i (qu)_x dx + \int_{\Gamma_o} \varphi_i [\![qu]\!] \hat{n} dx$$
$$+ \int_{\Omega_w} \varphi_i dP_x dx + \int_{\Gamma_o} \varphi_i \hat{d} [\![P]\!] \hat{n} dx = \int_{\Omega_w} \varphi_i D dx, \tag{3.43b}$$

$$\int_{\Omega_w} \varphi_i D dx = B h_0^2 \left(\int_{\Omega_w} \varphi_i G_x dx + \int_{\Gamma_o} \varphi_i [\![G]\!] \hat{n} dx \right)$$
$$+ \alpha_{MS} h_0^2 \left(\int_{\Omega_w} \varphi_i dF_x dx + \int_{\Gamma_o} \varphi_i \hat{d} [\![F]\!] \hat{n} dx \right), \tag{3.43c}$$

$$\int_{\Omega_w} \varphi_i G dx - \int_{\Omega_w} \varphi_i q_{xt} dx - \int_{\Gamma_o} \varphi_i [\![q_t]\!] \hat{n} dx = 0, \tag{3.43d}$$

$$\int_{\Omega_w} \varphi F dx - \int_{\Omega_w} \varphi_i N_x dx - \int_{\Gamma_o} \varphi_i [\![N]\!] \hat{n} dx = 0, \tag{3.43e}$$

$$\int_{\Omega_w} \varphi_i N dx - \int_{\Omega_w} \varphi_i P_x dx - \int_{\Gamma_o} \varphi_i [\![P]\!] \hat{n} dx = 0. \tag{3.43f}$$

where

$$[\![f]\!] = \frac{1}{2}(f^+ - f^-) = \hat{f} - f^-. \tag{3.44}$$

The coefficient multiplying the non-conservative product is treated taking the average of the elevation at the two sides of the interface. This choice, although simple, has the advantage to recover the conservative form in the free surface region, as the boundary term results

$$\hat{d}[\![d]\!] = \frac{\hat{d}^2}{2} - \frac{(d^-)^2}{2}. \tag{3.45}$$

We report the variational formulation of the coupling layer here to highlight the border integrals: in Ω_l we are going to have the coupling terms with both domains, such that

$$\int_{\Omega_l} \varphi_i P_t dx + g \int_{\Omega_l} \varphi_i q_x dx + g \int_{\Gamma_o} \varphi_i [\![q]\!] \hat{n} dx + g \int_{\Gamma_i} \varphi_i [\![q]\!] \hat{n} dx = 0, \tag{3.46a}$$

$$\int_{\Omega_l} \varphi_i q_t dx + \int_{\Omega_l} \varphi_i (qu)_x dx + \int_{\Gamma_o} \varphi_i [\![qu]\!] \hat{n} dx + \int_{\Gamma_i} \varphi_i [\![qu]\!] \hat{n} dx$$
$$+ \int_{\Omega_l} \varphi_i dP_x dx + \int_{\Gamma_o} \varphi_i \hat{d} [\![P]\!] \hat{n} dx + \int_{\Gamma_i} \varphi_i \hat{d} [\![P]\!] \hat{n} dx = 0. \tag{3.46b}$$

$$\tag{3.46c}$$

The weak formulation in the body domain is evaluated in the same manner:

$$\int_{\Omega_b} \varphi_i q_t dx + \int_{\Omega_b} \varphi_i \left(qu \right)_x dx + \int_{\Gamma_i} \varphi_i [\![qu]\!] \boldsymbol{n} dx$$

$$+ \int_{\Omega_b} \varphi_i dP_x dx + \int_{\Gamma_i} \varphi_i \hat{d} [\![P]\!] \boldsymbol{n} dx = 0, \tag{3.47a}$$

$$- \int_{\Omega_b} \varphi_i w_x dx \int_{\Gamma_i} \varphi_i [\![w]\!] \boldsymbol{n} dx = - \int_{\Omega_b} \varphi_i a dx + \int_{\Omega_b} \varphi_i k_x dx + \int_{\Gamma_i} \varphi_i [\![k]\!] \boldsymbol{n} dx, \tag{3.47b}$$

$$\int_{\Omega_b} \varphi_i w - \int_{\Omega_b} \varphi_i dP_x - \int_{\Gamma_i} \varphi_i \hat{d} [\![P]\!] \boldsymbol{n} dx = 0, \tag{3.47c}$$

$$\int_{\Omega_b} \varphi_i k - \int_{\Omega_b} \varphi_i \left(qu \right)_x - \int_{\Gamma_i} \varphi_i [\![qu]\!] \boldsymbol{n} dx = 0. \tag{3.47d}$$

Proposition 2. *The variational formulations eqs.* (3.43), (3.46) *and* (3.47) *are exactly well balanced: the hydrostatic equilibrium in definition* 2 *is an exact solution of the weak form.*

Proof. The main idea of the proof is to show that replacing the steady state in eq. (2.142) with condition of eq. (2.143) in the variational form, results in an identity $0 = 0$. As in eq. (2.142) all the fluxes and velocities are zero, only the terms related to variations of the total pressure P may contribute to form non-zero fluxes. We look at each domain separately.

In the outer domain, by definition $\bar{P}_w = gh_0$ and constant in time. So eqs. (3.43b)-(3.43f) lead to $N = F = G = D = 0$. The only term which may remain is the one related to the jump of the total pressure between the outer domain and the coupling layer $\int_{\partial\Omega_w \cap \partial\Omega_l} \varphi_i [\cdot] \boldsymbol{n} dx$. However, as in the latter we also have by definition $\bar{P}_l = gh_0$, these jumps are also identically zero.

In the coupling layer $\bar{P}_l = gh_0$ and it is constant in time, so only terms which may give a non-zero contribution are the ones related to total pressure jump with the below body region $\int_{\partial\Omega_l \cap \partial\Omega_b} \varphi_i [\cdot] \boldsymbol{n} dx$. If $\bar{P}_b = gh_0$ too, then the proof is achieved. This is easily seen from the force balance on the body at steady state. In particular, substituting the hydrostatic equilibrium eq. (2.142) in the force balance (2.118) and using eq. (2.143), one gets to the condition

$$0 = \rho_w \int_{\Omega_w} \bar{P}_b dx - \rho_w \int_{\Omega_w} gh_0 dx, \tag{3.48}$$

which must be true independently of the body shape and the domain size. In particular, this is true if $\bar{P}_b = gh_0$ throughout the inner domain, which also satisfies the auxiliary relations eqs. (3.47c) and (3.47d). □

3.3.3 Space discrete formulation

We introduce an additional matrix to be able to write the space discrete formulation of the wave-body model. $\widetilde{Q}_e = \widetilde{Q}_e(d)$ is the first derivative matrix in the domain Ω_e dependent on the elevation and it can be evaluated using a projection method, as for a summation by parts scheme [151]. Consider the non conservative term dP_x, we define the weak formulation

$$dP_x \rightarrow \int_{\Omega} \varphi_i d_j \partial_x P dx + \int_{\Gamma} \varphi_j \hat{d} [\![P]\!] \boldsymbol{n} dx. \tag{3.49}$$

Since $\hat{d}$ are the average of the nodal values of d on the nodes, we can take it out of the border integral and the term $\int_{\Gamma} \varphi_j [\![P]\!] \boldsymbol{n} dx$ can be discretized in the classical way.

The integral over Ω can be solved defining the auxiliary function

$$w = P_x \rightarrow \int_\Omega \varphi w dx = \int_\Omega \varphi P_x dx + \int_\Gamma \varphi[\![P]\!] dx \rightarrow w = \boldsymbol{M}^{-1}(\boldsymbol{D} + \boldsymbol{C} + \boldsymbol{C}_-)P. \quad (3.50)$$

Moreover

$$f = dw \rightarrow \int_\Omega \varphi f dx = \int_\Omega \varphi dw dx \rightarrow \boldsymbol{M}f = \boldsymbol{M}\mathcal{D}_d w, \quad (3.51)$$

$$dP_x = \boldsymbol{M}\mathcal{D}_d\boldsymbol{M}^{-1}\boldsymbol{D}P + \hat{d}(\boldsymbol{C} + \boldsymbol{C}_+)P. \quad (3.52)$$

We can define the first order derivative dependent on d as

$$\begin{aligned}\tilde{\boldsymbol{Q}} &= \tilde{\boldsymbol{D}} + \tilde{\boldsymbol{C}} + \tilde{\boldsymbol{C}}_\pm \\ &= \boldsymbol{M}\mathcal{D}_d\boldsymbol{M}^{-1}\boldsymbol{D}\hat{d}(\boldsymbol{C} + \boldsymbol{C}_\pm).\end{aligned} \quad (3.53)$$
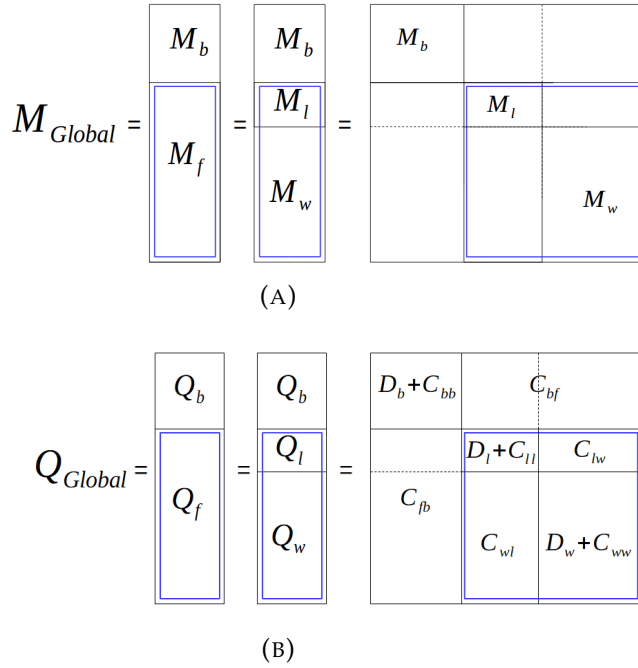

(A)

(B)

FIGURE 3.4 – Global mass matrix (a) and differentiation matrix (b).

A representation of the global matrices $\boldsymbol{M}$ and $\boldsymbol{Q}$ is presented in figure 3.4(a). Eqs. (3.41) and (3.42) in semi-discrete formulation are:

$$\boldsymbol{M}_{w,l}P_t + \boldsymbol{Q}_{w,l}q = 0, \qquad\qquad x \in \Omega_f, \qquad (3.54a)$$

$$\boldsymbol{L}_B q_t + \boldsymbol{Q}_w qu + \boldsymbol{B}_d^\alpha P = 0, \qquad\qquad x \in \Omega_w, \qquad (3.54b)$$

$$\boldsymbol{M}_{b,l}q_t + \boldsymbol{Q}_{q,l}qu + \tilde{\boldsymbol{Q}}_{b,l}\, P = 0, \qquad x \in \Omega_b \cup \Omega_l, \qquad (3.54c)$$

$$\boldsymbol{Q}_b\boldsymbol{M}_b^{-1}\, \tilde{\boldsymbol{Q}}_b\, P = -\boldsymbol{M}1a - \boldsymbol{Q}_b\boldsymbol{M}_b^{-1}\boldsymbol{Q}_b qu, \qquad x \in \Omega_b, \qquad (3.54d)$$

where 1 represents a vector of ones as the acceleration is a scalar variable. The linear global discrete operators introduced in eq. (2.53) in continuous form read

$$\boldsymbol{L}_B = \boldsymbol{M}_w - Bh_0^2\boldsymbol{Q}_w\boldsymbol{M}_w^{-1}\boldsymbol{Q}_w, \quad \boldsymbol{B}_d^\alpha = \tilde{\boldsymbol{Q}}_w + \alpha_{MS}h_0^2\, \tilde{\boldsymbol{Q}}_w\, \boldsymbol{M}_w^{-1}\boldsymbol{Q}_w\boldsymbol{M}_w^{-1}\, \tilde{\boldsymbol{Q}}_w\, . \quad (3.55)$$

Proposition 3. *The semi-discrete form eq. (3.54) is well balanced: the static equilibrium in eq. (2.142), with $\bar{a} = a = 0$, is exactly preseved.*

Proof. Identical to the variational case in proposition 2 □

3.4 Time discretization

The temporal domain is divided in a set of non-overlapping samples $[t^i, t^{i+1}]$, for $i = 0, 1, .., N_t$, where the t^i are called timesteps. The difference within the two timesteps is defined as $\delta t^{i+1} = t^{i+1} - t^i$. We are going to present two time integration methods, the Euler first order integration scheme and the backward differentiation formula of the third order. Notice that even if the Euler scheme permits a simple implementation and is A-stable [42], it should be used only in preliminary testing as it introduces dispersion and the characteristics of the waves are not preserved. High order schemes (at least third order) should be used in order to maintain the features of the space integration model. For both schemes, the dimension of the timestep is chosen by means of the Courant-Friedrichs-Lewy (CFL) condition [39, 55]:

$$\delta t^{i+1} = CFL \frac{(\min_i(\Delta x_i))^P}{\max_i(|u_i^n| - \sqrt{g d_i^n})}, \tag{3.56}$$

where CFL is a free parameter. For constant timestep and tuning the CFL parameter, we can evaluate a upper limit condition to choose the Δt:

$$\delta t \le CFL \frac{\min_i(\Delta x_i))^P}{\sqrt{g h_0}}. \tag{3.57}$$

This permits to have a error in time always dominated by the space error.

3.4.1 Discrete formulation

The fully discrete formulation of the wave-body system (3.54) evaluated at the timestep t^{n+1} reads

$$\begin{align}
\boldsymbol{M}_{w,l}\delta P^{n+1} + \boldsymbol{Q}_{w,l}q^{n+1} &= 0, & x \in \Omega_f, \tag{3.58a} \\
\boldsymbol{L}_B\delta q^{n+1} + \boldsymbol{Q}_w (qu)^{n+1} + \boldsymbol{B}_d^\alpha P^{n+1} &= 0, & x \in \Omega_w, \tag{3.58b} \\
\boldsymbol{M}_{b,l}\delta q^{n+1} + \boldsymbol{Q}_{q,l} (qu)^{n+1} + \tilde{\boldsymbol{Q}}_{b,l} P^{n+1} &= 0, & x \in \Omega_b \cup \Omega_l, \tag{3.58c} \\
- \tilde{\boldsymbol{Q}}_b \, \boldsymbol{M}_b^{-1}\boldsymbol{Q}_b P^{n+1} &= -\boldsymbol{M}1a^{n+1} - \boldsymbol{Q}_b\boldsymbol{M}_b^{-1}\boldsymbol{Q}_b (qu)^{n+1}, & x \in \Omega_b, \tag{3.58d}
\end{align}$$

where $\delta(\cdot)$ is the discrete representation of the time derivative $\partial_t(\cdot)$.

3.4.2 Euler scheme

The first time integration strategy that we consider is the Euler integration scheme. Considering the generic function $f(t)$, we define $f^n = f(t^n)$ the time discrete function. The integration method reads:

$$\delta t\delta f^{n+1} = f^{n+1} - f^n. \tag{3.59}$$

All the terms that are not derived in time should be evaluated through an linear extrapolation f^{ex} at the time t^{n+1} from the previous timesteps. For the Euler integration scheme, it simply resolves to evaluate the terms at the previous timestep $f^{ex} = f^n$. Notice that the operator B^d_α is evaluated with the extrapolated value of the elevation d^{ex}

3.4.3   eBDF3 scheme

Any backward differentiation scheme can be written in the form

$$\beta \delta t \delta f^{n+1} = \sum_{k=0}^{s} \alpha_k f^{n+1-k}, \tag{3.60}$$

where s is the order of the method. In particular, the parameters α_k and β of third order extrapolated backward differentiation scheme (eBDF3) [95, 104], are

$$\alpha_0 = 1, \alpha_1 = -\frac{18}{11}, \alpha_2 = \frac{9}{11}, \alpha_3 = -\frac{2}{11},$$
$$\beta = \frac{6}{11}. \tag{3.61}$$

The nonlinear terms are extrapolated at the timestep t^{n+1} through a Taylor approximation:

$$f^e = 3f^n - 3f^{n-1} + f^{n-2}. \tag{3.62}$$

The eBDF3 method is not A-stable but its stability is preserved for a $CFL = 1/3$ [94]. This method has been chosen because it is computationally inexpensive, once stored the information at the previous timesteps, the cost is equivalent to the Euler method. The method must be initialized for the steps $t = \{0, 1, 2\}$. Typically, we will not have an exact solution of the problem and the initialization is performed by a low order, single step time integration method, i.e. Euler method. These first two steps introduce a first order error time error in the simulation, diminishing the convergence rate of the model. However, we will show that in case of an exact or a manufactured solution, the method has a convergence rate of the third order.

3.5   Acceleration equation

As introduced in the continuous formulation section 2.3, the acceleration of the body can be evaluated from the Newton's second law. The discrete formulation of eq. (2.118)

$$m_b a = -g m_b + \rho_w \boldsymbol{w}^T \Pi_b. \tag{3.63}$$

Using the Gauss-Lobatto-Legendre integration weights $\boldsymbol{w}^T$, we can prove the following proposition.

Proposition 4. *Provided that the discrete operator $\tilde{K}$ is invertible, the discrete formulation of eq. (2.124) is*

$$(m_b + \boldsymbol{\mathcal{M}}_{add}) \, a^{n+1} = -g m_b - g \rho_w \boldsymbol{w}^T d_b - \rho_w \boldsymbol{w}^T \, \tilde{\boldsymbol{K}}_b^{-1} \left(\boldsymbol{Q}_b \boldsymbol{M}_b^{-1} \boldsymbol{Q}_b q u + \tilde{\boldsymbol{G}}_f \, P_f \right). \tag{3.64}$$

where the discrete added mass is defined as

$$\boldsymbol{\mathcal{M}}_{add} = \rho_w \boldsymbol{w}^T \, \tilde{\boldsymbol{K}}_d^{-1} \, \boldsymbol{w}. \tag{3.65}$$

Moreover, in case of constant depth and flat bottom body d_b^*, it can be shown that $\tilde{Q}_b = d_b^* Q_b$ and the matrix $\tilde{K}_b = d_b^* K_b$ is positive semi-definite (PSD) and thus the added mass is also non-negative

$$\mathcal{M}_{add} \geq 0 \tag{3.66}$$

Proof. Consider the discretized first order formulation in eqs. (3.41)-(3.42). Expanding the derivative matrices $\tilde{Q}_b$ and Q_b with their definitions (3.37) and (3.53):

$$-(D_b + C_{bb})w_b - C_{bf}w_f = -M_b 1 a + Q_b M_b^{-1} Q_b(qu), \tag{3.67a}$$

$$w_b = M_b^{-1}\left((\tilde{D}_b + \tilde{C}_{bb})P_b + \tilde{C}_{bf} P_f\right), \tag{3.67b}$$

$$w_f = M_f^{-1}\left((\tilde{D}_f + \tilde{C}_{ff})P_f + \tilde{C}_{fb} P_b\right). \tag{3.67c}$$

We define the matrices $\tilde{K}_b$ and $\tilde{G}_b$ using the definition of w_b and w_f

$$\begin{aligned}
\tilde{K}_b &= -(D_b + C_{bb})M_b^{-1}(\tilde{D}_b + \tilde{C}_{bb}) - C_{bf}M_f^{-1} \tilde{C}_{fb}, \\
\tilde{G}_f &= (D_b + C_{bb})M_b^{-1} \tilde{C}_{bf} + C_{bf}M_f^{-1}(\tilde{D}_f + \tilde{C}_{ff}).
\end{aligned} \tag{3.68}$$

From the definition of total pressure in eq. (2.93) and inverting $\tilde{K}_b$, the inner pressure Π_b is evaluated as

$$\Pi_b = -\tilde{K}_b^{-1}\left(M_b 1 a - Q_b M_b^{-1} Q_b qu - \tilde{G}_f P_f\right) - g d_b. \tag{3.69}$$

Substituting eq. (3.69) in the discrete acceleration eq. (3.63)

$$m_b a = -g m_b - \rho_w w^T \tilde{K}_b^{-1}\left(M_b 1 a - Q_b M_b^{-1} Q_b qu - \tilde{G}_f P_f\right) - g \rho_w w^T d_b. \tag{3.70}$$

We can demonstrate that $M_b 1 = w$

$$[M1]_i = \int_{\Omega_b} \sum_j^{N_{dof}} \varphi_i \varphi_j dx.$$

From the definition of GLL basis functions, we get that

$$\sum_j^{N_{dof}} \varphi_j = 1,$$

thus

$$[M1]_i = \int_{\Omega_b} \varphi_i dx,$$

and by analogy with the notation used for the pressure integral in the Newton second law eq. (3.63)

$$[M1]_i = w_i.$$

To show that the discrete added mass $\mathcal{M}_{add}$ is always non-negative for constant depth and flat bottom body, consider the quadratic function

$$w^T K_b w = -w^T (D_b + C_{bb}) M_b^{-1} (D_b + C_{bb}) w - w^T C_{bf} M_f^{-1} C_{fb} w.$$

The mass matrices M_b and M_f are positive definite (PD) so are also their inverse [93]. From eq. (3.36), we can define the matrices $D_b + C_{bb}$ and $\left(D_b + C_{bb}\right)^T$

$$[D_b + C_{bb}]_{ij} = \int_{\Omega_b} \varphi_i(\varphi_j)_x dx + 0.5 \int_{\partial\Omega_b} \varphi_i\varphi_j n|_{\partial\Omega_b} dx, \tag{3.71a}$$

$$\left[(D_b + C_{bb})^T\right]_{ij} = \int_{\Omega_b} (\varphi_i)_x\varphi_j dx - 0.5 \int_{\partial\Omega_b} \varphi_i\varphi_j n|_{\partial\Omega_b} dx. \tag{3.71b}$$

We also know that

$$\int_{\Omega_b} (\psi_i\psi_j)_x dx = \int_{\Omega_b} (\varphi_i)_x\varphi_j dx + \int_{\Omega_b} \varphi_i(\varphi_j)_x dx = \int_{\partial\Omega_b} \varphi_i\varphi_j n|_{\partial\Omega_b} dx. \tag{3.72}$$

Using eq. (3.72) in eq. (3.71a), it can be shown that

$$[D_b + C_{bb}]_{ij} = - \left[(D_b + C_{bb})^T\right]_{ij}. \tag{3.73}$$

Since the matrix M_b^{-1} is PD, it exists a unique PD matrix B_b such that $B_b^2 = B_b^T B_b = M_b^{-1}$ [93]. Thus, it holds the equivalence

$$-w^T \left(D_b + C_{bb}\right) M_b^{-1} \left(D_b + C_{bb}\right) w = -w^T \left(D_b + C_{bb}\right) B_b^T B_b \left(D_b + C_{bb}\right) w, \tag{3.74}$$

In the same way, for the free surface-body coupling matrices

$$\left[C_{bf}\right]_{ij} = 0.5 \int_{\partial\Omega_b \cap \partial\Omega_f} \varphi_i\varphi_j n|_{\partial\Omega_b} dx, \tag{3.75a}$$

$$\left[C_{fb}\right]_{ij} = 0.5 \int_{\partial\Omega_f \cap \partial\Omega_b} \varphi_i\varphi_j n|_{\partial\Omega_f} dx. \tag{3.75b}$$

and, since the normal vectors are pointing towards each other, $n|_{\partial\Omega_b} = -n|_{\partial\Omega_n}$, it can be shown that

$$\left[C_{bf}\right]_{ij} = - \left[C_{fb}^T\right]_{ij}. \tag{3.76}$$

Since also the matrix M_f is PD, it exists a matrix B_f such that $B_f^2 = B_f^T B_f = M_f^{-1}$ and

$$-w^T C_{bf} M_f^{-1} C_{fb} w = -w^T C_{bf} B_f^T B_f C_{fb} w, \tag{3.77}$$

As a consequence of eqs. (3.73) and (3.76), we can substitute the first $D_b + C_{bb}$ and C_{bf}

$$\begin{aligned}
-w^T \left(D_b + C_{bb}\right) B^T B_b \left(D_b + C_{bb}\right) w &- w^T C_{bf} B_f^T B_f C_{fb} = \\
&= w^T \left(D_b + C_{bb}\right)^T B^T B_b \left(D_b + C_{bb}\right) w + w^T C_{fb}^T B_f^T B_f C_{fb} = \\
&= \left(B \left(D_b + C_{bb}\right) w\right)^T B_b \left(D_b + C_{bb}\right) w + \left(B_f C_{fb} w\right)^T B_f C_{fb} w = \\
&= \left(B_b \left(D_b + C_{bb}\right) w\right)^2 + \left(B_f C_{fb} w\right)^2 \geq 0.
\end{aligned} \tag{3.78}$$

So K_b is positive semi-definite (PSD). When it is invertible also its inverse must be PSD [93] and the added mass is non-negative for constant depth and flat bottom body.   □

Chapter 4

1D numerical results

Sommaire

We have tested the 1D 'unified' spectral/*hp* Boussinesq model in several cases. The approach permits to simulate several combinations of free surface flow and fixed or floating structures. In particular, we discuss the convergence of the model in case of free surface and congested flow. Subsequently the numerical results on the study cases presented in chapter 3 are shown and, whenever possible, compared to analytic or reference (CFD or other) solutions to validate the model.

4.1 Manufactured solution

The study on the convergence of our approach has been done in two phases: first we have solved two coupled free surface subdomains, each modelled by a different Boussinesq model, and subsequently we have implemented a free surface-body coupling. As an exact solution does not exist for the MS model and even more for the free surface-body interaction, a manufactured solution has been implemented to study the convergence of the two tests.

4.1.1 Free surface convergence study

In this test we considered a periodical domain of length $L = 6\pi m$ modelled in $\Omega_w = [0, 2\pi] \cup [4\pi, 6\pi]$ by MS and from $\Omega_{NSW} = [2\pi, 4\pi]$ by NSW, coupled at 2π and at the periodic boundary. A known function $\zeta(\xi)$, with $\xi = kx - ct$, has been considered as solution of the two models. The manufactured variables of the models become

$$P^m(\zeta) = gd^m(\xi) = g(\zeta(\xi) + h0)$$
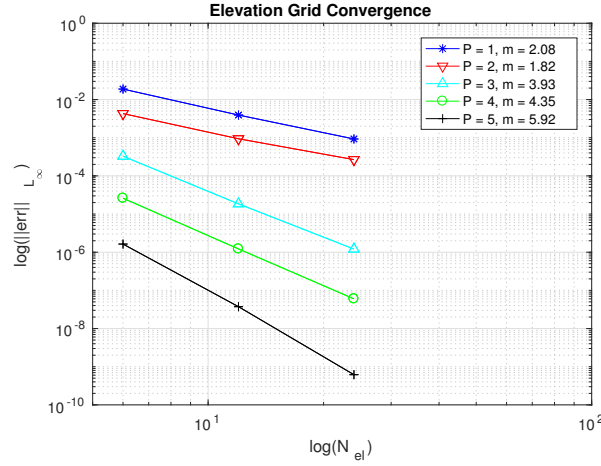$$u^m(\zeta) = c\zeta(\xi), \tag{4.1}$$
$$q^m(\zeta) = d^m(\xi)u^m(\xi).$$

FIGURE 4.1 – Convergence trend in a MS-NSW-MS model, with number of elements $N_{el} = [6, 12, 24]$ and polynomial orders $p = [1, 2, 3, 4, 5]$.

Clearly, eq.(4.1) will not satisfy exactly the MS system nor the NSW and the substitution of the variables P^m, d^m, u^m and q^m will result in a residual $r(\xi) \neq 0$. If we consider the residue as a source term, as

$$
\begin{aligned}
d_t + q_x &= r_d(\xi), \\
q_t + (qu_x) + gdP_x &= r_q^{NSW}(\xi), \quad \xi \in \Omega_{NSW}, \\
\mathcal{L}_B(q_t) + (qu_x) + g\mathcal{B}_\alpha^d(P) &= r_q^{MS}(\xi), \quad \xi \in \Omega_w,
\end{aligned}
\tag{4.2}
$$

the manufactured variables are exact solutions and they can be used to study the convergence. We have chosen $\zeta(\xi) = A\cos(\xi)$, where A, k and c are the wave amplitude, wave number and phase speed, since it is simple, periodic, $\mathcal{C}^\infty(\mathbb{R} \times \mathbb{R}_x)$ and we know all its derivatives. In the fully discretized space, the manufactured model is written as

$$
A\Delta U = RHS + M\tilde{r}^{n+1},
\tag{4.3}
$$

with the source term evaluated exactly at the new timestep. The theoretical convergence for the SEM is of order p for even polynomials and of order $p + 1$ for odd ones. Figure 4.1 shows the convergence of the mixed model problem for numbers of elements $N_{el} = [6, 12, 24]$ and polynomial orders $p = [1, 2, 3, 4, 5]$ and we can see that we reach the optimal rate of convergence.

4.1.2 Free surface-fixed body convergence study

The same approach has been used to validate the free surface-fixed body model. As shown in figure 4.2, the central NSW free surface domain Ω_{NSW} has been substituted by the inner domain Ω_b, a fixed pontoon of length $L = 2\pi$. The new manufactured solution reads

$$
\begin{aligned}
P^m(\xi) &= g(\zeta(\xi) + h0), \quad \xi \in \Omega_w \cup \Omega_b, \\
q^m(\xi) &= c\zeta(\xi)(\zeta(\xi) + h0), \quad \xi \in \Omega_w \cup \Omega_b \\
d^m(\xi) &= \begin{cases} \zeta(\xi) + h_0, & \xi \in \Omega_w, \\ h_0 - h_d, & \xi \in \Omega_b, \end{cases}
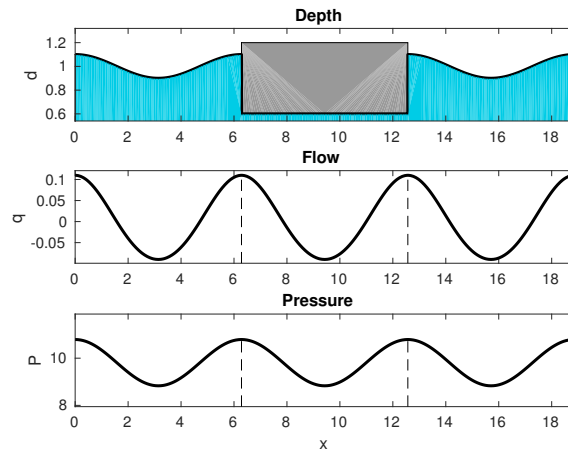\end{aligned}
\tag{4.4}
$$

FIGURE 4.2 – Solution of the manufactured problem for $p = 5$, with number of elements $N = 12$, final time $T = 2s$.

where h_d is the draft of the body. The convergence rate is presented in figure 4.3 for the variables of depth and total pressure. As we can see, we reach convergence rates are close to the optimal rate of convergence for odd polynomials and sub-optimal rate of p for even polynomial order. The sub-optimal convergence rate is probably due to the choice of centered fluxes as coupling method [37]
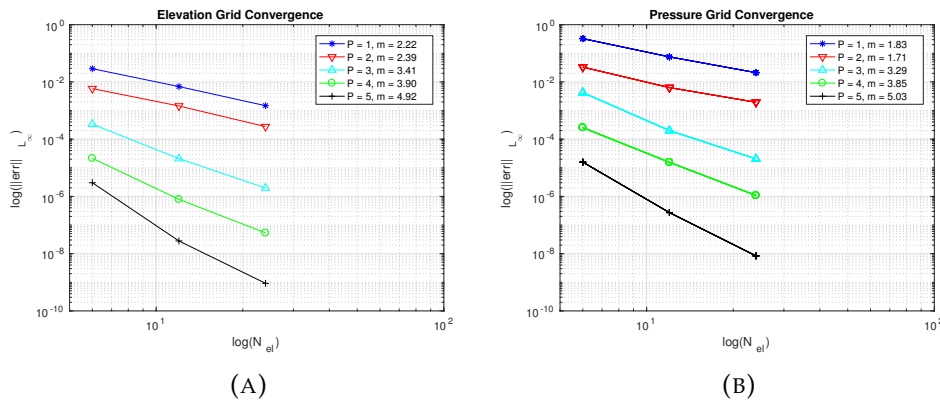

(A)

(B)

FIGURE 4.3 – Convergence trend in a MS-NSW-MS model, in figure (a) for the depth variables and in figure (b) for the total pressure variable.

4.1.3 Time Convergence

For the free surface-body manufactured solution we have studied also the time convergence, for the grid of $N_{el} = 12$ and polynomial order $p = 5$. The timestep δt for the eBDF3 integration method developed, is chosen in relation to the mesh size δx through a CFL condition [55]

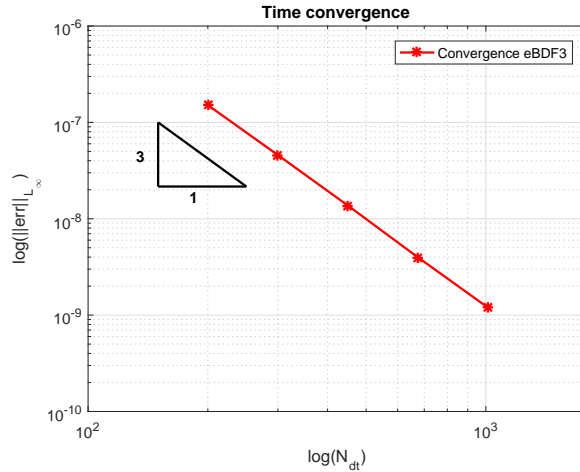$$\delta t \leq CFL \frac{\delta x}{\sqrt{gh_0 + |u|^2}}, \tag{4.5}$$

FIGURE 4.4 – Time Convergence for the fixed manufactured test.

such that the stability of the method is maintained. However, the error in space will always dominate the error in time when comparing the numerical solution to the exact one. Thus, we have evaluated a numerical reference solution with a time step of $\delta t = 2T / N_t$ where T is the wave period and $N_t = 64000$ is the total number of steps. The convergence is evaluated against this solution for $N_t = [200, 300, 450, 675, 1012]$. The resulting rate of convergence is presented in plot 4.4 and as we can see it is the optimal rate of the method.

Finally, we mention the efficiency of the spectral element method proposed. We have considered the problem presented in figure 4.2 with a mesh of $N_{el} = 12$ and $N_t = 5000$ over a simulation of one period $T = 1.95s$. As we can see from the convegence plots 4.3, from polynomial order $p = 1$ to $p = 5$ the error diminishes of five orders of magnitude while the simulation time remains almost constant. However, if the same precision has to be reached with linear elements, a much finer grid would be needed. Moreover, with 1500 DOF per domain against the 60 DOF of the high order polynomials the computational time becomes impractical, growing of five orders of magnitude.

4.2   Hydrostatic validation

For the hydrostatic case, Lannes has calculated the exact solution for the evolution of the contact point between free surface and body for a structure in forced motion and a semi-analytical solution for the position of the center of gravity of a body in decaying motion [111]. In this section, we are going to reproduce the results in [111] to validate the model for moving bodies. The basic setting for both cases is presented in figure 4.5. We consider a water flume of depth $h_0 = 15m$ that extends for $200m$ in both directions around the zero. The last $40m$ at both ends are part of a sponge layer that absorbs the incoming waves (cfr. section 2.5).

In all the test cases considered, $d_{target}(x) = h_0$ and $q_{target} = 0$. The density of water is set as $\rho_w = 1000kgm^{-3}$. The body placed with its center at $x = 0$ and its formed by a rectangular box of width $2R$ and height $H = 2R \sin(\pi/3) - R$, and a circular bottom of radius R, with the center passing through the vertical middle line of the body. The radius is $R = 10m$ and the density of the body is half the density of water ($\rho_b = 0.5\rho_w$). The free floating equilibrium position z^{eq} of the center of the
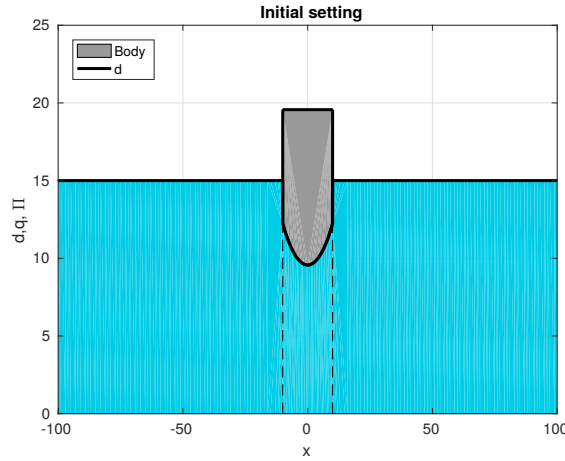
FIGURE 4.5 – Initial setting for the hydrostatic case tests.

body can be evaluated as

$$z^{eq} = \frac{R}{2} \left(1 - \frac{\rho_b}{\rho_w} \right) \left(\sqrt{3} - 2 + \frac{2\pi}{3} \right).$$ (4.6)

4.2.1 Forced motion test

In this test, the structure moves vertically in forced motion starting from the initial equilibrium position $z^{eq} = 4.57m$ and oscillates of $z = \pm 2m$ with a period $T = 10s$. The time dependent analytical solution of the water elevation at the contact points $x_{\pm}$ is

$$d_c(t, x_{\pm}) = \left(\tau_0 \left(\frac{x_+ - x_-}{4\sqrt{g}} v_G \right) \right)^2,$$

as it has been defined in section 4.2.1.

We can see in figure 4.6(a) the propagation of the wave generated by the forced motion of the body at $t = 6.66s$. Figure 4.6(b) shows the position of the contact point in time. The numerical solution presents the same behaviour of the exact solution. The error on the mass is evaluated with the body at the equilibrium position: the method conserves the mass within the limits of the finite domain and the absorption layer at the boundary.

Finally, in figure 4.6(d), we present a convergence study for 3 grids of $N_{el} = [25, 50, 100]$ and for polynomial order of $p = [1, 3, 5]$. Compared to the results of section 4.1.3, we have calculated a sub-optimal rate of convergence $rc = 1$ for all the mesh tested. This is probably due to the fact that the initializations of the first two steps of eBDF3 method are evaluated with Euler, instead of the exact solution and the initial first order error is then propagated to the rest of the simulation.

4.2.2 Decay motion test

For the decay test, the body presented in figure 4.5 is released from an initial position $z_0 = z_e - 2m$ and left to return to the equilibrium position. The semi-analytical solution of the position of the center of gravity δ_G has been anticipated in section
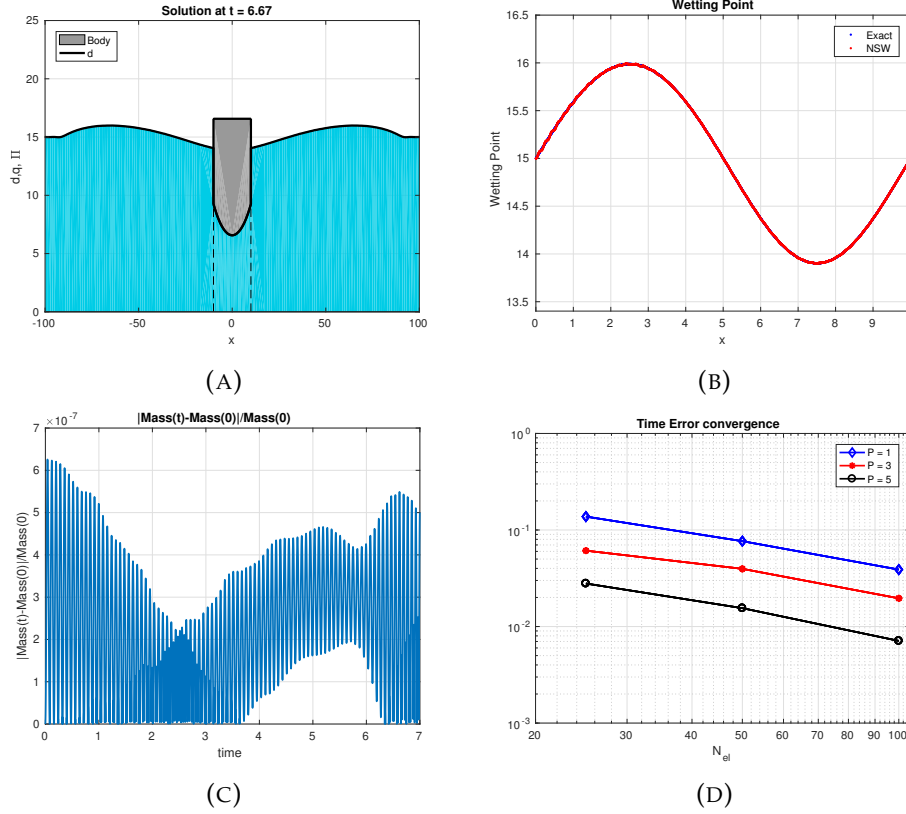
(A)

(B)

(C)

(D)

FIGURE 4.6 – Snapshot of the forced motion test case: (a) solution at $t = 6.66s$. Figure (b) shows the evolution of the contact point and the exact solution from eq. (2.147). Figure (c) shows the amount of error on the total mass during the simulation. Figure (d) Convergence in time for the forced motion test.

2.6.3 and reads:

$$
\begin{cases}
(m_b + m_{add})\ddot{\delta_G} = -c\delta_G - \nu(\dot{\delta_G}) + \beta(\delta_G)(\dot{\delta_G})^2 \\
(\delta_G, \dot{\delta_G})(t = 0) = (\delta_G^0, 0).
\end{cases}
\tag{4.7}
$$

Eq. (4.7) is solved at every timestep and allows us to validate our numerical solution.

As for the NSW scheme, the ODE (4.7) is solved by the eBFD3 time integration scheme, with the two initializing steps done by the Euler first order scheme, such that the two solutions are consistent in time. As we can see, the numerical and the semi-analytical solutions have a good agreement. The small difference in the peak at $t \approx 3s$ is probably due to Euler initialization at the first two steps that propagates in time two different errors, for 4.7 and 2.131, in the solutions. Also in this case the mass is kept constant within the limit of the absorption of the propagating wave.

4.3 Pontoon

This test case analyses the interaction of a fixed floating rectangular box with a weakly nonlinear solitary wave [55, 120, 154]. In particular, we are interested in reproducing the VOF-RANS results in [120] and FNPF results [55]. The basic setting is shown in figure 4.8. It consists in a rectangular box of length $L = 5m$ with a draft of $h_{draft} = 0.4m$ and total height of $0.6m$. The body is placed with the center of gravity

(A)   (B)

(C)   (D)
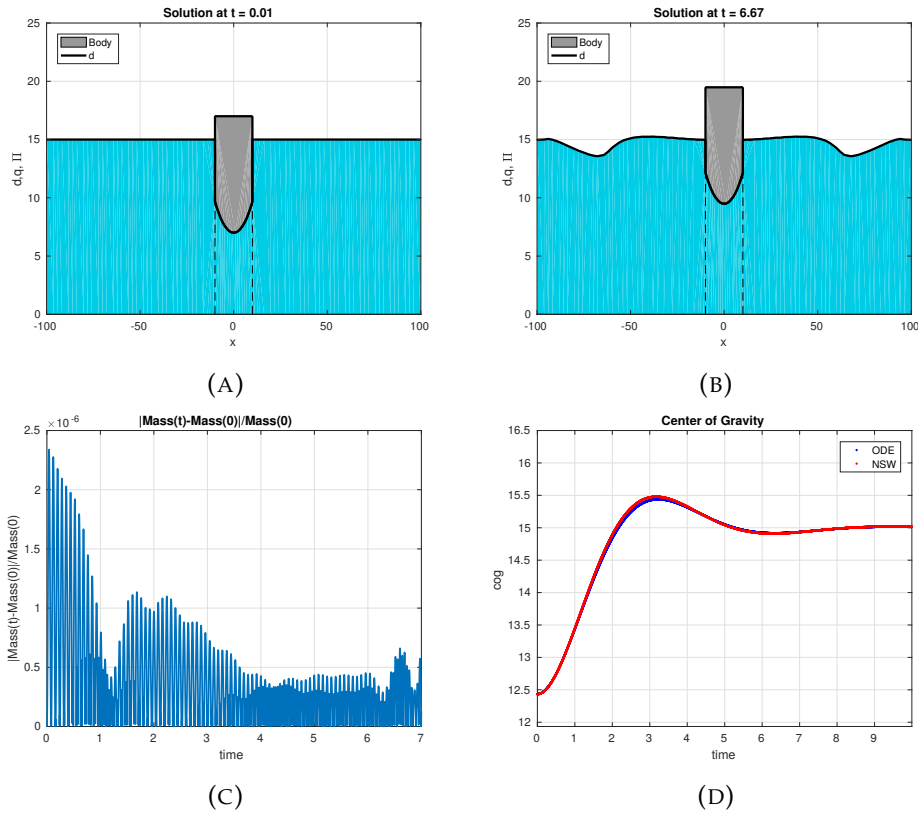
FIGURE 4.7 – Snapshot of the decay test case: (a) initial state, 4.7(b) solution at $t = 6.66s$. Figure (d) shows the evolution of the center of gravity and the exact solution and figure (c) the conserved mass of water during the simulation.
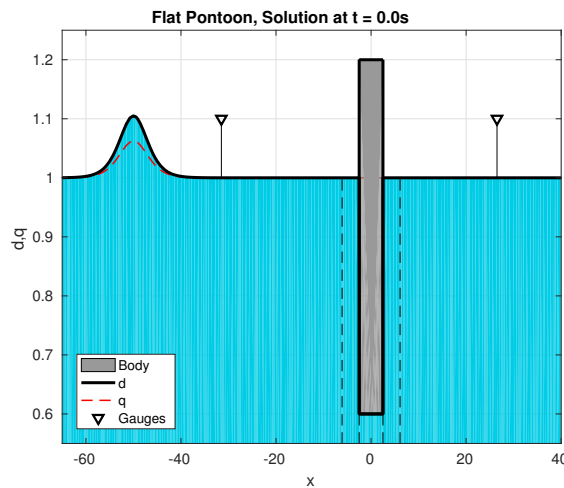

FIGURE 4.8 – Initial setting for the pontoon test case.

at $x = 0$ in a water flume that extends for $90m$ in both directions and constant depth $h_0 = 1m$. The last eighteen meters in both directions are used as an absorption layer. The two wave gauges are located at $G_1 = -31.5m$ and $G_2 = 26.5m$, to track the reflected and transmitted waves. The flume is discretized by a mesh of $N_w = 25$ elements in the water domain and of $N_b = 5$ elements in the inner one, for an higher resolution, and order $p = 3$ everywhere. The initial solitary wave is defined by the

GN exact solitary wave eq. (2.141).

From the original VOF-RANS test, we do not have any information about the generated wave but the initial elevation and adjusting γ, we can get a initial profile as similar as possible.

Due to the nonlinearity of the initial wave, the NSW model can not solve the propagation without the wave breaking, subsequently the free surface domain must be modelled by the MS system. However, thanks to proposition, the NSW model is used in the body domain to describe the congested flow. As introduced in section 2.2.3, we set up a NSW free surface coupling layer between the MS domain and the body domain. The length of the coupling layer has to be carefully calibrated and in the design of the pontoon test, the coupling layer has been kept as small as possible to avoid the distortion of the incoming wave and to permit the propagation of the dispersive characteristic of the solitary wave.
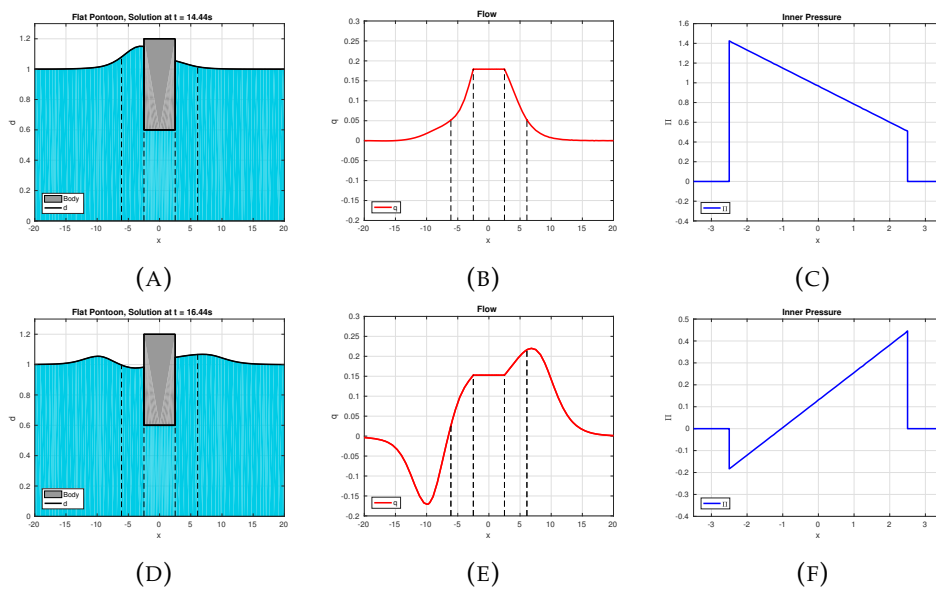
(A)

(B)

(C)

(D)

(E)

(F)

FIGURE 4.9 – Snapshot of the pontoon interacting with the incoming soliton at maximum and minimum wave elevation (*time* = $[14.44, 16.44]s$): (a) and (d) wave elevation, (b) (e) wave flow and (c) and (f) Inner pressure.

The plots in figure 4.9 show the snapshots of the solution at two different timesteps (*time* = $[14.44, 16.44]s$). We can see that the flow q of the wave remains continuous in the interaction with the body and the pressure Π under it evolves smoothly. The VOF-RANS and Boussinesq solutions are compared in figure 4.10(a): the top plot shows the incoming and reflected waves detected by the first gauge and the lower the transmitted ones. Considering the initial discrepancy between initial waves of the two tests, the results show a good agreement. Principally the MS solution overpredicts the peaks of the transmitted wave and under-predicts the trail of the reflected one but it still captures the salient characteristic of the solution. Finally we have tracked the error between the initial water mass and instantaneous waver mass, presented in figure 4.10(b). The error growing between $t = 0s - 20s$ is due to the absorption of the trail of the incoming soliton that travels in the $-x$ direction. The other growing trend is at $t > 35s$ when the transmitted and reflected wave arrive to the two sponge layers. Anyway, once the trail is absorbed, from $t \approx 20s$ to $t \approx 35s$ the total mass is conserved.
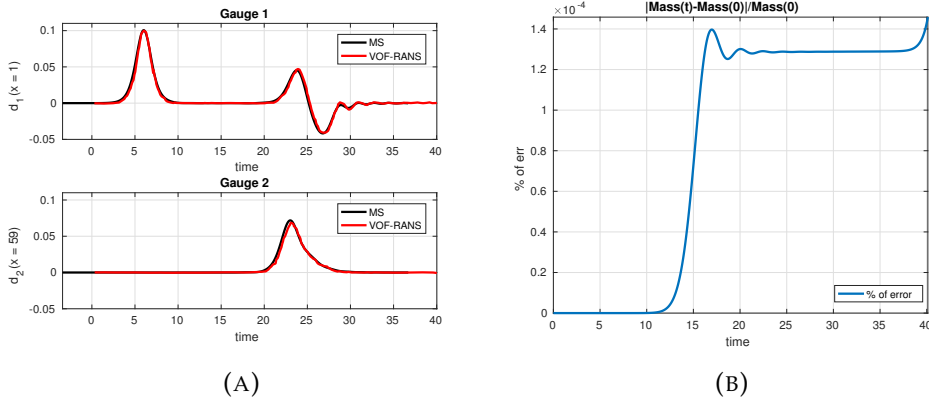
(A)

(B)

FIGURE 4.10 – (a) Elevation at the two gauges; (b), error in the total water mass during the simulation.

As we have seen in the forced and decay motion cases in section 4.2.1 and 4.2.2, this model can be easily modified to solve the case of a fixed pontoon with different bottom shapes and see how this effect the transmitted and reflected wave. In particular we tested a triangular bottom, a round parabolic bottom and a flat bottom with a deeper submerged area. The non-squared pontoons are designed to have a submerged volume equal to the one of the first test in figure 4.8. The mesh is the same as for the previous pontoon test. We see that the shape greatly affects the profile of the inner pressure (figures 4.9(f), 4.11(c), 4.11(f)). However, the transmitted and reflected waves are very similar to the original test, as we can see from the gauges plot in figure 4.11(j). For the fixed body setting the displaced volume (area in 2D) seems more important than the shape or the maximum depth. This is confirmed by the last test in figure 4.11(g), where we have a flat bottom pontoon that reaches the same maximum depth of the triangular one thus having a larger displaced area. From the gauges in figure 4.11(j) we see a substantial difference as the reflected wave is higher and the transmitted smaller. The force applied vertically by the wave on the bottom of the body in figure 4.11(k) is very similar in all the tests with the biggest difference seen after the peak of the wave has passed the body.

4.4 Heaving box

4.4.1 Single box

We consider a heaving box interacting with a stream function wave [64]. The basic setting shown in figure 4.12, consists of a rectangular box of length $l = 6m$ and height $= 10m$, with a displacement volume of $30m^2$ and density $\rho_b = 0.5\rho_w$ in a water flume. The flume has constant depth of $h_0 = 20m$ and its length is defined by the length of the propagating waves. In particular, the section left of the body is 5λ wavelength long, such that is accommodates a initial sponge layer (2λ), a generation layer of 1λ and a propagation section. The flume right to the body only needs to have an absorption section and it is long 4λ. The generation and absorption of waves is performed with the routine presented in section 2.5, where the wave elevation and flux are imposed as

$$d(x,t) = w(x)d(x,t) + \gamma(t)(1 - w(x))d_{target}(x),$$
$$q(x,t) = w(x)q(x,t) + \gamma(t)(1 - w(x))q_{target}(x),$$

(4.8)
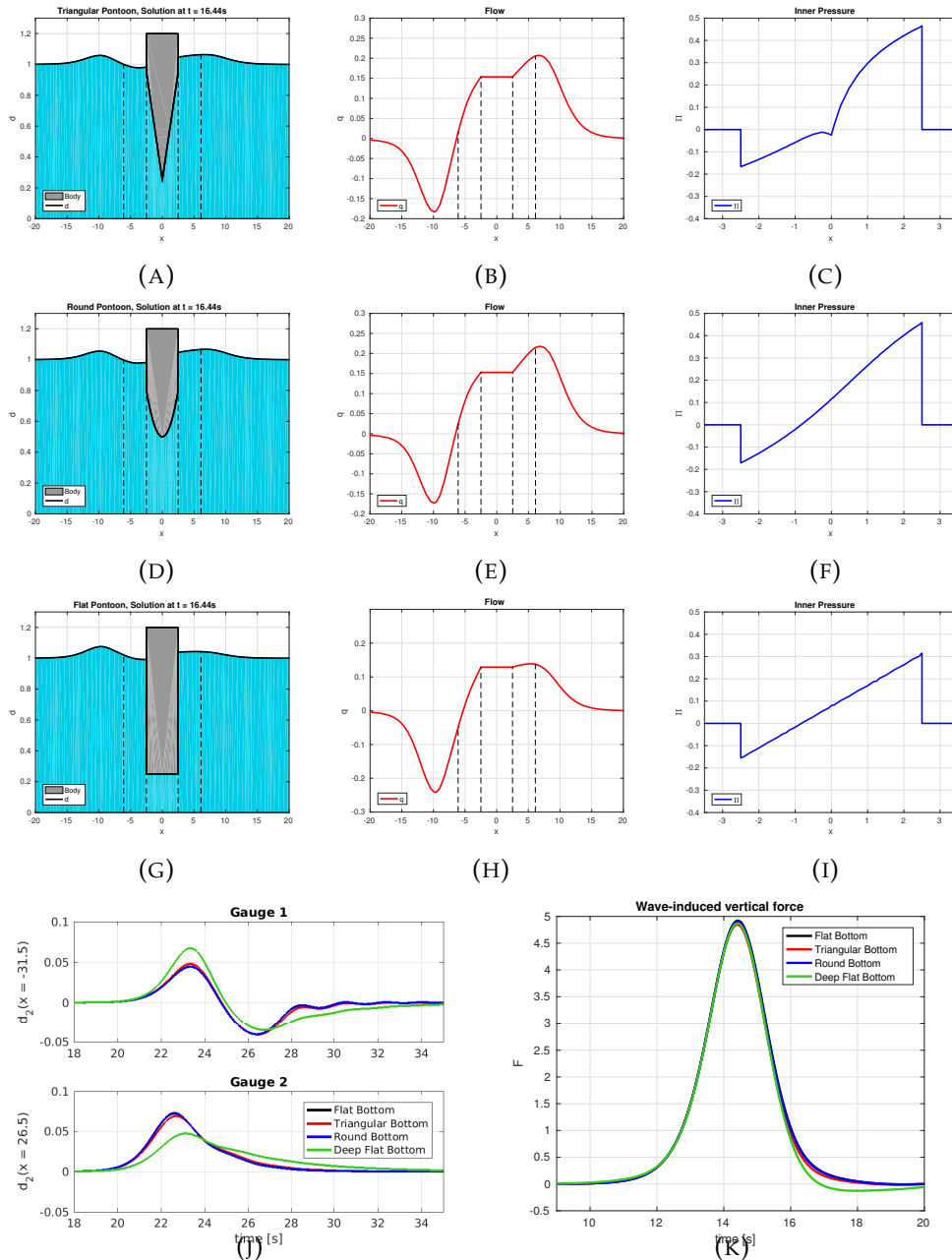
FIGURE 4.11 – Snapshot of the different bottom shaped pontoons at ($t = 16.44s$). Top row: triangular pontoon; Middle row: rounded pontoon; Bottom row: flat pontoon with large draft. Left column: wave elevation; Middle column: discharge; Right column: pressure on the body. The last two plots show (j) Surface elevation at the two gauges and (k) vertical force acting on the body.
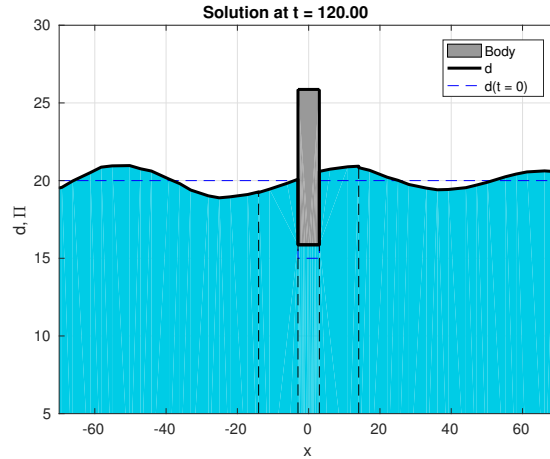
FIGURE 4.12 – Particular of the heaving body after 120s, for a stream
wave of period $T = 6s$ and steepness $\sigma = 0.025$.

where $w(x) \to [0, 1]$. Because of the nonlinear nature of the set of waves tested, the
outer domain must be solved with the MS equations. As in section 4.3, we define a
small NSW free surface coupling layer around the body, to couple the inner non dis-
persive model to the dispersive one. The NSW layer is calibrated to be long enough
such that we avoid the propagation of dispersive terms under the body, where they
are equal to zero and short enough to permit the propagation of the wave with min-
imal distortions. In practice, we have seen that $L_{NSW} = \frac{\lambda}{5}$, gives acceptable results.

Period $T[s]$	Amplitude $A[m]$	Steepness $\sigma[-]$
6.00	2.75×10^{-3}	10^{-4}
7.00	3.6×10^{-3}	10^{-4}
8.01	4.45×10^{-3}	10^{-4}
9.99	6.05×10^{-3}	10^{-4}
5.99	0.69	0.025
6.99	0.9	0.0249
8.01	1.12	0.025
10.01	1.53	0.025
5.97	1.38	0.0495
6.95	1.8	0.0494
7.92	2.23	0.0497

TABLE 4.1 – Period, amplitude and steepness of the wave tested

We tested three set of waves of increasing steepness $\sigma = \frac{A}{\lambda}$, where A is the wave
amplitude and λ the wave length. These are listed in the table 4.1. These waves have
been chosen to represent a fair range of waves in the application window of the MS
model, from very linear and long wave to weakly nonlinear ones. The outcome
results are presented in terms of a simplified Response Amplitude Operator (RAO)

$$RAO = \frac{\max(\eta_i) - \min(\eta_i)}{2A},\tag{4.9}$$

where η_i is the distance of the body center of gravity from the equilibrium position.

The RAO here represents an indication of the maximum displacement of the body interacting with a wave of amplitude A. The RAO evaluated from the Boussinesq simulation is then compared to the results given by the LPF and the CFD simulations. From the plot in figure 4.13, we notice that for linear waves (steepness $\sigma = 10^{-4}$), the Boussinesq model reproduces the behaviour of the linear model, with the characteristic peak at the resonance frequency $T = 5.6s$. For wave with a low steepness of $\sigma = 0.025$, the linear code presents the same behaviours for linear waves since the RAO in the linear model does not depend on the nonlinear characteristics of the incoming wave but only the period. However, for the Boussinesq code, we have an improved solution, being in good accordance with the outcome of the CFD model where the resonance peak at $T = 6s$ is about half the response of the linear model. For higher wave steepness in figure 4.15, the Boussinesq model, while improving the results of the linear code, can not fully catch the higher nonlinearity and the RAO has a value halfway between the linear and the RANS result. Note that for the fastest and shortest waves ($T < 6s$) we do not have any result for the Boussinesq model as we are outside its application window, suggesting that a Boussinesq model with improved properties should be used instead. Moreover, enhanced Boussinnesq models such as the Green-Naghdi [81] or the Nwogu [139], at the cost of a greater complexity, have a more complete description of nonlinearity and could improve the results for high steepness waves.
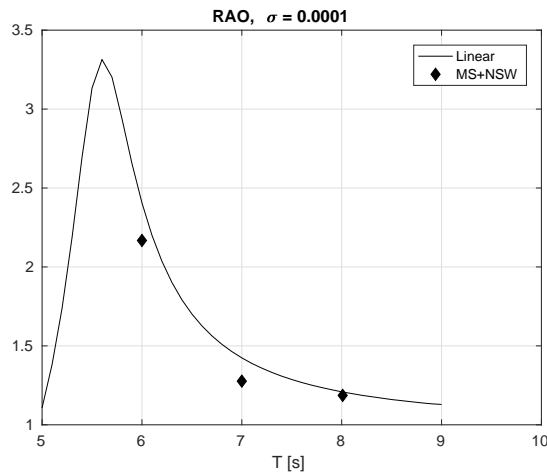

FIGURE 4.13 – RAO plot for a linear stream wave of steepness $\sigma = 0.0001$.

Nonentheless, the MS model greatly improves the results obtained by the simple linear code, at a fraction of the computational cost of a CFD simulation. Table 4.2 presents the performance of the RANS and the Boussinesq models in the form of computational time per wave period. The RANS simulations use existing codes on OpenFOAM [123] with a mesh of 250 000 cells for the waves of period $T = 6s$ and of 350 000 cells in the other cases. The Boussinesq simulations are done on a in-house code in Matlab [175] with a mesh of 51 elements in total and of polynomial order $p = 3$. As we can see from the table 4.2, the computational time per period used by the Boussinesq model is two to three orders of magnitude smaller than the CFD ones. This, together with the numerical results of the RAO of the heaving box in figures 4.13-4.15, confirms that the Boussinesq model is a cost effective alternative to a full RANS model if applied within the range of validity.
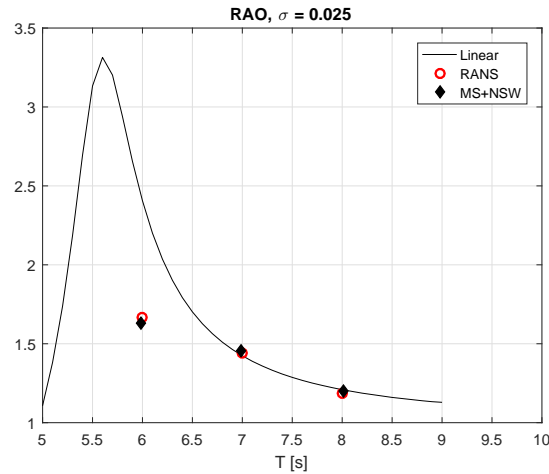
FIGURE 4.14 – RAO plot for a weakly nonlinear stream wave of steepness $\sigma = 0.025$.
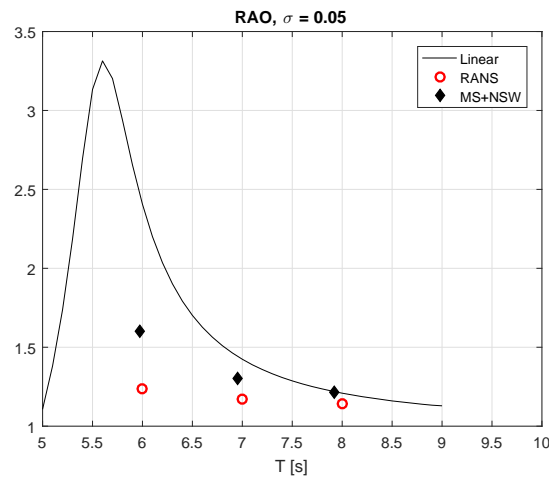
FIGURE 4.15 – RAO plot for a weakly nonlinear stream wave of steepness $\sigma = 0.05$.

σ	Period $T[s]$	CFD $[s/T]$	Boussinesq $[s/T]$
0.025	5.99	52 000	92
	6.99	77 000	123
	8.01	92 000	143
0.05	5.97	71 000	102
	6.95	120 000	120
	7.92	150 000	145

TABLE 4.2 – Computational effort per wave period for the CFD and Boussinesq models

4.4.2 Multiple bodies

Within our framework, we can use the domain decomposition to simulate multiple bodies. The scheme can simulate longer arrays but as a proof-of-concept and considering the limitation of a non-optimized code, we examine a small array of two bodies configuration, as shown in figure 4.16. Each body can be alternatively fixed or heaving. As matter of comparison for the dynamics of the two bodies, we

FIGURE 4.16 – Multi body problem. Each body can be either a fixed
pontoon or a heaving body. Here the simulation of two heaving bod-
ies with a wave of period $T = 10s$ and steepness $\sigma = 0.025$.

consider the setting of section 4.4.1: both bodies have length $l = 6m$ and height
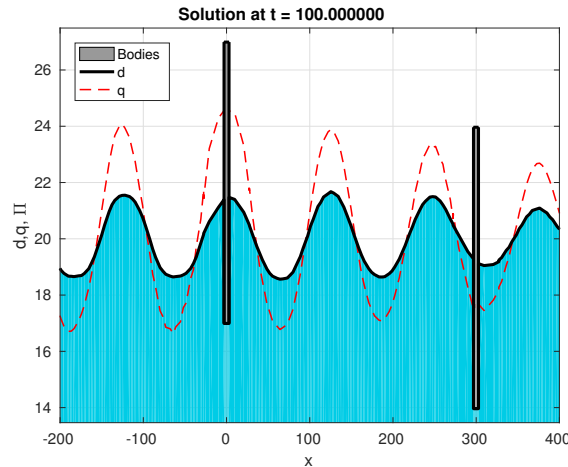$h_b = 10m$ in a flume of constant depth $h_0 = 20m$. The dimension of the free surface
domains is defined by the length of the wave tested, such that we can accommodate
the generation and the absorption layer. The left free surface domain is 5λ long and
the last domain is 4λ. The NSW layer around the bodies is a single element of length
equal to a fifth of a wave length. The polynomial order is $p = 3$. The length of the
central domain can affect the resulting dynamics of the body and at first is set to be
proportional to the wave length $L = 2\lambda$. The figure 4.17 shows the response of the
moving bodies of the simulations to four set of waves of period $T = [6, 7, 8, 10]s$ and
steepness $\sigma = [0.0001, 0.025]$. We can see from the figure 4.17, that the interaction of
the transmitted and reflected waves for the two bodies affects the RAO. We can see
that, a part from the short linear wave where the single body (the dashed line in the
plots) is at resonance frequency, the first body (blue stars and squares $*$, $\square$) benefits
by the reflected waves on the second one (red Xs and triangles $\times$, $\triangleleft$), especially when
the latter is another heaving body. It is interesting to notice that the variations of the
RAO of the two bodies present similar trends to the single body RAO, especially for
the more linear waves. This is probably do to the fact that the space between the to
bodies is not fixed through the different simulations but it is always proportional to
the wave length.

   We expect that the RAO can vary with less predictable trends in case the distance
is fixed, thus for the next case, we have tested the same set of waves with the two
bodies at a fixed distance of $20m$, shorter of any wavelength tested. Figure 4.18
shows the resulting RAO. In this case the reflected wave has a dampening impact
on the movement of the first body, resulting in it having a smaller movement than
the second one in most cases. This test shows also the importance, in the future, to be
able to optimize the placement of several bodies in such a way that the constructive
behaviours are enhanced and the destructive ones minimized.
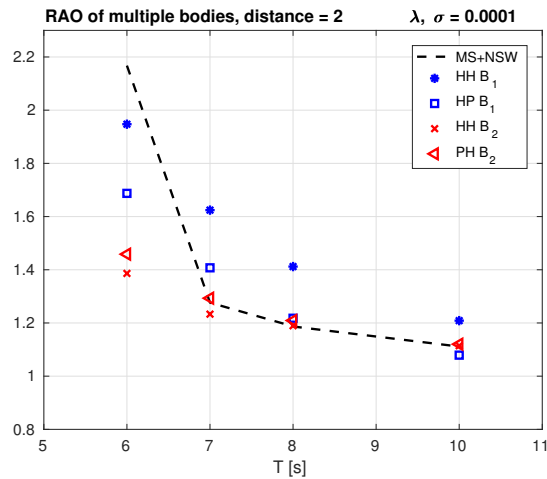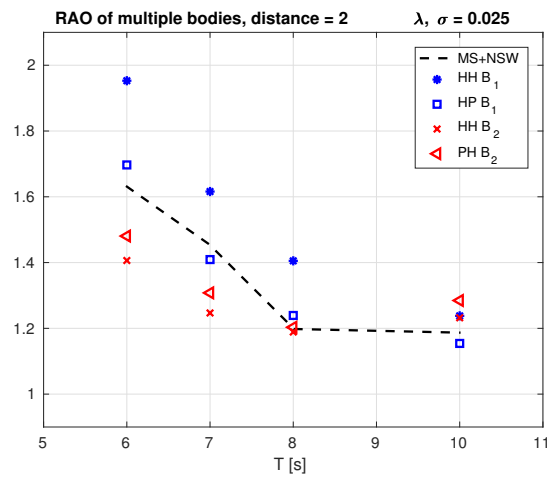
FIGURE 4.17 – RAO plots for a stream wave of period $T = [6, 7, 8, 10]s$ for the multiple bodies tests with the distance between the bodies dependent on the wave length $l = 2\lambda$, steepness $\sigma = 10^{-4}$ in figure (a) and $\sigma = 0.025$ in (b): the dashed line is the single body RAO, $*$ and $\times$ the first and second heaving bodies in series, $\square$ a heaving body in front of a pontoon and finally $\triangleleft$, a heaving body behind a pontoon.
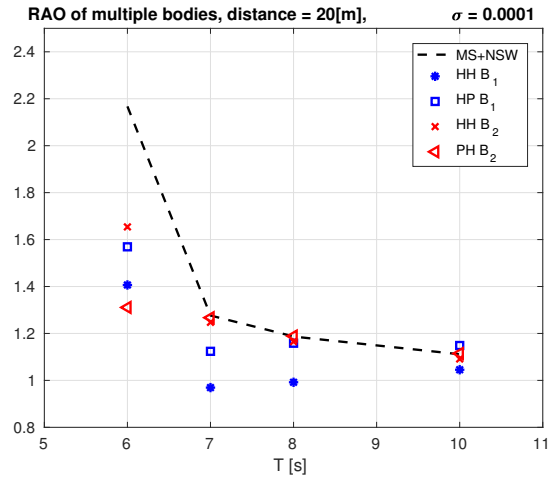
(A)
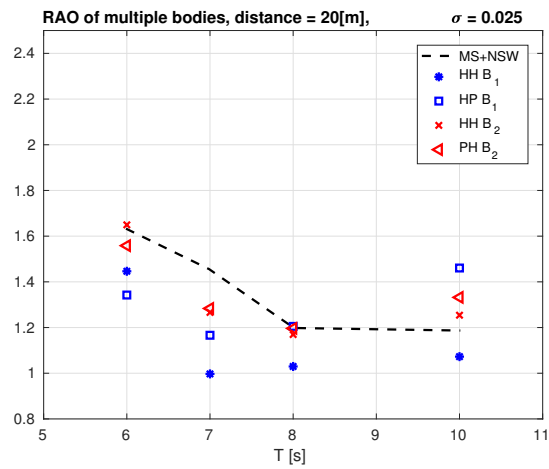
(B)

FIGURE 4.18 – RAO plots for a stream wave of period $T =$ [6, 7, 8, 10]s for the multiple bodies tests with the fixed distance between the bodies of 20m, steepness $\sigma = 10^{-4}$ in figure (a) and $\sigma = 0.025$ in (b): the dashed line is the single body RAO, $*$ and $\times$ the first and second heaving bodies in series, $\square$ a heaving body in front of a pontoon and finally $\triangleleft$, a heaving body behind a pontoon.

Chapter 5

Multidimensional extension

5.1 2D model

FIGURE 5.1 – 2D setup of the body problem.

The procedure to derive the one dimensional models performed in chapter 2 is general and can be applied to derivation of the two dimensional asymptotic model

[112]. Starting from the 3D Euler's equations

$$\begin{cases} u_x + v_y + w_z = 0 \\ u_t + uu_x + vu_y + wu_z + \frac{1}{\rho_w}p_x = 0, \\ v_t + uv_x + vv_y + wv_z + \frac{1}{\rho_w}p_y = 0, \\ w_t + uw_x + vw_y + ww_z + \frac{1}{\rho_w}p_z + g = 0. \end{cases} \tag{5.1}$$

The non-dimensional variables are evaluated in the free surface and body domain as in definition 1. The asymptotic development of the 3D Euler eq. 5.1 is equivalent to the 1D system and following the same steps, we obtain the two dimensional depth averaged model at different orders of precision. The 2D model are written in terms of the depth, velocity, flow and total pressure in $(x, y, t) = (\boldsymbol{x}, t) \in \Omega$:
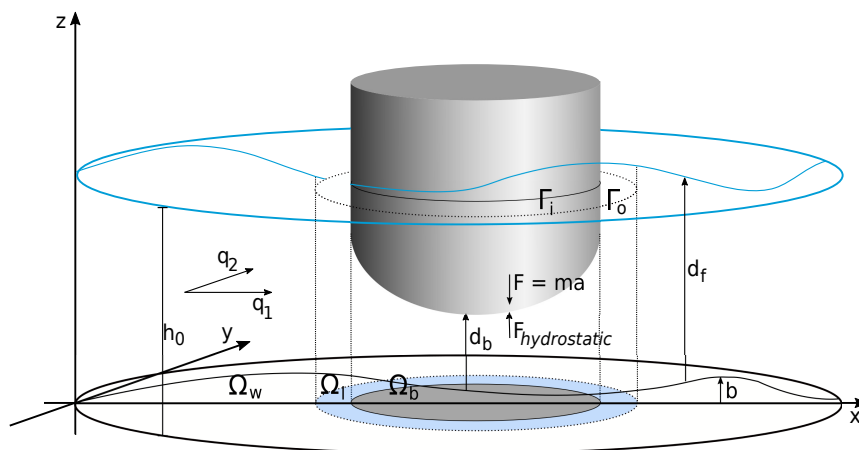
$$d = d(\boldsymbol{x}, t), \quad \bar{\boldsymbol{u}} = \begin{bmatrix} \bar{u}_1(\boldsymbol{x}, t) \\ \bar{u}_2(\boldsymbol{x}, t) \end{bmatrix}, \quad \bar{\boldsymbol{q}} = \begin{bmatrix} \bar{q}_1(\boldsymbol{x}, t) \\ \bar{q}_2(\boldsymbol{x}, t) \end{bmatrix}, \quad P = \Pi + gd,$$

where $\bar{u}_1, \bar{u}_2, \bar{q}_1$ and $\bar{q}_2$ are respectively the depth averaged velocity and flow in the x and y directions. We avoid to repeat the derivation of the asymptotic model and we report here only the final model for the free surface and the body domain. We are going to consider, as for the one dimensional models, only problems with a constant bathymetry $b(\boldsymbol{x}) = b_0 = 0$. From now on, we drop the $(\bar{\cdot})$ notation for the depth averaged variables, as they are the only variables considered.

5.1.1 Free surface domain

Here we present the two dimensional NSW, Abbott and MS model for the evolution of the free surface domain Ω_w.

Two dimensional NSW model. At the asymptotic precision of $\mathcal{O}(\mu^2)$, the two dimensional nonlinear shallow water (2D NSW) system reads

$$d_t + \nabla \cdot \boldsymbol{q} = 0, \tag{5.2a}$$
$$\boldsymbol{q}_t + \nabla \cdot (\boldsymbol{q} \otimes \boldsymbol{u}) + d\nabla P = 0. \tag{5.2b}$$

The derivative operators $\nabla(\cdot)$ and $\nabla \cdot (\cdot)$ represent respectively the gradient and the divergence operators. The tensor product $\otimes$ is defined as

$$\boldsymbol{f} \otimes \boldsymbol{g} = \begin{bmatrix} f_1 g_1 & f_1 g_2 \\ f_2 g_1 & f_2 g_2 \end{bmatrix}, \quad \text{with } \boldsymbol{f} = \begin{bmatrix} f_1 \\ f_2 \end{bmatrix}, \; \boldsymbol{g} = \begin{bmatrix} g_1 \\ g_2 \end{bmatrix}.$$

Two dimensional Abbott model. Including in the approximation the terms of order $\mathcal{O}(\varepsilon\mu^2, \mu^4)$, we have the two dimensional Abbott model. In terms of $d(x, y, t)$ and flux $\boldsymbol{q}(x, y, t)$, it reads

$$d_t + \nabla \cdot \boldsymbol{q} = 0,$$
$$\boldsymbol{q}_t + \nabla \cdot (\boldsymbol{q} \otimes \boldsymbol{u}) + d\nabla P = \frac{h_0^2}{3}\nabla(\nabla \cdot \boldsymbol{q}_t). \tag{5.3}$$

Two dimensional MS model. The two dimensional MS model can be deducted from the 2D Abbott equations as in chapter 2. The relation (2.50) is valid also in 2D

and reads

$$q_t = -h_0 \nabla d + \mathcal{O}(\varepsilon, \mu^2).$$

such that

$$\nabla(\nabla \cdot q_t) = h_0 \nabla(\Delta d) + \mathcal{O}(\varepsilon, \mu^2).$$

where $\Delta = \nabla \cdot (\nabla)$ is the Laplacian operator.

Defining the two dimensional linear operator

$$\mathcal{L}_B(\cdot) = \left(1 - Bh_0^2 \nabla(\nabla \cdot)\right), \quad \mathcal{B}_d^\alpha(\cdot) = d\nabla \left(1 + \alpha_{MS} h_0^2 \Delta\right), \tag{5.4}$$

the 2D MS model is:

$$\begin{aligned} d_t + \nabla \cdot q &= 0, \\ \mathcal{L}_B(q_t) + \nabla \cdot (q \otimes u) + \mathcal{B}_d^\alpha(P) &= 0. \end{aligned} \tag{5.5}$$

As for the 1D model, setting the free parameter B and α_{MS} to zero, permits to retrieve the NSW model. The optimal values to enhance the linear dispersion properties are $\alpha_{MS} = 1/15$ and $B = 1/3 + \alpha_{MS}$.

Linear dispersion relation. We refer to the 1D linear dispersion discussion in chapter 2 as the same conclusions can be deduced in terms of precision and application window of the three 2D model presented.

5.1.2 Body NSW model

In the two dimensional inner domain Ω_b, we can still prove the following result:

Proposition 5. *In Ω_b, under the standard assumptions of the Boussinesq theory*

$$\mu^4 \ll 1, \quad \varepsilon \approx \mu^2,$$

in absence of pitch, roll and yawn, all high order dispersive terms are negligible.

Proof. Consider the high order term of the Abbott model $\nabla(\nabla \cdot (q_t))$. As the function and it's derivative in space and time are continuous, we can invert the order of the derivative as $\nabla(\nabla \cdot (q)_t)$. Taking the derivative in time and the gradient of the mass eq. (5.2a), we have that

$$\nabla(d_{tt}) = -\nabla((\nabla \cdot q)_t).$$

But $d_{tt} = a$ is the vertical acceleration of the body, which in absence of pitch, roll or yawn is constant in space and $\nabla a = 0$, thus

$$\nabla(\nabla \cdot q_t) = 0.$$

$\square$

Proposition 5 implies that the dispersion effects under the body are negligible and we can use the 2D NSW model

$$d_t + \nabla \cdot q = 0, \tag{5.6a}$$
$$q_t + \nabla \cdot (q \otimes u) + d\nabla P = 0. \tag{5.6b}$$

The expression for the pressure is evaluated taking the divergence of the momentum eq. (5.6b):

$$\nabla \cdot (d\nabla P) = \nabla \cdot q_t + \nabla \cdot (\nabla \cdot (q \otimes u)).$$

As for the 1D model, we can define the acceleration of the body evaluating the time derivative of the mass equation (5.2a), such that the pressure equation becomes

$$\nabla \cdot (d \nabla P) = -a + \nabla \cdot (\nabla \cdot (\boldsymbol{q} \otimes \boldsymbol{u})). \tag{5.7}$$

Finally, the acceleration is evaluated from the Newton's second law

$$m_b a = -g m_b + \int_{\Omega_b} \Pi_b \hat{\boldsymbol{n}} d\boldsymbol{x}, \tag{5.8}$$

where $d\boldsymbol{x} = dxdy$ is the infinitesimal area and $\hat{\boldsymbol{n}}$ the outward normal vector to the body.

5.1.3   Coupling domains

As for the 1D problem in section 2.2.3, the coupling between the free surface domain and the body domain, is handled by introducing a small non-dispersive layer Ω_l around the body where we solve the 2D NSW eqs. (5.2). This layer is introduced to be able to compute some conservation laws, in particular energy and mass conservation.

Conservation relations

Let consider the free surface and body domain $\Omega = \Omega_b \cup \Omega_l$ with the interface $\Gamma_i = \Omega_b \cap \Omega_l$ as in figure 5.1. The general NSW system is:

$$\begin{aligned} \eta_t + \nabla \cdot (\boldsymbol{q}) &= 0, \\ \boldsymbol{q}_t + \nabla \cdot (\boldsymbol{q} \otimes \boldsymbol{u}) + d \nabla (g\eta + \Pi) &= 0, \end{aligned} \tag{5.9}$$

where Π is the pressure at $z = d$. By definition we have $\Pi = \Pi_{air} = 0$ in Ω_l and $\Pi = \Pi_b$ in Ω_b. The energy conservation statement can be obtained multiplying the components of system (5.9) by the vector $\boldsymbol{V} = \left[g\frac{\eta^2}{2} + \Pi - k, \boldsymbol{u} \right]$, where we have denoted $k = \boldsymbol{u}^2/2 = \boldsymbol{u} \cdot \boldsymbol{u}/2$ the kinetic energy, with $\cdot$ the scalar product. After simple manipulation, we obtain the 2D formulation of eq. (2.100):

$$\left(g\frac{\eta^2}{2} + dk \right)_t + \nabla \cdot (\boldsymbol{q}(g\eta + \Pi + k)) = -\mathcal{W}, \tag{5.10}$$

where $\mathcal{W} = \Pi d_t$ is the power transmitted/absorbed to/from the free surface or body. Setting

$$E = g\frac{\eta^2}{2} + dk, \quad \boldsymbol{F} = \boldsymbol{q}(g\eta + \Pi + k), \tag{5.11}$$

we can write compactly

$$E_t + \nabla \cdot (\boldsymbol{F}) = -\mathcal{W}. \tag{5.12}$$

The same conservation relation (5.10) can be evaluated for the free surface domain $\Omega_f = \Omega_w \cup \Omega_l$. In Ω_f both Π and $\mathcal{W}$ are zero and we recover the classical energy conservation for the shallow water equations. As for the 1D energy conservation law, eq. (5.12) represents the energy conservation only for fixed structures while for moving bodies it provides an energy balance. We can now couple the two domains, in particular the eqs. (5.9) and the pressure eq. (5.7). We define the vector $\boldsymbol{x} = (x, y)$

Assuming that

$$\lim_{\substack{\boldsymbol{x}\in\Omega_b \\ \boldsymbol{x}\to\Omega_l}} \boldsymbol{q} = \lim_{\substack{\boldsymbol{x}\in\Omega_l \\ \boldsymbol{x}\to\Omega_b}} \boldsymbol{q},$$

$$\lim_{\substack{\boldsymbol{x}\in\Omega_b \\ \boldsymbol{x}\to\Omega_l}} \boldsymbol{F} = \lim_{\substack{\boldsymbol{x}\in\Omega_l \\ \boldsymbol{x}\to\Omega_b}} \boldsymbol{F},$$
(5.13)

denoting by $\mathcal{M}$ and $\mathcal{E}$ the total volume of water and the total energy in the domain Ω, we can write

$$\mathcal{M}(t) = \mathcal{M}(0) - \int_0^t \int_{\Omega_b} \mathcal{V}\boldsymbol{dx}t$$

$$\mathcal{E}(t) = \mathcal{E}(0) - \int_0^t \int_{\Omega_b} \mathcal{W}\boldsymbol{dx}dt$$
(5.14)

which state that the initial volume (and thus the mass) and energy are conserved modulo the integral of the volume $\mathcal{V}$ of the body and power pushed in/out by the body.

Note that the definition of energy fluxes $\boldsymbol{F}$ and the relations in (5.13) imply the continuity of the dynamic pressure:

$$\lim_{\substack{x\in\Omega_b \\ x\to\Omega_l}} (g\eta + \Pi + k) = \lim_{\substack{x\in\Omega_l \\ x\to\Omega_b}} (g\eta + \Pi + k) = \lim_{\substack{x\in\Omega_l \\ x\to\Omega_b}} (g\eta + k).$$
(5.15)

This relation can be considered as a coupling condition on Γ_i.

Finally, we can deduce the continuity of the nonlinear terms $\mathcal{N}$

$$\mathcal{N} = \nabla \cdot (\boldsymbol{q} \otimes \boldsymbol{u}) + g\nabla \left(\frac{d^2}{2}\right) + d\nabla(\Pi),$$
(5.16)

as a consequence of the continuity of the fluxes q. From eq. (5.13):

$$\lim_{\substack{\boldsymbol{x}\in\Omega_b \\ \boldsymbol{x}\to\Omega_l}} \boldsymbol{q}_t = \lim_{\substack{\boldsymbol{x}\in\Omega_l \\ \boldsymbol{x}\to\Omega_b}} \boldsymbol{q}_t.$$
(5.17)

we can use eq. (5.9) to argue that

$$\lim_{\substack{\boldsymbol{x}\in\Omega_b \\ \boldsymbol{x}\to\Omega_l}} \mathcal{N} = \lim_{\substack{\boldsymbol{x}\in\Omega_l \\ \boldsymbol{x}\to\Omega_b}} \mathcal{N}.$$
(5.18)

Coupling conditions

The choice of the coupling conditions in two dimensions replicates the one dimensional coupling conditions. We aim to conserve the total mass of the system and the continuity of the hydrostatic pressure.

Mass conservation   As seen in the previous section, the conservation of global mass stems from the continuity of the normal component of the flux $\boldsymbol{q}$. Denoting the outward one dimensional normals directions to the free surface and body domain by $\hat{\boldsymbol{n}}_l$ and $\hat{\boldsymbol{n}}_b$, and by $\boldsymbol{q}$ the flux vector, we can define the jump at the interface as

$$[\![\boldsymbol{q}\cdot\hat{\boldsymbol{n}}]\!] := \boldsymbol{q}_b \cdot \hat{\boldsymbol{n}}_b + \boldsymbol{q}_l \cdot \hat{\boldsymbol{n}}_l.$$
(5.19)

Thus, the conservation of total mass is equivalent to

$$\llbracket \boldsymbol{q} \cdot \hat{\boldsymbol{n}} \rrbracket = 0. \tag{5.20}$$

Hydrostatic total pressure continuity   From a physical point of view, one may argue that in the hydrostatic approximation the value of the pressure at the boundaries of the body domain should match the hydrostatic pressure in the free surface region.This condition, while based on physical grounds, is not consistent with the conservation of total energy. The continuity condition for the hydrostatic total pressure $P = \Pi + gd$ reads:

$$\llbracket P \rrbracket = 0. \tag{5.21}$$

5.2   Body dynamics and added mass effects

In the case of freely floating object, the acceleration of the body has to be solved to evaluate the instantaneous position of the body and the dynamic pressure Π_b. As introduced the acceleration can be evaluated from the Newton second law, eq. (5.8). The dynamic pressure can be obtained from the definition of total pressure $\Pi_b = P - gd$. Consider now the pressure eq. (2.131b). We define a linear operator, dependent on the depth d, $\mathcal{K}_d = -\nabla \cdot (d\nabla(\cdot))$, such that we can rewrite eq. (5.7) as

$$\mathcal{K}_d(P) = -a + \nabla \cdot \nabla \cdot (\boldsymbol{q} \otimes \boldsymbol{u}). \tag{5.22}$$

If the operator $\mathcal{K}_d$ admits an inverse operator $\mathcal{K}_d$, we can evaluate an expression for the total pressure under the body

$$P = \mathcal{K}_d^{-1} \left(-a + \nabla \cdot (\nabla \cdot (\boldsymbol{q} \otimes \boldsymbol{u})) \right). \tag{5.23}$$

Substituting this definition into the Newton's second law eq. (5.8) and considering that for purely heaving body, the acceleration is not dependent on $\boldsymbol{x}$, we have an expression for the acceleration:

$$\left(m_b + \rho_w \int_{\Omega_b} \mathcal{K}_d^{-1}(\boldsymbol{1}) d\boldsymbol{x} \right) a = -g m_b + \rho_w \int_{\Omega_b} \left(\mathcal{K}_d^1 \nabla \cdot (\nabla \cdot (\boldsymbol{q} \otimes \boldsymbol{u})) - gd \right) d\boldsymbol{x}. \tag{5.24}$$

where $\mathcal{M}_{add}$ is the *added mass* as in the 1D model:

$$\mathcal{M}_{add} = \rho_w \int_{\Omega_b} \mathcal{K}_d^{-1}(\boldsymbol{1}) d\boldsymbol{x} \tag{5.25}$$

since it has the dimension of a mass. The expression of the inverse operator and the added mass in two dimension have been calculated in semi-analytical form in the paper of David Lannes [111].

5.3   Model summary

We summarize here the complete 2D wave-body model used to solve the evolution of the free surface domain $\Omega_f = \Omega_w \cup \Omega_l$ and body domain Ω_b.

The free surface MS-NSW model reads

$$
\begin{aligned}
&d_t + \nabla \cdot \boldsymbol{q} = 0, \quad \boldsymbol{x} \in \Omega_f \\
&\mathcal{L}_B(\boldsymbol{q}_t) + \nabla \cdot (\boldsymbol{q} \otimes \boldsymbol{u}) + \mathcal{B}_d^\alpha(P) = 0, \\
&(\alpha_{MS}, B) = \begin{cases} (1/15, 1/3 + \alpha_{MS}), & x \in \Omega_w, \\ (0, 0), & x \in \Omega_l, \end{cases}
\end{aligned}
\tag{5.26}
$$

where the operators $\mathcal{L}_B$ and $\mathcal{B}_d^\alpha$ had been defined in eq. (5.4). The equations of the body domain are

$$
\begin{aligned}
&d_t + \nabla \cdot \boldsymbol{q} = 0, \\
&\boldsymbol{q}_t + \nabla \cdot (\boldsymbol{q} \otimes \boldsymbol{u}) + d\nabla P = 0, \quad \boldsymbol{x} \in \Omega_b, \\
&\mathcal{K}_d(P) = -a + \nabla \cdot \nabla \cdot (\boldsymbol{q} \otimes \boldsymbol{u}).
\end{aligned}
\tag{5.27}
$$

The exchange of mass and fluxes through the interfaces Γ_i and Γ_o is performed by imposing the continuity of mass, the continuity of the momentum variation and the hydrostatic total pressure presented in section 2.2.3. On the body-coupling layer interface, considering that $\hat{\boldsymbol{n}}_b = -\hat{\boldsymbol{n}}_l$, the coupling reads

$$
\left.\begin{aligned}
[\![\boldsymbol{q}]\!]_{\Gamma_i} = 0 \rightarrow \boldsymbol{q}_b(x_i, t) = \boldsymbol{q}_l(x_i, t), \\
[\![P]\!]_{\Gamma_i} = 0 \rightarrow P_l(x_i, t) = P_b(x_i, t).
\end{aligned}\right\} \quad x_i \in \Gamma_i = \Omega_l \cap \Omega_b.
\tag{5.28}
$$

These are a direct consequence of the conservation of mass eq. (2.110) and the wave elevation continuity eq. (2.115). The coupling between the coupling layer and the outer MS domain reads

$$
\left.\begin{aligned}
[\![d]\!]_{\Gamma_o} \rightarrow d_w(x_o, t) = d_l(x_o, t), \\
[\![\boldsymbol{q}]\!]_{\Gamma_o} \rightarrow \boldsymbol{q}_w(x_o, t) = \boldsymbol{q}_l(x_o, t).
\end{aligned}\right\}, \quad x_o \in \Gamma_o = \Omega_w \cap \Omega_l.
\tag{5.29}
$$

The coupling conditions in the outer domain imply also

$$
\boldsymbol{q}_w(x_o, t) - \boldsymbol{q}_l(x_o, t) = \boldsymbol{u}_w d_w(x_o, t) - \boldsymbol{u}_l d_l(x_o, t) = 0 \rightarrow [\![\boldsymbol{u}]\!]_{\Gamma_i} = 0,
\tag{5.30}
$$

and the momentum variation continuity condition is automatically verified.

Finally, the acceleration equation that permits us to define the position of the body in time

$$
(m_b + \mathcal{M}_{add}) a = -g m_b + \rho_w \int_{\Omega_b} \left(\mathcal{K}_d^1 \nabla \cdot (\nabla \cdot (\boldsymbol{q} \otimes \boldsymbol{u})) - g d \right) d\boldsymbol{x}.
\tag{5.31}
$$

The model is closed imposing some conditions on the outer border. In this case we have imposed wall conditions

$$
\hat{\boldsymbol{n}}_{\Gamma_w} \cdot (\boldsymbol{q}(\boldsymbol{x}, t) \hat{\boldsymbol{n}}_{\Gamma_w}) = \boldsymbol{0},
\tag{5.32}
$$

where the $\hat{\boldsymbol{n}}_{\Gamma_w}$ is the outer pointing normal vector to $\Gamma_w = \partial \Omega_w$. This choice is done in the attempt to keep the computational domain shorter than what would be imposing absorption domains close to the border, thus keeping the simulation more efficient.

5.3.1 Analytical solution

Definition 3. *We define as hydrostatic equilibrium, the state*

$$(d_{w,l}, d_b, P, \boldsymbol{q}, \boldsymbol{u}, a) = (h_0, d_b, gh_0, \boldsymbol{0}, \boldsymbol{0}, 0), \tag{5.33}$$

with d_b and h_0 as the equilibrium depths under the body and in the free surface regions, linked by the hydrostatic equilibrium relation

$$\frac{m_b}{\rho_w} = \int_{\Omega_b} (h_0 - d_b) dx. \tag{5.34}$$

5.4 2D SEM

The extension of the 1D SEM method introduced in chapter 3 to two dimensions is conceptually straightforward. However it presents some additional complexity to the previous case. The computational domain Ω is dividen in N_{el} triangular elements as shown in figure 5.2.
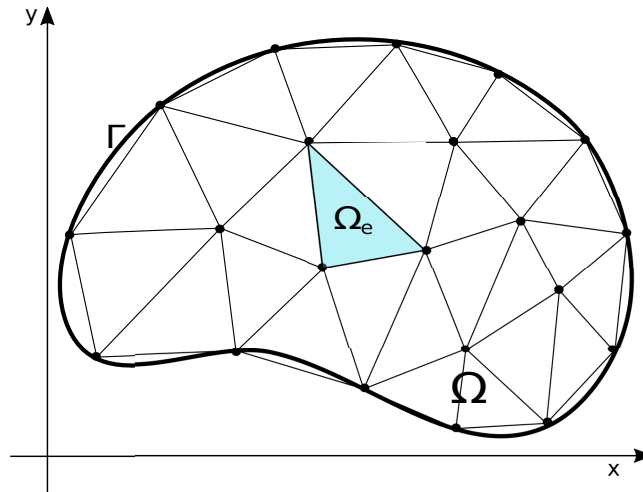
FIGURE 5.2 – A domain Ω with boundary Γ divided in a triangular mesh of N_{el} elements Ω_e.

5.4.1 Basis functions

A function $u(\boldsymbol{x})$ can always be represented by the sum of piece-wise polynomial functions

$$u(\boldsymbol{x}) \approx \hat{u}(\boldsymbol{x}) = \sum_{j=1}^{M} \hat{u}_j \varphi_j(\boldsymbol{x}), \tag{5.35}$$

where $\phi_j(\boldsymbol{x}) \in \Phi$ is a global basis function that satifies the Cardinal property (3.5) at the i'th node

$$\varphi_j(\boldsymbol{x}_i) = \delta_{ij}.$$

Each global function is defined on the entire domain Ω, but it has local support only on the local domain Ω_e and at most the neighbouring ones.

Similarly to the formulation in one dimension, each global basis function $\varphi_j(\boldsymbol{x})$ can be represented by the combination of local ones $\varphi_j^{(e)}(\boldsymbol{x})$

$$\varphi_j^{(e)} = \bigoplus_{e=1}^{N} \sum_{i=1}^{P} \varphi_j^{(e)}(\boldsymbol{x}_i) \varphi_j^{(e)}(\boldsymbol{x}), \tag{5.36}$$

where the local basis functions are multivariate polynomials belonging to the e'th element and defined on the set of interpolation nodes. The basis functions are defined in the space

$$\Phi = \{\varphi \in L^2(\Omega) : \varphi|_{\Omega_e} \in \mathbb{P}^p(\Omega_e), \forall \Omega_e \in \Omega\}.$$

The 2D polynomial space $\mathbb{P}^p$ can be defined as the span of all the polynomial functions at most of order p [84, 100, 148]

$$\mathbb{P}^p = \text{SPAN}(x^\alpha y^\beta), \quad \alpha, \beta \geq 0, \ \alpha + \beta \leq p.$$

The complete polynomial space $\mathbb{P}^p$ will have dimension $\frac{1}{2}(p+1)(p+2)$. The function $u(\boldsymbol{x})$ can be locally interpolated by

$$\hat{u}^{(e)}(\boldsymbol{x}) = \sum_{i=1}^{P} u(x_j) \varphi_j^{(e)}(\boldsymbol{x}_i) \varphi_j^{(e)}(\boldsymbol{x}). \tag{5.37}$$

Basis functions for triangulation

In this thesis we have implemented the unstructured orthogonal basis functions proposed by Proriol [149] and more recently by Dubiner [51] in two horizontal dimensions. As for the 1D model, we define the standard two dimensional triangular element Ω_s

$$\mathcal{T}_s = \{(r,s)| -1 \leq r,s; r+s \leq 0\}. \tag{5.38}$$

The definition of a standard element permits to relate all the different elements to the same basis functions everywhere and adapt them to each element through a simple mapping. The nodes in the reference triangle are defined by the so called *collapsed coordinate system* [100] which maps $\mathcal{T}_s$ to the reference quadrilateral

$$a = 2\frac{1+r}{1-s}, \ b = s. \tag{5.39}$$

The reference triangle, defined by the collapsed coordinate, becomes

$$\mathcal{T}_s = \{(a,b)| -1 \leq r,s \leq 1\}. \tag{5.40}$$

The advantage of the expression (5.40) is that it has independent limits and the two dimensional expansion of the basis functions can be constructed as the tensor product of the one dimensional functional spaces (3.1) (i.e. Legendre-Lagrange tensor basis in L^2). The two dimensional orthogonal polynomial basis functions are defined as

$$\varphi_{pq}(r,s) = \varphi_p^a(r)\varphi_q^b(s), \qquad p,q \geq 0,$$

where the one dimensional basis functions can be evaluated using the Jacobi polynomials of order p, $P_p^{\alpha,beta}$, presented in section 3.2.1

$$\varphi_p^a(r) = P_p^{0,0}(r), \quad \varphi_p^b(r) = \left(\frac{1-s}{2}\right)^p P_p^{2p+1,0}(s). \tag{5.41}$$

5.4.2   Discrete formulation

Element matrices

We discuss here the formulation of the mass and derivative matrices for the 2D SEM. Let us consider the PDE

$$\dot{f}(\boldsymbol{x}, t) + \partial_x f(\boldsymbol{x}, t) = 0, \tag{5.42}$$

where $f(\boldsymbol{x}, t)$ is a smooth continuous function defined in $(\boldsymbol{x}, t) = (x, y, t) \in \Omega \times \mathbb{R}^+$. We consider here the derivative in the x direction, however the deduction of the y derivative matrix is done in the same manner. Following the Galerkin framework, we evaluate the variational formulation

$$\int_\Omega v \dot{f} \, d\boldsymbol{x} + \int_\Omega v \partial_x f \, d\boldsymbol{x} = 0, \tag{5.43}$$

where $v = v(\boldsymbol{x})$ is a test function. The exact solution f is approximated by

$$\bar{f} = \sum_{j=1}^{M} \bar{f}_j \varphi_j(\boldsymbol{x}) \tag{5.44}$$

where $\varphi_j(\boldsymbol{x})$ is a global basis function over Ω. Since we can not guarantee the continuity of the derivative of the global basis functions across the the elements, we switch to the local representation of the approximated solution, knowing that the global solution can be retrieved through direct summation of the solution in all elements. In the local triangular domain, the basis functions are continuous and differentiable such that we can define in Ω_e the approximations

$$\bar{f} = \sum_{i=1}^{N} \bar{f}_i \varphi_i^{(e)}(\boldsymbol{x}), \quad \partial_x \bar{f} = \sum_{i=1}^{N} \bar{f}_i \partial_x \varphi_i^{(e)}(\boldsymbol{x}). \tag{5.45}$$

Assuming that the test functions in each elements are taken as the basis function $v^{(e)}(\boldsymbol{x}) = \varphi_j^{(e)}(\boldsymbol{x})$, the variational formulation can be written as

$$\int_{\Omega_e} \varphi_j^{(e)} \sum_{i=1}^{N} \dot{\bar{f}}_i \varphi_i^{(e)}(\boldsymbol{x}) \, d\boldsymbol{x} + \int_{\Omega_e} \varphi_j^{(e)} \sum_{i=1}^{N} \bar{f}_i \partial_x \varphi_i^{(e)}(\boldsymbol{x}) \, d\boldsymbol{x} = 0. \tag{5.46}$$

The two integrals give us the basic blocks to build the matrices. Each entry of the matrices can be written as

$$\begin{aligned}
\boldsymbol{\mathcal{M}}^{(e)}[i][j] &= \int_{\Omega_e} \varphi_j^{(e)} \varphi_i^{(e)} \, d\boldsymbol{x}, \\
\boldsymbol{\mathcal{D}}_x^{(e)}[i][j] &= \int_{\Omega_e} \varphi_j^{(e)} \partial_x \varphi_i^{(e)} \, d\boldsymbol{x}
\end{aligned} \tag{5.47}$$

It is convenient to employ the reference triangle $\mathcal{T}_s$ in the (r, s)-coordinate system (5.38) to evaluate the matrices's elements. The elements Ω_e are mapped to $\mathcal{T}_s$ using a Gordon-Hall transfinite interpolation procedure [79]. Through chain rule and the

mapping, the integrals in the reference triangle are

$$\int_{\Omega_e} \varphi_j^{(e)}(\boldsymbol{x})\varphi_i^{(e)}(\boldsymbol{x})d\boldsymbol{x} = \mathcal{J}^{(e)}\int_{\mathcal{T}_s} \varphi_j^{\mathcal{T}_s}(r,s)\varphi_i^{\mathcal{T}_s}(r,s)drds,$$

$$\int_{\Omega_e} \varphi_j^{(e)}(\boldsymbol{x})\partial_x\varphi_i^{(e)}(\boldsymbol{x})d\boldsymbol{x} = \qquad (5.48)$$

$$\mathcal{J}^{(e)}\int_{\mathcal{T}_s} \varphi_j^{\mathcal{T}_s}(r,s)\left(r_x\partial_r\varphi_i^{\mathcal{T}_s}(r,s) + s_x\partial_s\varphi_i^{(e)}(r,s)\right)drds,$$

where r_x, s_x are geometric weights and $\mathcal{J}^{(e)}$ the Jacobian of the transformation map between Ω_e and $\mathcal{T}_s$. The mass matrix can be thus defined as

$$\boldsymbol{\mathcal{M}}^{(e)} = \mathcal{J}^{(e)}\boldsymbol{\mathcal{M}}^{\mathcal{T}}. \qquad (5.49)$$

The local derivative integral has a contribution from both direction r, s. In the same way of the 1D discretization, we introduce the differentiation matrices in the r and s directions

$$\boldsymbol{\mathcal{D}}_r = \int_{\mathcal{T}_s} \varphi_j^{\mathcal{T}_s}(r,s)\partial_r\varphi_i^{\mathcal{T}_s}(r,s)drds,$$

$$\boldsymbol{\mathcal{D}}_s = \int_{\mathcal{T}_s} \varphi_j^{\mathcal{T}_s}(r,s)\partial_s\varphi_i^{\mathcal{T}_s}(r,s)drds. \qquad (5.50)$$

We can then define the differentiation matrix in x as the sum of these two contributions

$$\boldsymbol{\mathcal{D}}_x^{(e)} = \mathcal{J}^{(e)}(r_x\boldsymbol{\mathcal{D}}_r + s_x\boldsymbol{\mathcal{D}}_s), \qquad (5.51)$$

where r_x and s_x are geometric weights defined by the mapping between the two domains. In a similar fashion we define the y differentiation matrix as

$$\boldsymbol{\mathcal{D}}_y^{(e)} = \mathcal{J}^{(e)}(r_y\boldsymbol{\mathcal{D}}_r + s_y\boldsymbol{\mathcal{D}}_s). \qquad (5.52)$$

Patching together the element matrices, we can calculate the global mass matrix $\boldsymbol{\mathcal{M}}$ and differentiation matrices $\boldsymbol{\mathcal{D}}_x$ and similarly find the differentation matrix in the y direction $\boldsymbol{\mathcal{D}}_y$.

Divergence and gradient reconstruction

Divergence.   We consider the differential equation in $\Omega = \Omega_i \cup \Omega_j$

$$U + \nabla \cdot \boldsymbol{F}(U) = 0, \qquad (5.53)$$

where $U = U(x,y)$ and $\boldsymbol{F}(U) = [E(U), G(U)]$, E, G two function depending on U, to formulate the discrete divergence operator with the coupling matrices between the different domains. The variational formulation in Ω_i is

$$\int_{\Omega_i} \varphi_i U d\boldsymbol{x} + \int_{\Omega_i} \varphi_i \nabla \cdot \boldsymbol{F}(u)d\boldsymbol{x} + \int_\Gamma \varphi_i(\hat{\boldsymbol{F}}(U) - \boldsymbol{F}^-(U))\hat{\boldsymbol{n}}_s dS = 0, \qquad (5.54)$$

with $\Gamma = \partial\Omega_i \cap \Omega_j$ and $\hat{\boldsymbol{n}}_s = [\hat{n}\hat{t}]^T$ the vector normal to the surface Γ. $\boldsymbol{F}^-(U)$ represents the value of $\boldsymbol{F}(U)$ on the boundary and $\hat{\boldsymbol{F}}(U)$ is a numerical flux term, for simplicity and similarly to the 1D discrete model, has been chosen to be centred flux

$$\hat{\boldsymbol{F}}(U) = \frac{1}{2}(\boldsymbol{F}^+(U) + \boldsymbol{F}^-(U)), \qquad (5.55)$$

such that

$$\llbracket \boldsymbol{F}(U) \rrbracket = \hat{\boldsymbol{F}}(U) - \boldsymbol{F}^-(U). \tag{5.56}$$

If we expand the vector $\boldsymbol{F}(\boldsymbol{U})$ to its components

$$
\int_{\Omega_i} \varphi_i U \, d\boldsymbol{x} + \int_{\Omega} \varphi_i \partial_x E(U) \, d\boldsymbol{x} + \int_{\Omega_i} \varphi_i \partial_y G(U) \, d\boldsymbol{x}
$$
$$
+ \int_{\Gamma} \varphi_i \llbracket E(U) \rrbracket \hat{n} \, dS + \int_{\Gamma} \varphi_i \llbracket G(U) \rrbracket \hat{t} \, dS = 0. \tag{5.57}
$$

Substituting the interpolation of U, $E(U)$ and $G(U)$, the coupling integrals becomes

$$
\int_{\Gamma} \varphi_i \llbracket E(U) \rrbracket \hat{n} \, dS = \frac{1}{2} \int_{\Gamma} \varphi_i (\varphi_j^+ E^+(U) - \varphi_j^- E^-(U)) \hat{n} \, dS,
$$
$$
\int_{\Gamma} \varphi_i \llbracket E(U) \rrbracket \hat{n} \, dS = \frac{1}{2} \int_{\Gamma} \varphi_i (\varphi_j^+ E^+(U) - \varphi_j^- E^-(U)) \hat{n} \, dS. \tag{5.58}
$$

On each border element Ω_e , these integral are line integrals on the edge Γ_k, $k = 1, 2$ or 3 that is shared between domains and we can use the 1D local mass matrix (3.27) to evaluate the integrals

$$
\frac{1}{2} \int_{\Gamma_k} \varphi_i (\varphi_j^+ E^+(U) - \varphi_j^- E^-(U)) \hat{n} \, dS = \frac{1}{2} (\boldsymbol{M}_k^+ E^+(U) - \boldsymbol{M}_k^- E^-(U)) \hat{n}
$$
$$
\frac{1}{2} \int_{\Gamma_k} \varphi_i (\varphi_j^+ G^+(U) - \varphi_j^- G^-(U)) \hat{t} \, dS = \frac{1}{2} (\boldsymbol{M}_k^+ G^+(U) - \boldsymbol{M}_k^- G^-(U)) \hat{t} \tag{5.59}
$$

We define the normal and tangential coupling matrices patching together the local matrices to global ones, that have zeros entry for all the internal nodes and the element of the 1D local mass matrix for the interface nodes

$$
\begin{aligned}
\boldsymbol{\mathcal{C}}_{k-}^{\hat{n}} &= \frac{1}{2} \boldsymbol{M}_k^- \hat{n}_k, \\
\boldsymbol{\mathcal{C}}_{k+}^{\hat{n}} &= \frac{1}{2} \boldsymbol{M}_k^+ \hat{n}_k, \\
\boldsymbol{\mathcal{C}}_{k-}^{\hat{t}} &= \frac{1}{2} \boldsymbol{M}_k^- \hat{t}_k, \\
\boldsymbol{\mathcal{C}}_{k+}^{\hat{t}} &= \frac{1}{2} \boldsymbol{M}_k^+ \hat{t}_k.
\end{aligned}
\tag{5.60}
$$

Note tha for the domain Ω_j, we can deduce the same equations with the normal vector $\hat{m}_s = -\hat{n}_s$. Eq. (5.53) discretized in space becomes

$$\boldsymbol{\mathcal{M}} U + (\boldsymbol{\mathcal{D}}_x + \boldsymbol{\mathcal{C}}_{k-}^{\hat{n}} + \boldsymbol{\mathcal{C}}_{k+}^{\hat{n}}) E(U) + (\boldsymbol{\mathcal{D}}_y + \boldsymbol{\mathcal{C}}_{k-}^{\hat{t}} + \boldsymbol{\mathcal{C}}_{k+}^{\hat{t}}) G(U) = 0. \tag{5.61}$$

Gradient The discrete coupled gradient operator is found in a similar fashion: consider the differential equation

$$U + \nabla F = 0, \tag{5.62}$$

where now $\boldsymbol{U} = [U_1(x, y), U_2(x, y)]$ is a vector and $F = F(x, y)$ a scalar function. We can rewrite eq. (5.62) as

$$
\begin{aligned}
\partial_t U_1 + \partial_x F &= 0 \\
\partial_t U_2 + \partial_y F &= 0
\end{aligned}
\tag{5.63}
$$

Changing to the variational formulation, integrating by parts twice the derivative terms and using the interpolated functions, we can pass to the space discrete formulation

$$\mathcal{M}\partial_t U_1 + (\mathcal{D}_x + \mathcal{C}_{k-}^{\hat{n}} + \mathcal{C}_{k+}^{\hat{n}})F = 0$$
$$\mathcal{M}\partial_t U_2 + (\mathcal{D}_y + \mathcal{C}_{k-}^{\hat{t}} + \mathcal{C}_{k+}^{\hat{t}})F = 0 \tag{5.64}$$

We can define the coupled differentiation matrices

$$\mathcal{Q}_x = \mathcal{D}_x + \mathcal{C}_{k-}^{\hat{n}} + \mathcal{C}_{k+}^{\hat{n}},$$
$$\mathcal{Q}_y = \mathcal{D}_y + \mathcal{C}_{k-}^{\hat{t}} + \mathcal{C}_{k+}^{\hat{t}}. \tag{5.65}$$

and the discrete gradient and divergence operators.

Definition 4. *We define the discrete gradient $\boldsymbol{Q}^G$ and divergence $\boldsymbol{Q}^D$ operators as*

$$\nabla \Rightarrow \mathcal{Q}^G = \begin{bmatrix} \mathcal{Q}_x \\ \mathcal{Q}_y \end{bmatrix}, \quad \nabla \cdot \Rightarrow \mathcal{Q}^D = [\mathcal{Q}_x, \mathcal{Q}_y]. \tag{5.66}$$

Finally, we define the mass matrix for vectorial functions as

$$\underline{\mathcal{M}} = \begin{bmatrix} \mathcal{M} & 0 \\ 0 & \mathcal{M}. \end{bmatrix} \tag{5.67}$$

5.5 2D nonlinear dispersive wave-body discrete model

5.5.1 First order formulation

The numerical resolution of the models is done evaluating the first order derivative formulation. Thus, starting from the eqs. (5.26) and (5.27), we define auxiliary variables such that the free surface model in Ω_f becomes

$$\begin{aligned}
&P_t + g\nabla \cdot \boldsymbol{q} = 0, \\
&\boldsymbol{q}_t + \nabla \cdot (\boldsymbol{q} \otimes \boldsymbol{u}) + d\nabla P = \boldsymbol{H}, && \boldsymbol{x} \in \Omega_f \\
&\boldsymbol{H} = Bh_0^2 \nabla G + \alpha_{MS} h_0^2 d\nabla F, \\
&G - \nabla \cdot \boldsymbol{q}_t = 0, \\
&F - \nabla \cdot \boldsymbol{N} = 0, \\
&\boldsymbol{N} - \nabla P = 0.
\end{aligned} \tag{5.68}$$

Likewise, for the body model

$$\begin{aligned}
&\boldsymbol{q}_t + \nabla \cdot (\boldsymbol{q} \otimes \boldsymbol{u}) + d\nabla P = 0, \\
&-\nabla \cdot \boldsymbol{w} = -a + \nabla \cdot \boldsymbol{k}, && \boldsymbol{x} \in \Omega_b, \\
&\boldsymbol{w} - d\nabla P = 0, \\
&\boldsymbol{k} - \nabla \cdot (\boldsymbol{q} \otimes \boldsymbol{u}) = 0.
\end{aligned} \tag{5.69}$$

Note that the mass equation is not solved explicitly in Ω_b but it acts as a constraint on the position of the body. Moreover the pressure equation solved in the system (5.69), is valid also in the free surface domain and it is automatically sastified.

5.5.2   Variational formulation

The discrete formulation of the model is evaluated passing through the variational formulation. We multiply the eqs. (5.68) and (5.69) by a test function $\varphi_i(\boldsymbol{x})$ and integrate in each subdomain $\Omega_{w,l,b}$. The non conservative products, $d\nabla P$, which are not continuous over the interface between the free surface and body domains, are treated with the same strategy introduced in section 3.3.2. We make use of penalty terms consistent with the local linearization of the quasi-linear form of the system.

In the following equations the integral terms of the kind $\int_\Omega \varphi_i \nabla \cdot (\,)\boldsymbol{dx}$ are represented already after a double integration by part, such that we have the coupling terms on the interfaces. The variational form of the free surface system reads

$$\int_{\Omega_w} \varphi_i P_t \boldsymbol{dx} + g\int_{\Omega_w} \varphi_i \nabla \cdot \boldsymbol{q} \boldsymbol{dx} + g\int_{\Gamma_o} \varphi_i [\![\boldsymbol{q}]\!] \hat{\boldsymbol{n}}_S dS = 0, \tag{5.70a}$$

$$\int_{\Omega_w} \varphi_i \boldsymbol{q}_t \boldsymbol{dx} + \int_{\Omega_w} \varphi_i \nabla \cdot (\boldsymbol{q}\otimes\boldsymbol{u})\, dx + \int_{\Gamma_o} \varphi_i [\![\boldsymbol{q}\otimes\boldsymbol{u}]\!] \hat{\boldsymbol{n}}_S dS$$
$$+ \int_{\Omega_w} \varphi_i d\nabla P \boldsymbol{dx} + \int_{\Gamma_o} \varphi_i \hat{d} [\![P]\!] \hat{\boldsymbol{n}}_S dS = \int_{\Omega_w} \varphi_i \boldsymbol{H} \boldsymbol{dx}, \tag{5.70b}$$

$$\int_{\Omega_w} \varphi_i \boldsymbol{H} dx = B h_0^2 \left(\int_{\Omega_w} \varphi_i \nabla G \boldsymbol{dx} + \int_{\Gamma_o} \varphi_i [\![G]\!] \hat{\boldsymbol{n}}_S dS \right)$$
$$+ \alpha_{MS} h_0^2 \left(\int_{\Omega_w} \varphi_i d\nabla F \boldsymbol{dx} + \int_{\Gamma_o} \varphi_i \hat{d} [\![F]\!] \hat{\boldsymbol{n}}_S dS \right), \tag{5.70c}$$

$$\int_{\Omega_w} \varphi_i G \boldsymbol{dx} - \int_{\Omega_w} \varphi_i \nabla \cdot \boldsymbol{q}_t - \int_{\Gamma_o} \varphi_i [\![\boldsymbol{q}_t]\!] \hat{\boldsymbol{n}}_S dS = 0, \tag{5.70d}$$

$$\int_{\Omega_w} \varphi F - \int_{\Omega_w} \varphi_i \nabla \cdot \boldsymbol{N} \boldsymbol{dx} - \int_{\Gamma_o} \varphi_i [\![\boldsymbol{N}]\!] \hat{\boldsymbol{n}}_S dS = 0, \tag{5.70e}$$

$$\int_{\Omega_w} \varphi_i \boldsymbol{N} \boldsymbol{dx} - \int_{\Omega_w} \varphi_i \nabla P \boldsymbol{dx} - \int_{\Gamma_o} \varphi_i [\![P]\!] \hat{\boldsymbol{n}}_S dS = 0, \tag{5.70f}$$

where we have defined $\hat{\boldsymbol{n}}_S = [\hat{n}_1, \hat{n}_2]^T$ and dS the out pointing normal vector to the surface and the infinitesimal surface, respectively. In the coupling layer, we can do the same consideration as in the 1D case of eq. (3.46). The variational formulation is identical to the one of Ω_w with $(\alpha, B) = (0,0)$ and the jump terms both on the MS-NSW interface Γ_o and on the NSW-body interface Γ_i.

The weak formulation in the body domain is evaluated in the same manner:

$$\int_{\Omega_b} \varphi_i \boldsymbol{q}_t \boldsymbol{dx} + \int_{\Omega_b} \varphi_i \nabla \cdot (\boldsymbol{q}\otimes\boldsymbol{u})\, \boldsymbol{dx} + \int_{\Gamma_i} \varphi_i [\![\boldsymbol{q}\otimes\boldsymbol{u}]\!] \hat{\boldsymbol{n}}_S dS$$
$$+ \int_{\Omega_b} \varphi_i d\nabla P \boldsymbol{dx} + \int_{\Gamma_i} \varphi_i \hat{d} [\![P]\!] \hat{\boldsymbol{n}}_S dS x = 0, \tag{5.71a}$$

$$-\int_{\Omega_b} \varphi_i \nabla \cdot \boldsymbol{w} \boldsymbol{dx} \int_{\Gamma_i} \varphi_i [\![\boldsymbol{w}]\!] \hat{\boldsymbol{n}}_S dS = -\int_{\Omega_b} \varphi_i a \boldsymbol{dx}$$
$$+ \int_{\Omega_b} \varphi_i \nabla \cdot \boldsymbol{k} \boldsymbol{dx} + \int_{\Gamma_i} \varphi_i [\![\boldsymbol{k}]\!] \hat{\boldsymbol{n}}_S dS, \tag{5.71b}$$

$$\int_{\Omega_b} \varphi_i \boldsymbol{w} \boldsymbol{dx} - \int_{\Omega_b} \varphi_i d\nabla P \boldsymbol{dx} - \int_{\Gamma_i} \varphi_i \hat{d} [\![P]\!] \hat{\boldsymbol{n}}_S dS = 0, \tag{5.71c}$$

$$\int_{\Omega_b} \varphi_i \boldsymbol{k} \boldsymbol{dx} - \int_{\Omega_b} \varphi_i \nabla \cdot (\boldsymbol{q}\otimes\boldsymbol{u})\, \boldsymbol{dx} - \int_{\Gamma_i} \varphi_i [\![\boldsymbol{q}\otimes\boldsymbol{u}]\!] \hat{\boldsymbol{n}}_S dS = 0. \tag{5.71d}$$

Proposition 6. *The variational formulations eqs. (5.70) and (5.71) are exactly well balanced: the hydrostatic equilibrium in definition 3 is an exact solution of the weak form.*

Proof. The proof is identical to the 1D case in proposition 2. □

5.5.3 Space discrete formulation

Moreover, as for the one dimensional discrete formulation, the matrix $\widetilde{\boldsymbol{Q}}^G$ represents the derivation matrices dependent on the elevation d, resulting from

$$\widetilde{\boldsymbol{\mathcal{Q}}}_e^G = \int_{\Omega_e} \varphi_i d \nabla P d\boldsymbol{x} + \int_{\Gamma_e} \varphi_i \hat{d}_{e,e^+} [\![P]\!] \hat{\boldsymbol{n}}_s dS. \tag{5.72}$$

Using the definition 4, the continuous eqs. (5.68) and (5.69) in space discrete formulation are:

$$\boldsymbol{\mathcal{M}}_{w,l} P_t + \boldsymbol{\mathcal{Q}}_{w,l}^D \boldsymbol{q} = 0, \qquad\qquad \boldsymbol{x} \in \Omega_f, \tag{5.73a}$$

$$\boldsymbol{L}_B \boldsymbol{q}_t + \boldsymbol{\mathcal{Q}}_w^D (\boldsymbol{q} \otimes \boldsymbol{u}) + \boldsymbol{B}_d^\alpha P = 0, \qquad\qquad \boldsymbol{x} \in \Omega_w, \tag{5.73b}$$

$$\underline{\boldsymbol{\mathcal{M}}}_{b,l} \boldsymbol{q}_t + \boldsymbol{\mathcal{Q}}_{q,l}^D (\boldsymbol{q} \otimes \boldsymbol{u}) + \widetilde{\boldsymbol{\mathcal{Q}}}_{b,l}^G P = 0, \qquad x \in \Omega_b \cup \Omega_l, \tag{5.73c}$$

$$\boldsymbol{\mathcal{Q}}_b^D \underline{\boldsymbol{\mathcal{M}}}_b^{-1} \widetilde{\boldsymbol{\mathcal{Q}}}_b^G P = -\boldsymbol{\mathcal{M}} 1 a - \boldsymbol{\mathcal{Q}}_b^D \underline{\boldsymbol{\mathcal{M}}}_b^{-1} \boldsymbol{\mathcal{Q}}_b^D (\boldsymbol{q} \otimes \boldsymbol{u}), \qquad x \in \Omega_b. \tag{5.73d}$$

The 2D MS linear operators in matrix formulation are

$$\boldsymbol{L}_B = \underline{\boldsymbol{\mathcal{M}}}_w - Bh_0^2 \boldsymbol{\mathcal{Q}}_w^G \boldsymbol{\mathcal{M}}_w^{-1} \boldsymbol{\mathcal{Q}}_w^D, \quad \boldsymbol{B}_d^\alpha = \widetilde{\boldsymbol{\mathcal{Q}}}_w^G + \alpha_{MS} \widetilde{\boldsymbol{\mathcal{Q}}}_w^G \boldsymbol{\mathcal{M}}_w^{-1} \boldsymbol{Q}_w^D \underline{\boldsymbol{\mathcal{M}}}_w^{-1} \boldsymbol{Q}_w^G \tag{5.74}$$

Proposition 7. *The discrete formulations eqs. (5.73) are exactly well balanced: the hydrostatic equilibrium in definition 3 is an exact solution of the discrete form.*

Proof. The proof is identical to the 1D case in proposition 2. □

5.6 Added mass issues

Following the scheme introduced for the one dimensional model, the vertical acceleration of the body can be evaluated from the Newton's second law. The discrete formulation of the acceleration equation is

$$m_b a = -g m_b + \rho_w \boldsymbol{w}^T \Pi_b. \tag{5.75}$$

Using the Gauss-Lobatto-Legendre integration weights $\boldsymbol{w}^T$, we can prove the following proposition.

Proposition 8. *Provided that the discrete operator $\widetilde{\mathcal{K}}_b$ is invertible, the discrete formulation of eq. (5.24) is*

$$(m_b + \boldsymbol{\mathcal{M}}_{add}) a^{n+1} = -g m_b - g \rho_w \boldsymbol{w}^T d_b - \rho_w \boldsymbol{w}^T \widetilde{\mathcal{K}}_b^{-1} \left(\boldsymbol{Q}_b \boldsymbol{M}_b^{-1} \boldsymbol{Q}_b (\boldsymbol{q} \otimes \boldsymbol{u}) + \widetilde{\boldsymbol{\mathcal{G}}}_f P_f \right). \tag{5.76}$$

where the discrete added mass is defined as

$$\boldsymbol{\mathcal{M}}_{add} = \rho_w \boldsymbol{w}^T \widetilde{\mathcal{K}}_b^{-1} \boldsymbol{w}, \tag{5.77}$$

and the matrices discrete operators $\widetilde{\mathcal{K}}_b$ and $\widetilde{\mathcal{G}}_f$ are

$$
\begin{aligned}
\widetilde{\mathcal{K}}_b &= \left(\mathcal{D}_x^b + \mathcal{C}_b^{\hat{n}} \right) M_b^{-1} \left(\mathcal{D}_x^b + \mathcal{C}_b^{\hat{n}} \right) + \left(\mathcal{D}_y^b + \mathcal{C}_b^{\hat{t}} \right) M_b^{-1} \left(\mathcal{D}_y^b + \mathcal{C}_b^{\hat{t}} \right), \\
&\quad + \mathcal{C}_{bf}^{\hat{n}} M_f^{-1} \mathcal{C}_{fb}^{\hat{n}} + \mathcal{C}_{bf}^{\hat{t}} M_f^{-1} \mathcal{C}_{fb}^{\hat{t}} \\
\widetilde{\mathcal{G}}_f &= \left(\mathcal{D}_x^b + \mathcal{C}_b^{\hat{n}} \right) M_b^{-1} \mathcal{C}_{bf}^{\hat{n}} + \left(\mathcal{D}_y^b + \mathcal{C}_b^{\hat{t}} \right) M_b^{-1} \mathcal{C}_{bf}^{\hat{t}} \\
&\quad + \mathcal{C}_{bf}^{\hat{n}} M_f^{-1} \left(\mathcal{D}_x^f + \mathcal{C}_f^{\hat{n}} \right) + \mathcal{C}_{bf}^{\hat{t}} M_f^{-1} \left(\mathcal{D}_y^f + \mathcal{C}_f^{\hat{t}} \right).
\end{aligned}
\tag{5.78}
$$

Proof. The proof is identical to the 1D case in proposition 4. $\square$

A particular care has to be taken when solving in time the acceleration eq. (5.76). In fact it can be shown that using an explicit method to solve in time the acceleration equation can impact the value of the added mass and if $m_b < \mathcal{M}_{add}$ the algorithm is unconditionally unstable [30]. A better choice is to implement an implicit solver, as the one proposed by Causin et al. [30] for fluid structure interaction, since it would be stable for every Δt and it will converge even for $\mathcal{M}_{add} \gg m_b$.

Chapter 6

2D numerical results

The 2D 'unified' spectral/*hp* Boussinesq model as been tested numerically. In this chapter we are going to present the convergence of the model in case of free surface, coupling NSW and MS domains in chapter 6.1. Subsequently the pontoon test case is shown for a rectangular and a cylinder fixed structure: the results on the study cases presented in chapter 6.2 are shown and compared to reference (CFD and FNPF) solutions to validate model.

6.1 Coupling multiple domains

The convergence of the free surface model is tested through the use of the manufactured solution technique (cfr. section 2.6.4). We consider a squared free surface Ω_O domain of dimension $(x,y) = [-2,2] \times [-2,2]\, m$, with a smaller circular subdomain Ω_I of radius $r = 0.1\, m$ and centered in $(x,y) = (0,0)$. The domain is discretized with a nonstructured triangular mesh as in figure 6.1(a). We impose the following manufactured solution

$$
\begin{aligned}
d(x,y,t) &= A\sin(kx - ct) + h0, \\
u(x,y,t) &= [cd(x,y,t),0]^T, \quad (x,y) \in \Omega_O \cup \Omega_I \\
q(x,y,t) &= d(x,y,t)u(x,y,t).
\end{aligned}
\tag{6.1}
$$

where $h_0 = 1m$ is the water depth and $A = 0.01\, m$ the elevation of the sinusoidal wave, presented in figure 6.1(b).
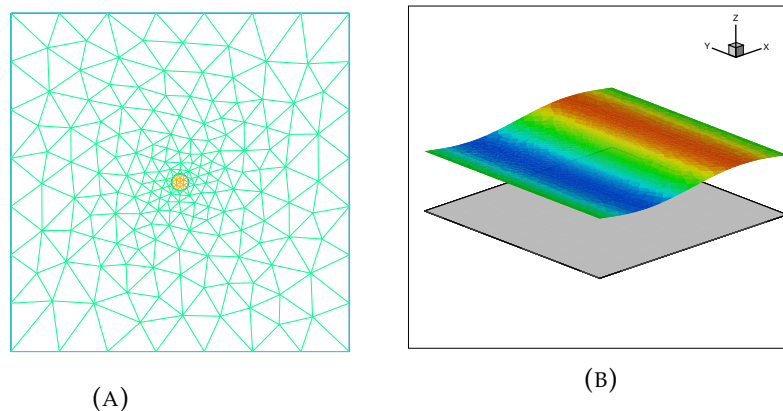

(A)

(B)

FIGURE 6.1 – Mesh (a) and initial solution (b) of the NSW coupled convergence test.

For simplicity, the wave speed is set to be equal to $c = 1\, m/s$ and the wave number $k = \pi$, such that in $\Omega_O \cup \Omega_I$, we have one wave length. The two domains
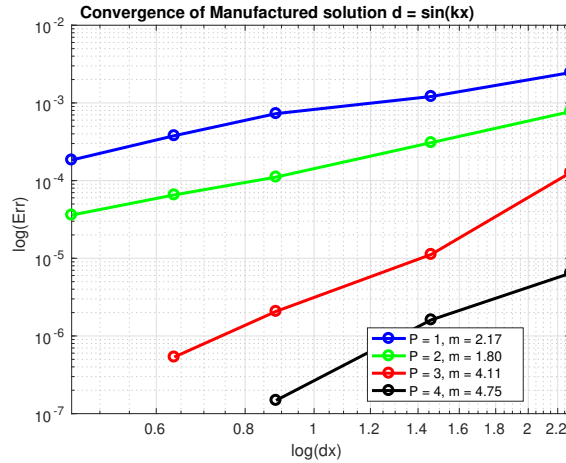
FIGURE 6.2 – Convergence plot for the manufactured solution in eq. (6.1) solved in two NSW free surface domain.

are coupled with centered fluxes and periodical condition is imposed on the vertical boundaries $(x, y) = (-2, y) \cup (2, y)$. The horizontal boundary has reflective wall conditions. As first test, we solve in both domain the NSW system. As we can see from figure 6.2, even though we do not reach the ideal rate of convergence of $P + 1$ for integration method of order P, the model converges approximately with $P + 1$ rate for odd order methods and P for even order, as we have experienced for the 1D wave models.

6.2 Pontoon

We do not have any analytical or experimental solutions for the test cases of the interaction between a solitary wave and a fixed floating pontoon. We have thus evaluated some reference solutions using FNPF and CFD models. First we have tested a linear solitary wave, using the same solitary wave solution (2.141) of section 2.5.2:

$$
\begin{cases}
d(x, y, t) = h_0 + A \operatorname{sech}^2(k(x - x_0 - ct)), \\
\boldsymbol{u}(x, y, t) = c \left(1 - \frac{h_0}{d(x,t)} \right), \\
\boldsymbol{q}(x, y, t) = d(x, y, t) \boldsymbol{u}(x, y, t), \\
k = \gamma \frac{\sqrt{2A}}{2h_0 \sqrt{h_0 + A}}, \quad c = \sqrt{g(A + h_0)},
\end{cases}
\tag{6.2}
$$

for a wave of amplitude $A = 0.01m$ over a depth of $h_0 = 1m$. In this test both the body domain and the outer domain are solved with the NSW equation. The flume is $240\,m$ long and $4\,m$ wide, with a constant depth of $1\,m$. The pontoon is placed with its center at $(x, y) = (0, 0)$. We have tested two pontoons: a rectangular prism and a cylinder with a draft of 0.4. The full description of the two pontoons is in appendix A. In figures 6.3 and 6.4 we see the solitary wave interacting with the pontoons.

We have placed two gauges at $(x, y) = (-31.5, 0)$ and $(x, y) = (26.5, 0)$, upstream and downstream the pontoon. The results of the gauges, in figure 6.5, show that the NSW model underestimates the reflected wave compared to the FNPF and CFD simulations, for both the rectangular and cylinder pontoons. However the transmitted wave is well described.
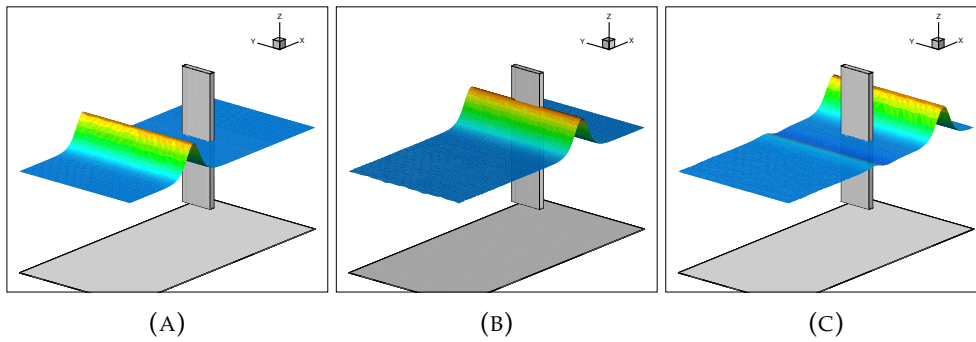
FIGURE 6.3 – Rectangular pontoon NSW test ad different timesteps: figure (a) is the initial condition, figure (b) shows the moment of maximum interaction between the pontoon and the wave and figure (c) after the wave has passed.
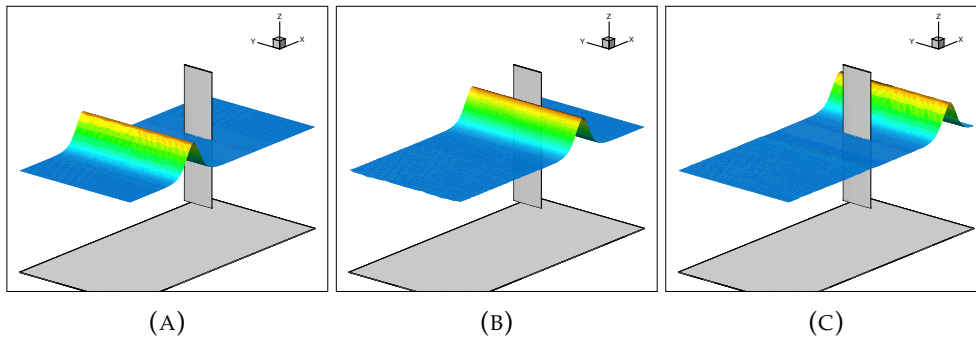

FIGURE 6.4 – Cylinder pontoon NSW test ad different timesteps: figure (a) is the initial condition, figure (b) shows the moment of maximum interaction between the pontoon and the wave and figure (c) after the wave has passed.
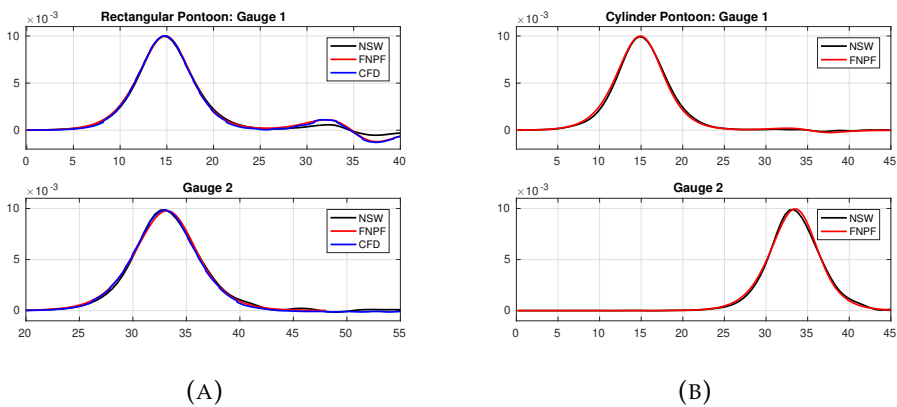

FIGURE 6.5 – NSW gauges results for the rectangular pontoon (a) and the cylinder pontoon (b).

Chapter 7

Latching control

In this chapter, we present the latching control technique: the principle regulating the latching control and its implementation are described in section 7.1, while section 7.2 shows proof-of-concept results of the application of this control technique to the heaving box case.

7.1 Latching control

7.1.1 Principle

The reason in implementing a control technique of the body's movement is to improve the production of energy. Budal and Falnes have shown in [24] that the power production of point absorber WEC is increased when the device is kept in phase with the incoming wave period. This can be accomplished with a simple phase control that consists in latching the motion of the body when its vertical velocity is equal to zero, at the peak and trough of each oscillations, and then releasing it after a latching period, obtaining an higher vertical speed. The complexity of the latching control lies in the determination of the latching time. It has been shown that latching period and the body response are sub-optimal for linear code compared to CFD [76]. Moreover, small heaving devices in long wave might present overly large oscillation, breaking the hydrodynamic assumption of small amplitude [82]. Thus, it is interesting to test the performance of Boussinesq models for which we do not have such assumption. Several studies considered the evaluation of the latching period T_L, in regular waves it has been shown that half the difference between the wave and the natural period of the body is a good estimate of T_L [67] and in [82]. Greenhow and White [82] did a theoretical study and demonstrate that, whitin the small amplitude assumption, the response of a latched body is three times the wave amplitude. In random sea state, different techniques have been proposed [11] to find an optimal latching time. For example Budal et al. [25] has experimented with Kalman filter, placed before the body, to detect the instantaneus period and regulate the latching time accordingly. Other approaches involves the improvement of a specific target characteristic, as the power absorption [10] or the velocity and excitation peaks [89].

In this work, we consider monochromatic and regular waves with a period of T and we know the natural period of the body T_b. Hence, we consider a constant
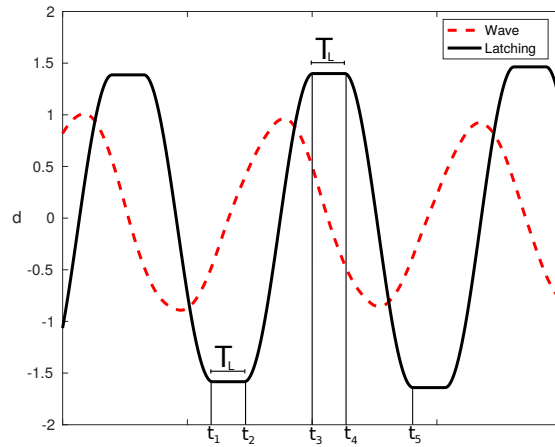
FIGURE 7.1 – Latching timings to put position and elevation in phase: T_L is the latching period, t_1, t_3 and t_5 are the starting latching instants, at t_2 and t_3 the body is unlatched.

latching period T_L, that is evaluated by:

$$T_L = \frac{t_5 - t_1}{2} - t_5 - t_4 = \frac{T - T_b}{2},\qquad(7.1)$$

referring to the figure 7.1. Note that eq. (7.1) presents several limitation. First of all it can be used only for wave with a period $T > T_b$. With respect to wave period $T < T_b$, other methods had been developed, i.e. declutching [173]. Secondly, the body must have no or negligible damping and the natural period of the body can be complicated to define, especially in case of large motions and high nonlinearities. Finally, the latching period can be defined differently for the peak and the trough of the wave, to better follow the characteristic profile of the wave. However, the following tests had been designed with linear waves and an undamped body, such that eq. (7.1) is valid.

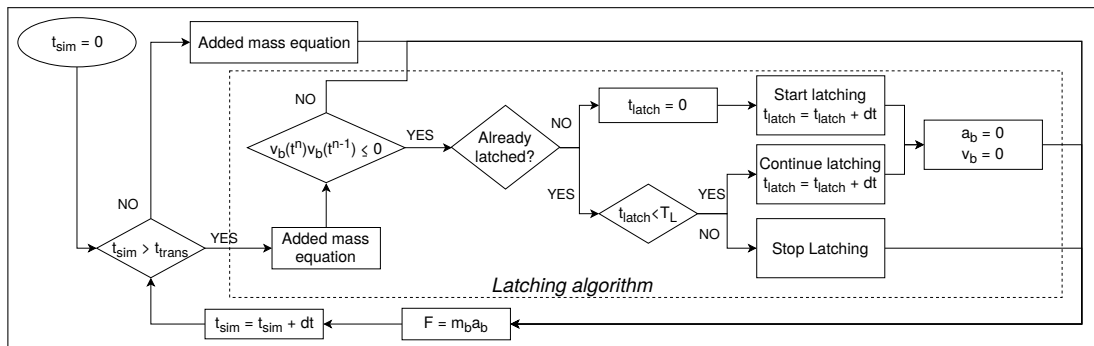### 7.1.2 Implementation

FIGURE 7.2 – Latching algorithm: t_{sim} is the instant time of the simulation, t_{trans} is the transitional time to reach the steady solution, t_{latch} is the latching instant time, T_L the latching period, Δt the timestep. m_b, v_b, a_b are respectively the mass, the velocity and the acceleration of the body. F is the force applied to the body.

The latching algorithm proposed for constant T_L is designed on the one presented by Giorgi and Ringwood [76] for bodies in linear waves. The basic algorithm is shown in the flowchart 7.2. At $t_{sim} = 0$, the body is considered at the equilibrium position and water flume is still. The waves are generated gradually to reach the final elevation. During this transitional time t_{trans} the latching is not applied, letting the waves and the body reach a steady state. At every timestep Δt, we evaluate the acceleration of the body thanks to the added mass eq.(2.132). The latching starts when the $v_b(t^n) = 0$ condition is satisfied. Due to the numerical precision and timestepping, it is really unlikely to verify exactly the latching condition, a better strategy is to check when the velocity changes direction, thus when $v_b(t^n)v_b(t^{n-1}) \leq 0$, we have crossed an extremum and the latching is applied. The condition is verified also when the body is already latched, so a timer t_{latch} has been set to count how long the body has been locked in the extreme position and at every new iteration t_{latch} is increased of Δt. Once $t_{latch} \geq T_L$, the body is released from the locked state. If the latching condition is verified and $t_{latch} < T_L$, the acceleration and velocity of the body are set to zero, such that the position of the center of gravity of the body $z_{cog}(t^n) = z_{cog}(t^{n-1})$, while if one of the conditions is not verified $v_b(t^n)$ and $a_b(t^n)$ are updated and the dynamics of the body is left free to evolve.

7.2 Results

7.2.1 1D
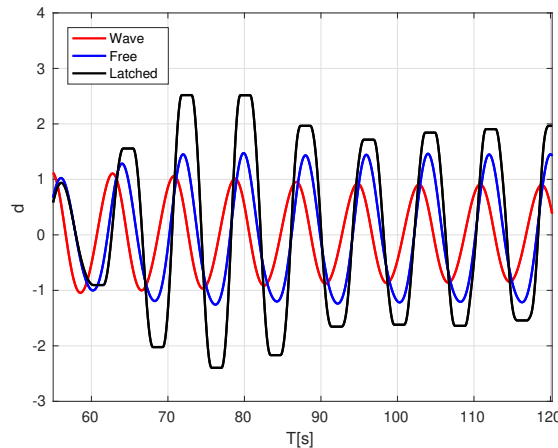
FIGURE 7.3 – Comparison between the amplitude of the incoming wave, the free and latched body dynamics, respectively in red, blue and black.

We have applied the latching algorithm 7.2 to the case of a heaving box with a width of $6m$ and draft $5m$ in a water depth of $20m$. The incoming waves can be regarded as linear ($H = 2.23m$) with a period of $8s$, which is well outside the box's heave natural frequency of $5.5s$. The results is seen in figure 7.3, where the latching have been activated at $t = 40s$. First we see that the latching, as expected, greatly increases the motion response of the box. The non-latched solution has a response amplitude operator (RAO) of roughly 1.2. The latched case in figure 7.3, albeit the heave amplitude is not constant in time, clearly has a RAO above 2. We see some differences between the Boussinesq and the CFD results, mainly in phase, but again the Boussinesq model correctly captures the salient features of the solution. The

latched response is not perfectly harmonic due to reflected waves and even some air entrainment (in the CFD case).

(A)   (B)
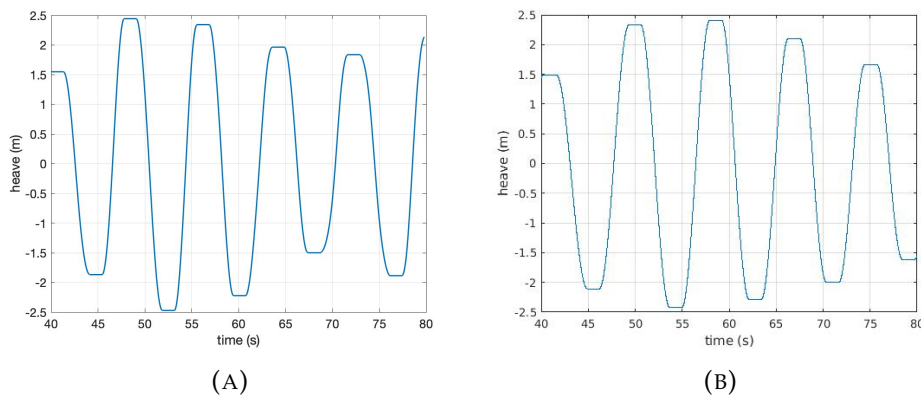
FIGURE 7.4 – Latched heave motion using (a) the Boussinesq model and (b) VOF-RANS.

This simple control method is beneficial although not optimal also in semi-random sea state. As an example, the same linear incoming wave has been applied to a multiple body case, in figure 7.5(a), where the body in the left is a fixed pontoon and right one is a floating one. While the incoming wave is a monochromatic one, the waves interacting with the latched body are the result of transmitted and reflected waves and can be considered random. As we can see from the figure 7.5(b), the oscillations of the body latched are again, about twice the amplitude of the incoming wav, compared to 1.5 times of the free floating body.

(A)   (B)

FIGURE 7.5 – Figure (a) shows the initial set of the multiple bodies case and figure (b) the motion of the center of gravity of second body for the free heaving and latched cases.

Chapter 8

Conclusion and follow up

This thesis proposes a novel method to solve the interaction between waves and floating bodies in the region of shallow waters, based on weakly dispersive, weakly nonlinear Boussinesq equations. This st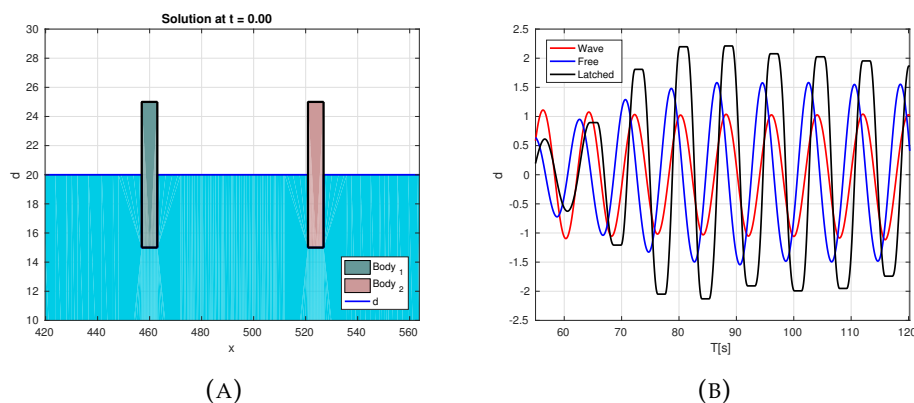udy is addressed in particular to the marine and renewable energy sector, within the design and simulation of heaving point absorber wave energy converters. In this final chapter, we recall the contributions and the results and we propose some possible follow-up topics.

8.1 Wave-body interaction

We have proposed a depth-integrated unified Boussinesq model for nonlinear wave-body interaction based on the unified approach [96, 111, 78] which instructs to divide the computational domain in free surface and body domain and express the body dynamics by a depth-integrated Boussinesq model too. We have presented the derivation of three classical nonlinear Boussinesq models (nonlinear shallow water, Abbott model [2] and Madsen and Sørensen [124]) for the description of the water waves dynamics in the free surface area. The similar deductions had been used to obtain the depth integrated model in the body domain and the differential equations that define the dynamics of the body. as all models based on Boussinesq-type equations, the model is limited to shallow and intermediate depth regimes.

The wave-body interaction model has been resolved with the spectral/*hp* finite element method (SEM). In particular, we have discussed the construction of continuous SEM [99] and used them to solve the models inside each domain. The discontinuous Galerkin SEM [37] had been considered and applied to implement flux-based coupling conditions and permit the exchange of informations between domains.

This results in a new efficient and accurate model that simulates the wave propagation and the nonlinear interaction of waves with bodies. We have tested our framework both for a one horizontal dimension and two dimensions model. We have demonstrated the high order convergence of the models using manufactured solutions in case of the coupling between free surface domains and wave-body interactions. Moreover, for the one dimensional case, we have verified the hydrostatic model for a body in forced motion and decay motion, using the exact and semi-analytical solution obtained by Lannes [111]. The 1D results for a fixed pontoon test and a freely floating body have been evaluated using the dispersive MS model and have shown a good agreement with the results of FNPF and CFD models and in general an improvement in precision compared to linear models. The 2D model, after being validated with the manufactured solution, has been used to simulate the pontoon that shows good agreement with the FNPF and CFD simulations too. Finally we have implemented the latching algorithm as outlined in Giorgi and Ringwood [76] to improve the response to the wave motion of the body and apply it to the case

of a heaving box. The preliminary results show that the Boussinesq model captures the salient features of the solution shown by the CFD computations, even if they presents some differences.

8.2   Future developements

The results obtained in this thesis open several research topics, including issues to be solved and not yet addressed in this work or future developments that will fully exploit the depth-integrated SEM model introduced.

8.2.1   Stabilization

The first important aspect to address is the implementation a pressure stabilization technique to eliminate the spurious modes resulting from the discretization that influence the precision of the results. It can be demonstrated that the use of only first order operators with centered fluxes results in spurious oscillations in the solution [129]. On the other hand, undivided even order operators have a damping effect on the high frequency oscillations. Notice that these modes had a minimal impact on the results of our tests. Nonetheless, a countermeasure should be implemented to completely avoid them, in the view of simulating more complex cases. We propose two methods:

Fast stabilization technique   Consider the inner domain eqs. (2.131). A simple stabilization technique consists in adding a numerical "velocity" v_s to the mass equation (2.131a):

$$d_t + q_x = -v_s, \quad \dot{v}_s = \mu_E P. \tag{8.1}$$

The velocity v_s is a perturbation of the mass of the order of the scheme $\mathcal{O}(\Delta x^{p+1})$. The rest of the derivation of the wave-body model repeats the one presented in chapters 2 and 5.

This stabilization permits to insert easily into the present model a new term that should absorb part of the spurious oscillations.

Dissipation operator stabilization technique   The second idea is to add to the model a dissipation operator based on the standard continuous Galerkin stiffness matrix. The main principle is that the continuous second order derivative operator, without the coupling conditions, can absorb the energy of the unresolved modes [129]. We suggest a rough implementation of this stabilization method. Consider the 1D NSW wave-body model

$$V_t + \boldsymbol{J}_a W_x + N = 0,$$

where $V = [d; q]^T$, $W = [P, q]^T$ and $N = [0; (qu)_x]^T$ is the vector of nonlinear terms. The matrix $\boldsymbol{J}_a = \begin{bmatrix} 0 & g \\ gd & 0 \end{bmatrix}$ is the linear acoustic Jacobian. The stabilization in the continuous model requires to add the stabilizing term $\mathcal{S} = (\boldsymbol{\tau} \boldsymbol{J}_a (V_t + \boldsymbol{J}_a W_x + N))_x$ to the model and discretize it using only the standard continuous matrices. The main drawback of this technique is that the numerical resolution is more computational demanding, as the stabilizing term couples the mass and momentum equations and a global (mass and momentum) matrix has to be inverted at every timestep. Since the numerical results, in chapter 4, were minimally affected by the spurious modes

and the decrease in computational power is non negligible, we have decided to leave the stabilization to future development.

8.2.2 Domain coupling

Another point of interest is the coupling between the different domains, not only inner and outer but also MS-NSW coupling. As introduced in the previous chapter, we have chosen a coupling strategy that conserves the total water mass of the global domain. However, a method that conserves the total energy could be another sensible choice. This would mean to use non standard Boussinesq models. In particular the MS model has to be modified adding a new nonlinear term to become Galilean invariant, as

$$
\begin{aligned}
d_t + q_x &= 0, \\
\mathcal{L}_B(q_t + (uq)_x) + \mathcal{B}_d^\alpha P &= 0.
\end{aligned}
\tag{8.2}
$$

This new term is within the MS approximation and it does not affect the precision of the model. Moreover, it can be shown that the invariant MS (iMS) model (8.2) conserves the energy.

The inclusion of a energy conserving model is going to be necessary in the implementation of an arbitrary Lagrangian Eulerian model and permitting more degree of freedom to the model. In this thesis, since we have only considered vertical movement and the results found were acceptable, we have not implemented a energy conservative model.

8.2.3 Body movements

The natural continuation of this work is the inclusion of more degree of freedom to the body, in particular rotations (pitch or yaw) and horizontal translations (surge and sway). A critical element when we consider sway and surge motions is to keep track of the contact point between water and body as it defines the boundary between the free surface and the body lateral surface. The position of the contact point can be accounted using some tracking techniques as the one developed by Godlewski et al. [78] for congested shallow water flow and adapt the roof model to a moving body. This will permit to describe not only the position of the contact point between water and body on rotating body but also along bodies which walls are not vertical at the contact point. The approach for the description of horizontal translation is to have water-body interfaces that are time dependent and move accordingly to the body motion. This can be done setting up the problem in a arbitrary Lagrangian Eulerian framework (ALE): we can define two coordinate systems, the fixed earthbound or Eulerian one and one with the origin framed to the center of the body, called Lagrangian. Through a mapping between the two coordinates systems, we can pass between the far field (in Eulerian coordinates) or the moving fields (body and near field) in Lagrangian coordinates where the horizontal motion is described as a motion of the whole system and the interfaces can be considered as fixed.

8.2.4 Applications

The final aspiration of this work is to bridge these fundamental developments to applications of engineering relevance. This can be achieved not only by using control techniques (as the latching previously presented) but also adding a power take off and damping device to the body, such that the power generated by the device can

be evaluated and compared to physical experiments. Moreover, we have seen that is simple to expand the model to simulate multiple bodies, such that farms and arrays of WEC, as the one presented in [47], can be numerically resolved. Finally, the ability to simulate multiple bodies in an precise and efficient way will permit optimization studies, which can not be performed by CFD because of the high computational cost.

Appendix A

2D test settings

We report here the setting of the 2D test for the pontoon, forced motion and free floating cases.

Rectangular pontoon
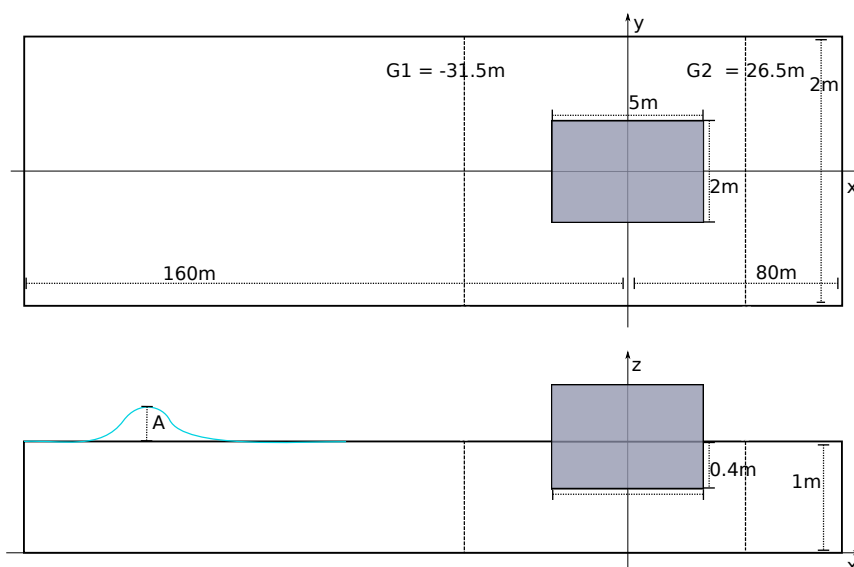
— Flume setting:
  Length: $L = 240m$ $(x_-, x_+) = (-180m, 80m),$
  Width: $W = 2m$ $(y_-, y_+) = (-1m, 1m),$
  Depth: $h_0 = 1m,$
  Gauge 1: $x_{G1} = (-31.5m)\,,$
  Gauge 2: $x_{G2} = (26.5m).$
— Pontoon setting
  Length: $L = 5m,$ $(x_-, x_+) = (-2.5m, 2.5m),$
  Width: $W = 1m,$ $(y_-, y_+) = (-0.5m, 0.5m),$
  Draft: $h_{draft} = 0.4m.$

Cylinder pontoon
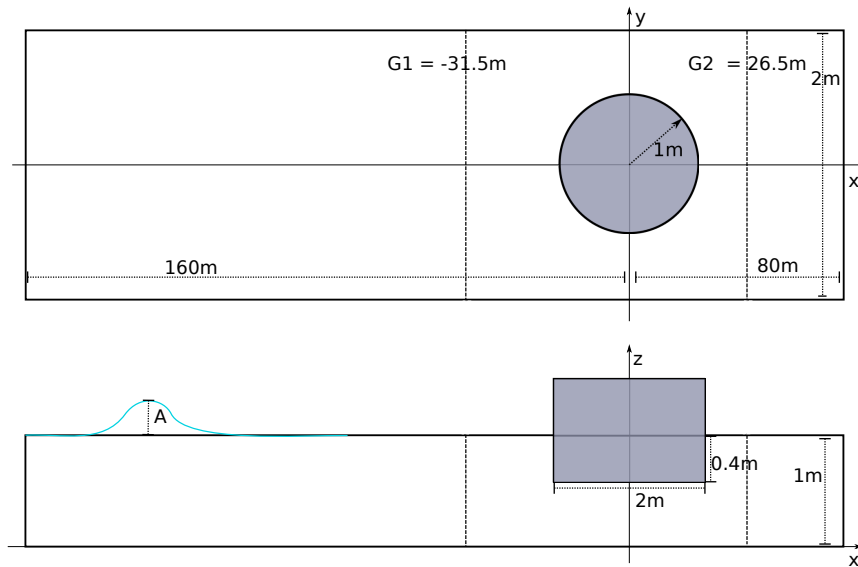
— Flume setting:

Length:	$L = 240m$	$(x_-, x_+) = (-180m, 80m)$,
Width:	$W = 2m$	$(y_-, y_+) = (-1m, 1m)$,
Depth:	$h_0 = 1m$,	
Gauge 1:	$x_{G1} = (-31.5m)$,	
Gauge 2:	$x_{G2} = (26.5m)$.	

— Pontoon setting

Radius:	$R = 1m$,
Draft:	$h_{draft} = 0.4m$.

Bibliography

[1] J. Abanades, D. Greaves, and G. Iglesias. "Wave farm impact on the beach profile: A case study". In: *Coastal Engineering* 86 (2014), pp. 36–44.

[2] M.B. Abbott, H.M. Petersen, and O. Skovgaard. "On the numerical modelling of short waves in shallow water". In: *Journal of Hydraulic Research* 16.3 (1978), pp. 173–204.

[3] R. Abgrall. "On essentially non-oscillatory schemes on unstructured meshes: analysis and implementation". In: *Journal of Computational Physics* 114.1 (1994), pp. 45–58.

[4] Paris Agreement. "United nations framework convention on climate change". In: *Paris, France* (2015).

[5] K. Anastasiou and C.T. Chan. "Solution of the 2D shallow water equations using the finite volume method on unstructured triangular meshes". In: *International Journal for Numerical Methods in Fluids* 24.11 (1997), pp. 1225–1245.

[6] *ANSYS-AQWA*. URL: https://www.ansys.com/.

[7] *Aquamarine Power*. URL: http://www.emec.org.uk/about-us/wave-clients/aquamarine-power/.

[8] A. Babarit. "Impact of long separating distances on the energy production of two interacting wave energy converters". In: *Ocean Engineering* 37.8-9 (2010), pp. 718–729.

[9] A. Babarit. *NEMOH*. URL: https://lheea.ec-nantes.fr/logiciels-et-brevets/nemoh-presentation-192863.kjsp.

[10] A. Babarit and A. H. Clément. "Optimal latching control of a wave energy device in regular and irregular waves". In: *Applied Ocean Research* 28.2 (2006), pp. 77–91.

[11] A. Babarit, G. Duclos, and A. H. Clément. "Comparison of latching control strategies for a heaving wave energy device in random sea". In: *Applied Ocean Research* 26.5 (2004), pp. 227–238.

[12] I. Babuška and M. R. Dorr. "Error estimates for the combinedh andp versions of the finite element method". In: *Numerische Mathematik* 37.2 (1981), pp. 257–277.

[13] I. Babuška and B.Q. Guo. "The h, p and hp version of the finite element method; basis theory and applications". In: *Advances in Engineering Software* 15.3-4 (1992), pp. 159–174.

[14] I. Babuška, B. A. Szabo, and I. N. Katz. "The p-version of the finite element method". In: *SIAM journal on numerical analysis* 18.3 (1981), pp. 515–545.

[15] S. J. Beatty. "Self-reacting point absorber wave energy converters". PhD thesis. 2015.

[16]   K.A. Belibassakis. "A boundary element method for the hydrodynamic analysis of floating bodies in variable bathymetry regions". In: *Engineering Analysis with Boundary Elements* 32.10 (2008), pp. 796–810.

[17]   D. Bellafiore et al. "Modeling ship-induced waves in shallow water systems: The Venice experiment". In: *Ocean Engineering* 155 (2018), pp. 227–239.

[18]   S. Bellec, M. Colin, et al. "On the existence of solitary waves for Boussinesq type equations and Cauchy problem for a new conservative model". In: *Advances in Differential Equations* 21.9/10 (2016), pp. 945–976.

[19]   P. Bonneton et al. "A splitting approach for the fully nonlinear and weakly dispersive Green–Naghdi model". In: *Journal of Computational Physics* 230.4 (2011), pp. 1479–1498.

[20]   U. Bosi et al. "A spectral/hp element depth-integrated model for nonlinear wave-body interaction". In: *Computer Methods in Applied Mechanics and Engineering* 348 (2019), pp. 222–249.

[21]   C. A. Brebbia. *Topics in Boundary Element Research: Volume 1: Basic Principles and Applications*. Vol. 1. Springer, 2013.

[22]   D. Bresch, D. Lannes, and G. Metivier. "Waves interacting with a partially immersed obstacle in the Boussinesq regime". In: *arXiv preprint arXiv:1902.04837* (2019).

[23]   M. Brocchini. "A reasoned overview on Boussinesq-type models: the interplay between physics, mathematics and numerics". In: *Proceedings of the Royal Society A: Mathematical, Physical and Engineering Sciences* 469.2160 (2013), p. 20130496.

[24]   K. Budal and J. Falnes. "Interacting point absorbers with controlled motion". In: *Power from sea waves* (1980), pp. 381–399.

[25]   K. Budal et al. "The Norwegian wave-power buoy project". In: *Norges teknisk-naturvitenskapelige universitet, Fakultet for naturvitenskap . . .* (1982).

[26]   K. Budar and J. Falnes. "A resonant point absorber of ocean-wave power". In: *Nature* 256.5517 (1975), p. 478.

[27]   R. Caljouw et al. "Testing and model evaluation of a scale CETO unit. towards the deployment of a commercial scale CETO Wave Energy Converter". In: *Proceedings of the 9th European wave and tidal energy conference (EWTEC)*. 2011.

[28]   C. D. Cantwell et al. "High-order spectral/hp element discretisation for reaction–diffusion problems on surfaces: Application to cardiac electrophysiology". In: *Journal of computational physics* 257 (2014), pp. 813–829.

[29]   M. J. Castro et al. "Why many theories of shock waves are necessary: Convergence error in formally path-consistent schemes". In: *Journal of Computational Physics* 227.17 (2008), pp. 8107–8129.

[30]   P. Causin, J.-F. Gerbeau, and F. Nobile. "Added-mass effect in the design of partitioned algorithms for fluid–structure problems". In: *Computer methods in applied mechanics and engineering* 194.42-44 (2005), pp. 4506–4527.

[31]   C. Chen, H. Liu, and R. C. Beardsley. "An unstructured grid, finite-volume, three-dimensional, primitive equations ocean model: application to coastal ocean and estuaries". In: *Journal of atmospheric and oceanic technology* 20.1 (2003), pp. 159–186.

[32]   J.-T. Chen et al. "True and spurious eigensolutions for the problems with the mixed-type boundary conditions using BEMs". In: *Finite elements in analysis and design* 40.11 (2004), pp. 1521–1549.

[33]   X.N. Chen and S. D. Sharma. "A slender ship moving at a near-critical speed in a shallow channel". In: *Journal of Fluid Mechanics* 291 (1995), pp. 263–285.

[34]   Y. R. Choi, S. Y. Hong, and H. S. Choi. "An analysis of second-order wave forces on floating bodies by using a higher-order boundary element method". In: *Ocean Engineering* 28.1 (2001), pp. 117–138.

[35]   A. Clément et al. "The SEAREV wave energy converter". In: *Proceedings of the 6th Wave and Tidal Energy Conference, Glasgow, UK*. 2005.

[36]   A. Clément et al. "Wave energy in Europe: current status and perspectives". In: *Renewable and sustainable energy reviews* 6.5 (2002), pp. 405–431.

[37]   B. Cockburn and C.-W. Shu. "The local discontinuous Galerkin method for time-dependent convection-diffusion systems". In: *SIAM Journal on Numerical Analysis* 35.6 (1998), pp. 2440–2463.

[38]   A. Comerford et al. "A combined numerical and experimental framework for determining permeability properties of the arterial media". In: *Biomechanics and modeling in mechanobiology* 14.2 (2015), pp. 297–313.

[39]   R. Courant, K. Friedrichs, and H. Lewy. "On the partial difference equations of mathematical physics". In: *IBM journal of Research and Development* 11.2 (1967), pp. 215–234.

[40]   S. H. Crandall. *Engineering analysis: A survey of numerical procedures*. Krieger Publishing Co., Inc., 1983.

[41]   W.E. Cummins. *The impulse response function and ship motions*. Tech. rep. David Taylor Model Basin Washington DC, 1962.

[42]   G. G. Dahlquist. "A special stability problem for linear multistep methods". In: *BIT Numerical Mathematics* 3.1 (1963), pp. 27–43.

[43]   S.N. Das and S.K. Das. "Mathematical model for coupled roll and yaw motions of a floating body in regular waves under resonant and non-resonant conditions". In: *Applied Mathematical Modelling* 29.1 (2005), pp. 19–34.

[44]   E. B. Davies and M. Plum. "Spectral pollution". In: *IMA Journal of Numerical Analysis* 24.3 (2004), pp. 417–438.

[45]   R. G. Dean and R. A. Dalrymple. *Water wave mechanics for engineers and scientists*. Vol. 2. World Scientific Publishing Company, 1991.

[46]   X. Deng et al. "Geometric conservation law and applications to high-order finite difference schemes with stationary grids". In: *Journal of Computational Physics* 230.4 (2011), pp. 1100–1115.

[47]   B. Devolder. "Hydrodynamic Modelling of Wave Energy Converter Arrays". PhD thesis. Ghent University, 2017.

[48]   F. Dias and T. J. Bridges. "The numerical computation of freely propagating time-dependent irrotational water waves". In: *Fluid Dynamics Research* 38.12 (2006), pp. 803–830.

[49]   M.W. Dingemans. *Water wave propagation over uneven bottoms*. Advanced Series on Ocean Engineering. 1997.

[50]   B. Drew, A. R. Plummer, and M. N. Sahinkaya. *A review of wave energy converter technology*. 2009.

[51]   M. Dubiner. "Spectral methods on triangles and other domains". In: *Journal of Scientific Computing* 6.4 (1991), pp. 345–390.

[52] M. Dumbser et al. "ADER schemes on unstructured meshes for nonconservative hyperbolic systems: Applications to geophysical flows". In: *Computers & Fluids* 38.9 (2009), pp. 1731–1748.

[53] L. Elden, L. Wittmeyer-Koch, and H. B. Nielsen. "Introduction to Numerical Computation-analysis and MATLAB illustrations". In: (2004).

[54] H. C. Elman, D. J. Silvester, and A. J. Wathen. *Finite elements and fast iterative solvers: with applications in incompressible fluid dynamics*. Numerical Mathematics and Science, 2014.

[55] A. P. Engsig-Karup, C. Eskilsson, and D. Bigoni. "A stabilised nodal spectral element method for fully nonlinear water waves". In: *Journal of Computational Physics* 318 (2016), pp. 1–21.

[56] A. P. Engsig-Karup et al. "Nodal DG-FEM solution of high-order Boussinesq-type equations". In: *Journal of engineering mathematics* 56.3 (2006), pp. 351–370.

[57] A.P. Engsig-Karup, C. Eskilsson, et al. "Spectral element FNPF simulation of focused wave groups impacting a fixed FPSO". In: *The 28th International Ocean and Polar Engineering Conference*. International Society of Offshore and Polar Engineers. 2018.

[58] A.P. Engsig-Karup, C. Monteserin, and C. Eskilsson. "A stabilised mixed Eulerian Lagrangian spectral element method for nonlinear wave interaction with fixed structures". In: *Submitted for peer-review. See also URL http://https://arxiv.org/abs/1703.09697* ().

[59] R.C. Ertekin, W.C. Webster, and J.V. Wehausen. "Waves caused by a moving disturbance in a shallow channel of finite width". In: *Journal of Fluid Mechanics* 169 (1986), pp. 275–292.

[60] C. Eskilsson and S. J. Sherwin. "Spectral/hp discontinuous Galerkin methods for modelling 2D Boussinesq equations". In: *Journal of Computational Physics* 212.2 (2006), pp. 566–589.

[61] C. Eskilsson and S.J. Sherwin. "A discontinuous spectral element model for Boussinesq-type equations". In: *Journal of Scientific Computing* 17.1-4 (2002), pp. 143–152.

[62] C. Eskilsson, S.J. Sherwin, and L. Bergdahl. "An unstructured spectral/hp element model for enhanced Boussinesq-type equations". In: *Coastal Engineering* 53.11 (2006), pp. 947–963.

[63] C. Eskilsson et al. "CFD study of the overtopping discharge of the Wave Dragon wave energy converter". In: *Renewable Energies Offshore* (2015), pp. 287–294.

[64] C. Eskilsson et al. "Wave induced motions of point-absorbers: a hierarchical investigation of hydrodynamic models". In: *11th European Wave and Tidal Energy Conference (EWTEC). Nantes, France*. 2015.

[65] D.V. Evans. "The oscillating water column wave-energy device". In: *IMA Journal of Applied Mathematics* 22.4 (1978), pp. 423–433.

[66] A. F.O. Falcão and J. C.C. Henriques. "Oscillating-water-column wave energy converters and air turbines: A review". In: *Renewable Energy* 85 (2016), pp. 1391–1424.

[67] J. Falnes and P. M. Lillebekken. "Budal's latching-controlled-buoy type wave-power plant". In: (2003).

[68] O. Faltinsen. *Sea loads on ships and offshore structures*. Vol. 1. Cambridge university press, 1993.

[69] C. B Field. *Climate change 2014–Impacts, adaptation and vulnerability: Regional aspects*. Cambridge University Press, 2014.

[70] J. Fiévez and T. Sawyer. "Lessons learned from building and operating a grid connected wave energy plant". In: *Proceedings of the 11th European Wave and Tidal Energy Conference, Nantes, France*. 2015, pp. 6–11.

[71] A. G. Filippini et al. "On the nonlinear behaviour of Boussinesq type models: Amplitude-velocity vs amplitude-flux forms". In: *Coastal Engineering* 99 (2015), pp. 109–123.

[72] B.A. Finlayson and L.E. Scriven. "The method of weighted residuals—a review". In: *Appl. Mech. Rev* 19.9 (1966), pp. 735–748.

[73] U. S. Fjordholm, S. Mishra, and E. Tadmor. "Well-balanced and energy stable schemes for the shallow water equations with discontinuous topography". In: *Journal of Computational Physics* 230.14 (2011), pp. 5587–5609.

[74] B. G. Galerkin. "Series solution of some problems of elastic equilibrium of rods and plates". In: *Vestn. Inzh. Tekh* 19 (1915), pp. 897–908.

[75] J. Gilloteaux. "Mouvements de grande amplitude d'un corps flottant en fluide parfait. Application à la récupération de l'énergie des vagues." PhD thesis. Ecole Centrale de Nantes (ECN); Université de Nantes, 2007.

[76] G. Giorgi and J. V. Ringwood. "Implementation of latching control in a numerical wave tank with regular waves". In: *Journal of Ocean Engineering and Marine Energy* 2.2 (2016), pp. 211–226.

[77] G.S. Gipson. "Boundary element fundamentals- Basic concepts and recent developments in the Poisson equation". In: *Southampton, England and Billerica, MA, Computational Mechanics Publications(Topics in Engineering.* 2 (1987).

[78] E. Godlewski et al. "Congested shallow water model: roof modelling in free surface flow". In: *ESAIM: Mathematical Modelling and Numerical Analysis* (2018).

[79] W.J. Gordon and C.A. Hall. "Construction of curvilinear co-ordinate systems and applications to mesh generation". In: *International Journal for Numerical Methods in Engineering* 7.4 (1973), pp. 461–477.

[80] M. Gouin, G. Ducrozet, and P. Ferrant. "Development and validation of a non-linear spectral model for water waves over variable depth". In: *European Journal of Mechanics-B/Fluids* 57 (2016), pp. 115–128.

[81] A. E. Green and P. M. Naghdi. "A derivation of equations for wave propagation in water of variable depth". In: *Journal of Fluid Mechanics* 78.2 (1976), pp. 237–246.

[82] M. Greenhow and S.P. White. "Optimal heave motion of some axisymmetric wave energy devices in sinusoidal waves". In: *Applied Ocean Research* 19.3-4 (1997), pp. 141–159.

[83] K. Grimich et al. "An accurate finite-volume formulation of a Residual-Based Compact scheme for unsteady compressible flows". In: *Computers & Fluids* 92 (2014), pp. 93–112.

[84] J. Grooss and J. S. Hesthaven. "A level set discontinuous Galerkin method for free surface flows". In: *Computer Methods in Applied Mechanics and Engineering* 195.25-28 (2006), pp. 3406–3429.

[85]   C. Grossmann, H. Roos, and M. Stynes. *Numerical treatment of partial differential equations*. Vol. 154. Springer, 2007.

[86]   E. Guerber et al. "A fully nonlinear implicit model for wave interactions with submerged structures in forced or free motion". In: *Engineering Analysis with Boundary Elements* 36.7 (2012), pp. 1151–1163.

[87]   K. Gunn and C. Stock-Williams. "Quantifying the global wave power resource". In: *Renewable Energy* 44 (2012), pp. 296–304.

[88]   B. Gustafsson. *High order difference methods for time dependent PDE*. Vol. 38. Springer Science & Business Media, 2007.

[89]   J. Hals, T. Bjarte-Larsson, and J. Falnes. "Optimum reactive control and control by latching of a wave-absorbing semisubmerged heaving sphere". In: *ASME 2002 21st International Conference on Offshore Mechanics and Arctic Engineering*. American Society of Mechanical Engineers. 2002, pp. 415–423.

[90]   D.M. Hawken, P. Townsend, and M.F. Webster. "A comparison of gradient recovery methods in finite-element calculations". In: *Communications in Applied Numerical Methods* 7.3 (1991), pp. 195–204.

[91]   R. Henderson. "Design, simulation, and testing of a novel hydraulic power take-off system for the Pelamis wave energy converter". In: *Renewable energy* 31.2 (2006), pp. 271–283.

[92]   J. S. Hesthaven and T. Warburton. *Nodal discontinuous Galerkin methods: algorithms, analysis, and applications*. Springer Science & Business Media, 2007.

[93]   R. A. Horn and C. R. Johnson. "Norms for vectors and matrices". In: *Matrix analysis* (1990), pp. 313–386.

[94]   W. Hundsdorfer, S. J. Ruuth, and R. J. Spiteri. "Monotonicity-preserving linear multistep methods". In: *SIAM Journal on Numerical Analysis* 41.2 (2003), pp. 605–623.

[95]   W. Hundsdorfer and J. G. Verwer. *Numerical solution of time-dependent advection-diffusion-reaction equations*. Vol. 33. Springer Science & Business Media, 2013.

[96]   T. Jiang. "Ship waves in shallow water". In: *FORTSCHRITT BERICHTE-VDI REIHE 12 VERKEHRSTECHNIK FAHRZEUGTECHNIK* (2001).

[97]   F. John. "On the motion of floating bodies. I". In: *Communications on Pure and Applied Mathematics* 2.1 (1949), pp. 13–57.

[98]   J. R. Joubert et al. "Wave Energy Converters (WECs)". In: (Oct. 2013).

[99]   G. Karniadakis and S. Sherwin. *Spectral/hp element methods for computational fluid dynamics*. Oxford University Press, 2013.

[100]   G. E. Karniadakis and S. J. Sherwin. *Spectral/hp element methods for CFD (Numerical mathematics and scientific computation)*. Oxford University Press, New York, 1999.

[101]   M. Kazolea and M. Ricchiuto. "On wave breaking for Boussinesq-type models". In: *Ocean Modelling* 123 (2018), pp. 16–39.

[102]   C.H. Kim, A.H. Clément, K. Tanizawa, et al. "Recent research and development of numerical wave tanks-a review". In: *International Journal of Offshore and Polar Engineering* 9.04 (1999).

[103] J. King et al. "Exploiting batch processing on streaming architectures to solve 2D elliptic finite element problems: a Hybridized Discontinuous Galerkin (HDG) case study". In: *Journal of Scientific Computing* 60.2 (2014), pp. 457–482.

[104] J. Klosa. "Extrapolated BDF residual distribution schemes for the shallow water equations". PhD thesis. Master thesis, 2012.

[105] J. P. Kofoed et al. "Prototype testing of the wave energy converter wave dragon". In: *Renewable energy* 31.2 (2006), pp. 181–189.

[106] W. Koo, KR. Lee, et al. "Numerical and experimental analysis of Backward Bent Duct Buoy (BBDB) wave energy converter". In: *The Twenty-first International Offshore and Polar Engineering Conference*. International Society of Offshore and Polar Engineers. 2011.

[107] E. V. Koutandos, Th. V. Karambas, and C. G. Koutitas. "Floating Breakwater Response to Waves Action Using a Boussinesq Model Coupled with a 2DV Elliptic Solver". In: *Journal of Waterway, Port, Coastal, and Ocean Engineering* 130.5 (Sept. 2004), pp. 243–255. DOI: `10.1061/(ASCE)0733-950X(2004)130:5(243)`.

[108] H. Kreiss, H.-O. Kreiss, and J. Oliger. *Methods for the approximate solution of time dependent problems*. 10. International Council of Scientific Unions, World Meteorological Organization, 1973.

[109] C. Lacor, S. Smirnov, and M. Baelmans. "A finite volume formulation of compact central schemes on arbitrary structured grids". In: *Journal of Computational Physics* 198.2 (2004), pp. 535–566.

[110] D. Lannes. Private Communication. 2018.

[111] D. Lannes. "On the dynamics of floating structures". In: *Annals of PDE* 3.1 (2017), p. 11.

[112] D. Lannes. *The water waves problem: mathematical analysis and asymptotics*. Vol. 188. American Mathematical Soc., 2013.

[113] J. Larsen and H. Dancy. "Open boundaries in short wave simulations—a new approach". In: *Coastal Engineering* 7.3 (1983), pp. 285–297.

[114] W. Laskowski, H. B. Bingham, and A. P. Engsig-Karup. "Modelling of Wave-structure Interaction for Cylindrical Structures using a Spectral Element Multigrid Method". In: ().

[115] S. K. Lele. "Compact finite difference schemes with spectral-like resolution". In: *Journal of computational physics* 103.1 (1992), pp. 16–42.

[116] L. Letournel et al. "Comparison of fully nonlinear and weakly nonlinear potential flow solvers for the study of wave energy converters undergoing large amplitude motions". In: *ASME 2014 33rd International Conference on Ocean, Offshore and Arctic Engineering*. American Society of Mechanical Engineers. 2014, V09BT09A002–V09BT09A002.

[117] R. J. LeVeque. "Finite difference methods for differential equations". In: *Draft version for use in AMath* 585.6 (1998), p. 112.

[118] R. J. LeVeque. *Finite volume methods for hyperbolic problems*. Vol. 31. Cambridge university press, 2002.

[119] Y. Li and Y.-H. Yu. "A synthesis of numerical methods for modeling wave energy converter-point absorbers". In: *Renewable and Sustainable Energy Reviews* 16.6 (2012), pp. 4352–4364.

[120] P. Lin. "A multiple-layer σ-coordinate model for simulation of wave–structure interaction". In: *Computers & fluids* 35.2 (2006), pp. 147–167.

[121] P. Lin and P. L.-F. Liu. "Internal wave-maker for Navier-Stokes equations models". In: *Journal of waterway, port, coastal, and ocean engineering* 125.4 (1999), pp. 207–215.

[122] W.M. Lin. "Nonlinear forced motions of floating bodies". In: *Proccedings of 15th Symposium on Naval Hydrodynamics, 1984*. 1984.

[123] OpenCFD Ltd. *OpenFOAM*. 2014. URL: http://openfoam.org.

[124] P. A. Madsen and O. R. Sørensen. "A new form of the Boussinesq equations with improved linear dispersion characteristics. Part 2. A slowly-varying bathymetry". In: *Coastal engineering* 18.3-4 (1992), pp. 183–204.

[125] D. Magagna and A. Uihlein. "Ocean energy development in Europe: Current status and future perspectives". In: *International Journal of Marine Energy* 11 (2015), pp. 84–104.

[126] J. S. Mani. "Design of Y Frame Floating Breakwater". en. In: *Journal of Waterway, Port, Coastal, and Ocean Engineering* 117.2 (Mar. 1991), pp. 105–119. ISSN: 0733-950X. DOI: 10.1061/(ASCE)0733-950X(1991)117:2(105).

[127] L. Martinelli and P. Ruol. "2D Model of floating breakwater dynamics under linear and nonlinear waves". In: *COMSOL users conference* (2006).

[128] L. Martinelli and P. Ruol. "2D Model of floating breakwater dynamics under linear and nonlinear waves". In: *COMSOL users conference*. Vol. 353. 2006.

[129] K. Mattsson, M. Svärd, and J. Nordström. "Stable and accurate artificial dissipation". In: *Journal of Scientific Computing* 21.1 (2004), pp. 57–79.

[130] C. C. Mei, M. Stiassnie, and D. K.-P. Yue. *Theory and applications of ocean surface waves: nonlinear aspects*. Vol. 23. World scientific, 2005.

[131] E. Mendoza et al. "Beach response to wave energy converter farms acting as coastal defence". In: *Coastal Engineering* 87 (2014), pp. 97–111.

[132] *MIDWEST – Multi-fIdelity Decision making tools for Wave Energy SysTems*. December, 2015. URL: https://project.inria.fr/midwest/.

[133] Climate Change Mitigation. "IPCC special report on renewable energy sources and climate change mitigation". In: (2011).

[134] C. Monteserin, A. P. Engsig-Karup, and C. Eskilsson. "Nonlinear Wave-Body Interaction Using a Mixed-Eulerian-Lagrangian Spectral Element Model". In: *ASME 2018 37th International Conference on Ocean, Offshore and Arctic Engineering*. American Society of Mechanical Engineers. 2018, V009T13A030–V009T13A030.

[135] D. Moxey et al. "A thermo-elastic analogy for high-order curvilinear meshing with control of mesh validity and quality". In: *Procedia engineering* 82 (2014), pp. 127–135.

[136] M. L. Muñoz-Ruiz and C. Parés. "On the convergence and well-balanced property of path-conservative numerical schemes for systems of balance laws". In: *Journal of Scientific Computing* 48.1-3 (2011), pp. 274–295.

[137] S. Nimmala, S. Yim, and S. Grilli. "An Efficient 3-D FNPF Numerical Wave Tank for Virtual Large-Scale Wave Basin Experiment". In: *ASME 2012 31st International Conference on Ocean, Offshore and Arctic Engineering*. American Society of Mechanical Engineers. 2012, pp. 703–711.

[138] J. H. Nørgaard, T. L. Andersen, et al. "Investigation of wave transmission from a floating wave dragon wave energy converter". In: *The Twenty-second International Offshore and Polar Engineering Conference*. International Society of Offshore and Polar Engineers. 2012.

[139] O. Nwogu. "Alternative form of Boussinesq equations for nearshore wave propagation". In: *Journal of Waterway, Port, Coastal, and Ocean Engineering* 119.6 (1993), pp. 618–638.

[140] O. Nwogu. "Nonlinear evolution of directional wave spectra in shallow water". In: *Coastal Engineering 1994*. 1994.

[141] CorPower Ocean. "The CorPower Wave Energy Converter". In: (2012).

[142] J. Palm. "Mooring dynamics for wave energy applications". PhD thesis. Chalmers University of Technology, Gothenburg, Sweden, 2017.

[143] J. Palm et al. "CFD simulation of a moored floating wave energy converter". In: *Proceedings of the 10th European Wave and Tidal Energy Conference, Aalborg, Denmark*. Vol. 25. 2013.

[144] R. Pasquetti. "Viscous Stabilizations for High Order Approximations of Saint-Venant and Boussinesq Flows". In: *Spectral and High Order Methods for Partial Differential Equations ICOSAHOM 2016*. Ed. by Marco L. Bittencourt, Ney A. Dumont, and Jan S. Hesthaven. Cham: Springer International Publishing, 2017, pp. 519–531.

[145] A. T. Patera. "A spectral element method for fluid dynamics: laminar flow in a channel expansion". In: *Journal of computational Physics* 54.3 (1984), pp. 468–488.

[146] M. Penalba, G. Giorgi, and J. V. Ringwood. "Mathematical modelling of wave energy converters: a review of nonlinear approaches". In: *Renewable and Sustainable Energy Reviews* 78 (2017), pp. 1188–1207.

[147] D.H. Peregrine. "Long waves on a beach". In: *Journal of fluid mechanics* 27.4 (1967), pp. 815–827.

[148] C. Pozrikidis. *Introduction to finite and spectral element methods using MATLAB*. CRC Press, 2005.

[149] J. Proriol. "Sur une famille de polynomes á deux variables orthogonaux dans un triangle". In: *COMPTES RENDUS HEBDOMADAIRES DES SEANCES DE L ACADEMIE DES SCIENCES* 245.26 (1957), pp. 2459–2461.

[150] A. Quarteroni and A. Valli. *Numerical approximation of partial differential equations*. Vol. 23. Springer Science & Business Media, 2008.

[151] H. Ranocha. "Generalised summation-by-parts operators and variable coefficients". In: *Journal of Computational Physics* 362 (2018), pp. 20–48.

[152] A. Rezgui, P. Cinnella, and A. Lerat. "Third-order accurate finite volume schemes for Euler computations on curvilinear meshes". In: *Computers & fluids* 30.7-8 (2001), pp. 875–901.

[153] M. Ricchiuto and A. G. Filippini. "Upwind residual discretization of enhanced Boussinesq equations for wave propagation over complex bathymetries". In: *Journal of Computational Physics* 271 (2014), pp. 306–341.

[154] D. P. Rijnsdorp and M. Zijlema. "Simulating waves and their interactions with a restrained ship using a non-hydrostatic wave-flow model". In: *Coastal Engineering* 114 (2016), pp. 119–136.

[155] P. J. Roache. "Code verification by the method of manufactured solutions". In: *Journal of Fluids Engineering* 124.1 (2002), pp. 4–10.

[156] C. J. Roy et al. "Verification of Euler/Navier–Stokes codes using the method of manufactured solutions". In: *International Journal for Numerical Methods in Fluids* 44.6 (2004), pp. 599–620.

[157] K. Salari and P. Knupp. *Code verification by the method of manufactured solutions.* Tech. rep. Sandia National Labs., Albuquerque, NM (US); Sandia National Labs, 2000.

[158] S. H. Salter. "Wave power". In: *Nature* 249.5459 (1974), pp. 720–724.

[159] A. Samii and C. Dawson. "An explicit hybridized discontinuous Galerkin method for Serre–Green–Naghdi wave model". In: *Computer Methods in Applied Mechanics and Engineering* 330 (2018), pp. 447–470.

[160] A. Sandberg et al. "Critical factors influencing viability of wave energy converters in off-grid luxury resorts and small utilities". In: *Sustainability* 8.12 (2016), p. 1274.

[161] D. Serson, J.R. Meneghini, and S.J. Sherwin. "Velocity-correction schemes for the incompressible Navier–Stokes equations in general coordinate systems". In: *Journal of Computational Physics* 316 (2016), pp. 243–254.

[162] C.-W. Shu. "Essentially non-oscillatory and weighted essentially non-oscillatory schemes for hyperbolic conservation laws". In: *Advanced numerical approximation of nonlinear hyperbolic equations.* Springer, 1998, pp. 325–432.

[163] C.W. Shu. "High order WENO and DG methods for time-dependent convection-dominated PDEs: A brief survey of several recent developments". In: *Journal of Computational Physics* 316 (2016), pp. 598–613.

[164] L. Shunn and F. Ham. "Method of manufactured solutions applied to variable-density flow solvers". In: *Annual Research Briefs-2007, Center for Turbulence Research* (2007), pp. 155–168.

[165] J. Spinneken et al. "Assessment of an advanced finite element tool for the simulation of fully-nonlinear gravity water waves". In: *The Twenty-second International Offshore and Polar Engineering Conference.* International Society of Offshore and Polar Engineers. 2012.

[166] M. A. Sprague and T. L. Geers. "A spectral-element/finite-element analysis of a ship-like structure subjected to an underwater explosion". In: *Computer methods in applied mechanics and engineering* 195.17-18 (2006), pp. 2149–2167.

[167] V. Sriram, S.A. Sannasiraj, and V. Sundar. "Velocity calculation methods in finite element based MEL formulation". In: *Advances in Numerical Simulation of Nonlinear Water Waves.* World Scientific, 2010, pp. 203–244.

[168] T. F. Stocker et al. *IPCC, 2013: climate change 2013: the physical science basis. Contribution of working group I to the fifth assessment report of the intergovernmental panel on climate change.* 2013.

[169] G. Strang and G. J. Fix. *An analysis of the finite element method.* Vol. 212. Prentice-hall Englewood Cliffs, NJ, 1973.

[170] H. Sun. "A boundary element method applied to strongly nonlinear wave-body interaction problems". In: *Fakultet for ingeniørvitenskap og teknologi* (2007).

[171] N. Taniguchi and T. Kobayashi. "Finite volume method on the unstructured grid system". In: *Computers & Fluids* 19.3-4 (1991), pp. 287–295.

[172] K. Tanizawa. "The state of the art on numerical wave tank". In: *Proceedings of 4th Osaka Colloquium on Seakeeping Performance of Ships 2000*. 2000, pp. 95–114.

[173] B. Teillant, J.-C. Gilloteaux, and J.V. Ringwood. "Optimal damping profile for a heaving buoy wave energy converter". In: *IFAC Proceedings Volumes* 43.20 (2010), pp. 360–365.

[174] B. Teng and R. E. Taylor. "New higher-order boundary element methods for wave diffraction/radiation". In: *Applied Ocean Research* 17.2 (1995), pp. 71–77.

[175] Inc. The MathWorks. *MATLAB and Statistics Toolbox Release 2016b*. 2016.

[176] E. F. Toro. *Riemann solvers and numerical methods for fluid dynamics: a practical introduction*. Springer Science & Business Media, 2013.

[177] E.F. Toro. "Riemann Solvers and Numerical Methods for Fluid Dynamics–Springer". In: *Heidelberg, 624pp* (1999).

[178] Innovation Union. *EC. Communication from the Commission to the European Parliament, the Council, the European Economic and Social Committee and the Committee of the Regions – A roadmap for moving to a competitive low carbon economy in 2050. European Commission, Brussels, European Union; 2011. ommunication from the Commission to the European Parliament, the Council, the European Economic and Social Committee and the Committee of the Regions*. 2011.

[179] *WAMIT*. URL: https://www.wamit.com/.

[180] Z. J. Wang et al. "High-order CFD methods: current status and perspective". In: *International Journal for Numerical Methods in Fluids* 72.8 (2013), pp. 811–845.

[181] *Wave Swell Energy*. URL: https://waveswellenergy.com.au/.

[182] J. Weber. "WEC Technology Readiness and Performance Matrix–finding the best research technology development trajectory". In: *Int. Conf. Ocean Energy Dublin Irel*. 2012.

[183] *WEC-Sim*. URL: http://en.openei.org/wiki/WEC-Sim.

[184] J. F. Wendt. *Computational fluid dynamics: an introduction*. Springer Science & Business Media, 2008.

[185] L. Weynans and D. Lannes. *Generating boundary conditions for a Boussinesq system*. Research Report RR 9248. INRIA Bordeaux, 2019. URL: https://hal.inria.fr/hal-01982925.

[186] A.N. Williams, H.S. Lee, and Z. Huang. "Floating pontoon breakwaters". In: *Ocean Engineering* 27.3 (2000), pp. 221–240.

[187] K.J. Williams. "The boundary integral equation method for the solution of wave-obstacle interaction". In: *International journal for numerical methods in fluids* 8.2 (1988), pp. 227–242.

[188] H. A. Wolgamot and C. J. Fitzgerald. "Nonlinear hydrodynamic and real fluid effects on wave energy converters". In: *Proceedings of the Institution of Mechanical Engineers, Part A: Journal of Power and Energy* 229.7 (2015), pp. 772–794.

[189] G.X. Wu and R. E. Taylor. "The coupled finite element and boundary element analysis of nonlinear interactions between waves and bodies". In: *Ocean Engineering* 30.3 (2003), pp. 387–400.

[190] D. Xu et al. "Effect of nonuniform grids on high-order finite difference method". In: *Advances in Applied Mathematics and Mechanics* 9.4 (2017), pp. 1012–1034.

[191] H. Xu et al. "Spectral/hp element methods: Recent developments, applications, and perspectives". In: *Journal of Hydrodynamics* 30.1 (2018), pp. 1–22.

[192] J. Yan and C.-W. Shu. "Local discontinuous Galerkin methods for partial differential equations with higher order derivatives". In: *Journal of Scientific Computing* 17.1-4 (2002), pp. 27–47.

[193] Y.H. Yu and Y. Li. "Reynolds-Averaged Navier–Stokes simulation of the heave performance of a two-body floating-point absorber wave energy system". In: *Computers & Fluids* 73 (2013), pp. 104–114.

[194] S. Zhao. "On the spurious solutions in the high-order finite difference methods for eigenvalue problems". In: *Computer methods in applied mechanics and engineering* 196.49-52 (2007), pp. 5031–5046.

[195] S.-P. Zhu, H.-W. Liu, and K. Chen. "A general DRBEM model for wave refraction and diffraction". In: *Engineering analysis with boundary elements* 24.5 (2000), pp. 377–390.